Accurate GNSS Positioning in Urban Canyons with Extended Kalman Filter

髙山，洋史

(Degree)
博士（工学）

(Date of Degree)
2023-03-25

(Date of Publication)
2025-03-25

(Resource Type)
doctoral thesis

(Report Number)
甲第8654号

(URL)
https://hdl.handle.net/20.500.14094/0100482402

Doctoral Dissertation

Accurate GNSS Positioning in Urban Canyons with Extended Kalman Filter

拡張カルマンフィルタによる都市部でのGNSS高精度測位

January, 2023

Graduate School of System Informatics

Kobe University

TAKAYAMA Yoji

髙山 洋史

To my wife and sons

Abstract

Inaccuracy in urban canyons has been a persistent and lingering problem for the Global Navigation Satellite System (GNSS). This thesis reports the results of a study on performance improvement of the extended Kalman filter (EKF) to obtain more accurate positions in urban canyons.

GNSS is a system that provides positioning on a global basis. GNSS receivers on the ground measure distance to satellites based on the time of flight of satellite signals. And then they determine their positions based on trilateration. GNSS positioning accuracy depends on signals' propagation delay due to, e.g., the troposphere and ionosphere. GNSS can achieve accuracy within ten meters with no objects in the lines of sight of satellites. The areas with no objects in the lines of sight of satellites are referred to as open sky areas.

One last great unsolved GNSS problem is inaccuracy in urban canyons. Positioning with GNSS in urban canyons suffers from significant position errors due to Non-Line-Of-Sight (NLOS) reception. NLOS reception occurs where the direct signal is blocked, and the signal is received only via reflection or diffraction. Measurement errors due to NLOS reception are characterized by their sign and size. Since signals via reflection or diffraction arrive later than (blocked) signals via direct paths, measurement errors due to NLOS reception are always positive. Furthermore, their errors depend on their path delays and are potentially unbounded. They can be over a hundred meters and outliers that can degrade position accuracy significantly.

Because of the low computational cost, almost all GNSS receivers employ the extended Kalman filter to determine their positions. The EKF performance is highly dependent on the accuracy of measurement and the setting of parameters in the EKF. Inaccurate and biased measurements due to NLOS reception can reduce the estimation accuracy of the EKF. This research aims to achieve a few meters of accuracy in urban canyons by removing outliers and choosing parameters in the EKF according to remained measurements. The enhanced EKF performance will benefit our society.

This research solves the problem of inaccuracy in urban canyons in two stages. The first stage is to develop a method to reject outliers due to NLOS reception from the computation of the EKF. This stage begins with introducing the model that represents the surrounding environments, e.g., buildings, of a GNSS receiver to compute path delays geometrically due to reflection or diffraction. Since measurement errors in NLOS signals depend heavily on path delays due to reflection or diffraction, computed path delays using the geometric model can predict measurement errors. Based on the predicted values, the method can improve position accuracy by detecting and rejecting outliers due to NLOS reception.

However, removing outliers decreases the number of measurements and may cause poor satellite geometry. Poor satellite geometry means a biased distribution of satellites as seen by a GNSS receiver. As positioning accuracy highly depends on satellite geometry, it is necessary to show how poor satellite geometry affects the EKF performance.

Therefore, the second stage begins with numerical examples to point out the problem caused by poor satellite geometry. These examples illustrate that a fictitious noise approach, which can avoid filter divergence by adding fictitious noise to process noise heuristically, results in excessive inflation of the estimation error covariance matrix in the EKF with poor satellite geometry. Further, this stage provides a theoretical analysis of the sensitivity of the estimation error covariance matrix varying on process noise in the EKF. From the examples and the theoretical analysis, a process noise model that chooses fictitious noise based on satellite geometry is proposed in this stage. The proposed process noise model can suppress inflation of the estimation error covariance matrix when satellite geometry is poor. To our best knowledge, the proposed model in the second stage is the first to choose process noise depending on satellite geometry.

The key findings of this research are twofold and come from each of the stages described above. The first is the performance improvement in urban canyons by removing outliers and demonstrated through driving tests in Shinjuku, Tokyo, known for NLOS reception. The second is also performance improvement in urban canyons by avoiding unintentional inflation of the estimation error covariance matrix. It is revealed through theoretical and experimental results. In addition, the process noise model proposed in the second stage can be applied to applications with a generic EKF other than GNSS. Numerical simulations in robot localization show that the proposed model improves localization performance.

Chapter 1 introduces the background and the main issue of this research. The background begins with the current GNSS status from the point of view of accuracy to define the main issue of this research, which is inaccuracy in urban canyons. And then, this chapter refers to some studies related to this research's main issue to show the difference between the studies and this research. The difference would show our contribution that represents an advance in current knowledge in the GNSS field. Further, this chapter summarizes the main results of this thesis through overviews of each chapter. Finally, three background materials and a mathematical introduction to the EKF are given in this chapter that would be needed in later chapters. Three materials are the single point positioning with the EKF, measurement errors in urban canyons, and the role of satellite geometry in positioning.

Chapter 2 is devoted to developing a method to detect and reject outliers due to NLOS re-

ception. This chapter begins with a review of the adaptive extended Kalman filter proposed in previous studies to deal with measurement outliers in urban canyons. The adaptive EKF can determine the appropriate noise input level in real time with innovations or residuals of measurements. Although the adaptive EKF reduces the impacts of NLOS reception on estimates, measurement errors due to NLOS reception may make biased position errors because they are always positive. Thus, the adaptive EKF should not use measurements due to NLOS reception, even with the adjustment of noise input level.

This chapter proposes a method to reject outliers from the adaptive EKF to reduce biased position errors, introducing a model that represents the surrounding environments in urban canyons to predict path delays of signals due to NLOS reception. Since measurement errors due to NLOS reception depend on path delays of reflected or diffracted signals to direct signals, measurement errors can be predicted geometrically using the model. The proposed method has a threshold to detect signals whose path delay is nearly equal to or longer than the predicted values of path delays. The threshold is chosen as a smaller predicted value so that it can detect NLOS signals as much as possible. Removing measurements whose path delays are too long can reduce biased position errors. Note that the prediction of path delays with the geometric model is sometimes inaccurate. And some NLOS signals might be accepted and used in the computation of the EKF. Since the adaptive EKF can determine the appropriate noise input level for accepted NLOS signals, it can reduce the impacts of the accepted NLOS signals on state estimates. The results of experiments in urban canyons show the performance improvement of the adaptive EKF with the proposed method.

Chapter 3 begins with numerical examples to highlight the problem caused by fictitious noise for avoiding filter divergence. The problem is that estimation errors by adding fictitious noise to process noise can be distributed more widely in a particular direction determined by satellite geometry. Since the estimation error covariance matrix in the EKF varies depending on fictitious noise, the sensitivity analysis of the matrix due to fictitious noise can explain the cause of the problem. From the sensitivity analysis, the variation of the estimation error covariance matrix depends on measurement matrices, that is, satellite geometry. This analysis and numerical examples indicate that fictitious noise may result in excessive inflation in a particular direction of the estimation error covariance matrix and eventually degrade filter performance.

Based on the results of numerical examples and the sensitivity analysis, this chapter presents a process noise model that varies depending on satellite geometry. The process noise model can suppress the inflation of the estimation error covariance matrix due to poor satellite geometry by

choosing a small or zero fictitious noise in a particular direction. The improvement of position accuracy due to the proposed model is demonstrated through experiments of stationary GNSS positioning with poor satellite geometry.

Chapter 4 presents a process noise model extended from the proposed model in Chapter 3. As stated earlier, the proposed model in Chapter 3 is derived based on the sensitivity analysis of the estimation error covariance matrix under some assumptions. Although one of the assumptions is that the state transition matrix is an identity matrix, the assumption does not often hold in the EKF for GNSS positioning. This explains that the proposed model in Chapter 3 should be extended.

This chapter begins with a sensitivity analysis of the estimation error covariance matrix without the assumptions introduced in Chapter 3. From this analysis, fictitious noise varies the estimation error covariance matrix. Keeping this in mind, let fictitious noise be chosen so that the variation of the estimation error covariance matrix will be a given value. For this purpose, the value is designed in two ways later described.

Since the size of the estimation error covariance matrix is usually large, it is difficult to determine appropriate values for all elements of the matrix. Therefore, the value should be constrained in some way to be able to determine. Recall that unintentional inflation of the estimation error covariance matrix may degrade filter performance, as Chapter 3 pointed out. This indicates that the directions exist such that inflation in the estimation error covariance matrix is unnecessary. Based on the consideration, the constraint by measurement matrices can be effective in forming the value.

In the first design, the value is chosen through a trial-and-error process. In the second design, the value is chosen to minimize the sum of the square of measurement residuals. In the sense of minimization, the value is referred to as a decision variable. Position accuracy improvement is demonstrated through stationary GNSS positioning for the first choice and in GNSS/INS positioning for the second choice.

Moreover, the extended process noise model can be applied to applications other than GNSS and GNSS/INS. For example, robot localization is one important system to determine the robot's position with range and vision sensors, such as LiDAR devices and cameras. It tends to suffer from unexpected dynamics errors in the prediction of robot motion. Furthermore, the information from these sensors often degenerates, for example, when the robot moves along the wall. This indicates that using the extended process noise model may improve the EKF performance by varying fictitious noise based on measurement matrices. Numerical simulations in

robot localization show the improved performance of the EKF for the localization system.

Chapter 5 concludes this thesis. This chapter begins with a brief revisit of the contents of each chapter and the key findings of this thesis. And then, it states the importance and significance of those findings compared with previous studies. Further, this chapter refers to possible applications to other areas with the proposed process noise model and the possibility of expanding the proposed process noise model to other nonlinear filters. Finally, future work on obtaining more accurate positions in urban canyons is presented.

Acknowledgement

The successful completion of this research results from the kindness and support I received from some people, and I would like to express my appreciation to them.

This research was conducted in Professor Hisashi Tamaki's laboratory, the Emergent Computing laboratory (CS14) of the Department of Information Science, Graduate School of System Informatics, Kobe University.

First, I would like to thank my main Adviser, Associate Professor Takateru Urakubo, for guiding me through my doctoral research. I also thank him for helping me to improve my thinking and writing and, most importantly, for the technical advice I received from his rich bank of knowledge. For these, I want to express my profound gratitude by saying a big thank you. I would like to express deep appreciation to Professor Hisashi Tamaki, my principal adviser, for all his done for me to ensure that this research ends successfully. Special thanks go to Professor Tetsuya Takiguchi and Professor Zhi-wei Luo, my co-advisers, for the highly valuable comments I received from them, which have improved the quality of this dissertation. I would like to extend my sincere thanks to Professor Sueo Sugimoto for providing valuable comments concerning Kalman filter.

I would like to thank all members in CS14 for providing me with a good environment for my research work. I say a big thank you to you all.

This endeavor would not have been possible without tremendous support from Furuno Electric Co. Ltd. I wish to express my cordial gratitude to Mr. Takahiko Ikeda, General Manager, Research & Development Department, System Product Division, Furuno Electric Co. Ltd., for allowing me to join the Ph.D. program of Kobe University. I would also like to thank my former and current section managers, Mr. Masataka Yasukawa and Mr. Noriyuki Kitamura, for their enormous help in proceeding with my doctoral research. Some of the ideas and motivations propelling my work were picked up from the doctoral research of Dr. Takaki Tominaga, and discussion with Mr. Akihiro Ohsugi and Mr. Takashi Kato. Dr. Hitoshi Kondo gave me valuable comments on my conference paper. This dissertation is based on work at Furuno. I would like to express deep gratitude to all colleagues in the GNSS team at Furuno.

Finally, I am extremely grateful to my family, Maki, Ritsuki, and Yuki, for their unconditional support and encouragement. I am also deeply grateful to my parents, Isamu and Shigemi, for their continuous support.

Contents

Chapter 1

Introduction

1.1 Unsolved GNSS Problem in Urban Canyons

Inaccurate positioning in urban canyons is one last unsolved problem with the Global Navigation Satellite System (GNSS) [1, 2]. Since billions of devices and almost infinite applications worldwide employ GNSS to determine their positions, inaccuracy in urban canyons significantly impacts our society. The problem might result in fatal errors in near-future mobilities, like autonomous vehicles or air mobility vehicles.

The position accuracy with GNSS is a few meters by single point positioning (SPP), a few decimeters by precise point positioning (PPP) [3], and a few centimeters by real-time kinematic (RTK) positioning [4]. This accuracy can be achieved only in open sky areas with few objects, such as buildings or walls, that can block, reflect, and diffract signals from satellites. Unfortunately, the position accuracy by SPP dramatically degrades above tens of meters due to Non-Line-Of-Sight (NLOS) signal reception in urban canyons. Although positioning is performed based on measurements extracted from satellite signals, measurements from NLOS signals tend to be outliers. To make matters worse, the PPP and RTK do not work in urban canyons either, because many obstacles can block direct signals from satellites and the temporary loss of the lock of a tracked signal often occurs.

One approach to solving the problem is improving the accuracy of SPP. Since the extended Kalman filter (EKF) [5, 6] usually accomplishes the SPP, the author has begun to enhance the EKF performance to achieve a few meters of accuracy in urban canyons as in open sky areas. The EKF performance depends heavily on measurement accuracy and setting parameters in the

EKF. The parameters are known as measurement and process covariance matrices. We need to address the issue in two stages to achieve the goal: (1) algorithm-based outlier rejection caused by NLOS signal receptions and (2) process noise setting that takes into account poor satellite geometry and its rapid change that may be caused by (1).

Although many researchers have developed methods to mitigate large position errors due to NLOS reception from hardware and software perspectives, none completely eliminates the effects due to NLOS reception on estimates. However, some different methods are not exclusive but complementary so that a portfolio approach can be effective [7]. Several ingenuities for GNSS antennas, such as multiple antennas, dual-polarization antennas, a well-designed GNSS antenna [8], and the CRPA system [9], allow receivers to receive direct signals by attenuating or rejecting NLOS signals. Some techniques, code discriminator design [9], early-late correlator comparison [10], and Doppler domain multipath mitigation [11] have been proposed from the view of the receiver's design. Using additional sensors or resources, such as fish-eye cameras and 3D-city maps [12, 13, 14], is also an attractive choice to mitigate position errors in urban canyons. Although these approaches are quite effective, it is difficult to apply them to any device due to costs and size.

More cost-effective approaches are algorithm-based outlier rejection. Receiver Autonomous Integrity Monitoring (RAIM) is a technique based on the consistency check of redundancy of measurements initially investigated in the aviation GNSS field [15, 16]. Within the framework of RAIM, Kalman filter-based RAIM techniques are proposed [17, 18]. Since almost all measurements would be obtained from NLOS signals in urban canyons, measurement outliers due to NLOS signals may pass through the consistency check unexpectedly. Innovation filtering is a generic method to reject outliers in the Kalman filter [9]. However, the literature [19] has reported that the method results in biased estimates. Furthermore, even if outliers due to NLOS signals are completely detected and rejected, such precise rejection leads to poor satellite geometry. Poor satellite geometry means biased distribution of satellites as seen by a receiver [20]. To the best of our knowledge, no results in the literature dealing with NLOS reception show how poor satellite geometry due to outlier rejection affects the EKF performance. For example, whether process noise, often chosen heuristically, works appropriately with poor satellite geometry must be examined.

The research aims to improve the EKF performance with an adaptive process noise setting

in the EKF while rejecting outliers due to NLOS reception, where *adaptive* means choosing process noise covariance in the EKF based on satellite geometry. Measurement outliers due to NLOS signals violate the assumption of measurement noise in the EKF. We can improve performance by rejecting measurement outliers from the filter computation. The rejection, however, would result in poor satellite geometry if a GNSS device installed on a vehicle moves in urban canyons. We highlight that poor satellite geometry causes performance degradation with a large process noise covariance. Thus, we can improve performance by choosing process noise covariance based on satellite geometry.

We first propose a novel method to reject measurement outliers based on the results of the state-of-the-art [13, 14]. The results show that measurement errors due to NLOS signals can be predicted by ray tracing with a 3D-city model. However, ray tracing with a 3D-city model requires a high computational cost. Therefore, we attempt to predict path delays due to NLOS signals with a simple geometric model instead of a 3D-city model. Comparing predicted path delays with a simple geometric model to innovations computed in the EKF, the method detects and rejects measurement outliers. We show the performance improvement with actual data collected in Shinjuku, Tokyo, famous for NLOS signal reception due to many skyscrapers.

We next design a process noise model based on satellite geometry. The EKF performance mainly depends on process noise covariance, one tuning parameter in the EKF. We often choose it to reduce unexpected estimation errors due to dynamics model uncertainties, that is, process noise covariance tends to be large to cover dynamics model uncertainties. Through sensitivity analysis and numerical examples, we point out that process noise covariance in a naïve manner may degrade the EKF performance with poor satellite geometry. To avoid degradation, we propose a process noise model that process noise covariance varies on satellite geometry. We show that the model improves the EKF performance through stationary single point positioning experiments.

We finally extend the process noise model based on satellite geometry in the following respects. The sensitivity analysis mentioned above is limited to the state transition matrix being an identity matrix. We remove this limitation and again show the sensitivity of the estimation error covariance matrix due to a process noise covariance. We design an extended process noise model based on the results of the generalized sensitivity analysis. A process noise covariance is determined by measurement matrices that represent satellite geometry. As far as we know, this is

the first model to choose process noise covariance based on measurement matrices. Moreover, we perform experiments to show enhanced position accuracy in driving tests in addition to stationary positioning.

1.2 Accurate Positioning Difficulties in Urban Canyons

1.2.1 Overview of Single Point Positioning with Extended Kalman Filter

This section introduces an overview of the single point positioning with the extended Kalman filter. Receiving a signal from a satellite, we obtain the distance between a GNSS receiver and a satellite from the time of flight of a signal. Since the time of flight is measured with the GNSS's clock and a GNSS receiver's clock, it includes the bias between these clocks. We call the distance contained in the clock bias *pseudo range*. Since the position vector of a GNSS receiver and the clock bias are unknown, we can compute the position and the clock bias by receiving simultaneously four or more signals, i.e., pseudo ranges, with a least-squares method. The single point positioning means that a single GNSS receiver computes its position and clock bias.

The extended Kalman filter (EKF) can be applied to the single point positioning with a low-computational cost to obtain more accurate positions than instantaneous least-squares methods. This thesis assumes that a GNSS receiver is installed on a four-wheel vehicle that moves on the ground. To construct the EKF requires a dynamics model of a state vector to represent how the state vector evolves. Therefore, we must define an appropriate vehicle motion model to represent the position of a driving car. Since the clock bias between the GNSS's system clock and a GNSS receiver's clock also varies, it is necessary to define a proper dynamics model for the clock bias.

Above mentioned dynamics model would have uncertainties. For example, we often use a vehicle motion model in that a velocity or acceleration is the first-order Markov process [21]. This model differs from the actual vehicle motion, and the difference may lead to unexpected position errors. To reduce unexpected position errors, we often select a process noise covariance in the EKF that can cover the difference. Since the difference is usually poorly known or unknown, we are apt to choose it heuristically.

Another example is the clock bias model. Almost all GNSS receivers adopt a Temperature Compensated Xtal Oscillator (TCXO) as a GNSS receiver clock. Since it varies depending on various effects, it is difficult to represent it as a model accurately. For the same reason as the vehicle motion model, we often choose the process noise covariance of the clock bias heuristically.

Dynamics model uncertainty is a topic not limited to the GNSS field but perhaps common to many applications with the EKF. Although many techniques, e.g., fading memory filter and adaptive estimation of process noise covariance [22, 23, 24], have been proposed so far, none have shown the results under poor satellite geometry caused by outlier rejection in urban canyons as far as we know. The following sections introduce NLOS signals and satellite geometry in urban canyons.

1.2.2 Multipath and NLOS Signals

This section explains the dominant sources of measurement error in a pseudo range in urban canyons: NLOS and multipath signals. GNSS signals from satellites can be blocked, reflected, and diffracted by nearby objects, such as buildings and walls. NLOS and multipath are different phenomena, as shown in Fig. 1.1. NLOS signal reception occurs when the signal via a direct path is blocked and only via a reflect or diffract path is received. In this thesis, we call a signal via a reflected or diffracted path reflected or diffracted signal. A multipath signal means that a signal via multiple paths is received. This thesis assumes that one of the multiple paths is a direct one.

Their error characteristics vastly differ. Measurement errors due to multipath signals in pseudo ranges are up to half a code chip that depends on the signal structure [25]. For example, half a code chip of the GPS L1C/A signal currently in use is about 150 [m], and one of the GPS L5 signal in the ongoing plan by the U.S. government is about 15 [m]. Using the GPS L5 signal, measurement errors of multipath signals become one-tenth of the ones with the GPS L1C/A signal. The U.S. government will schedule the full operational capability of the GPS L5 signal in the second quarter of 2028 [26]. This explains that we can see an effective solution to measurement errors due to multipath signals coming shortly.

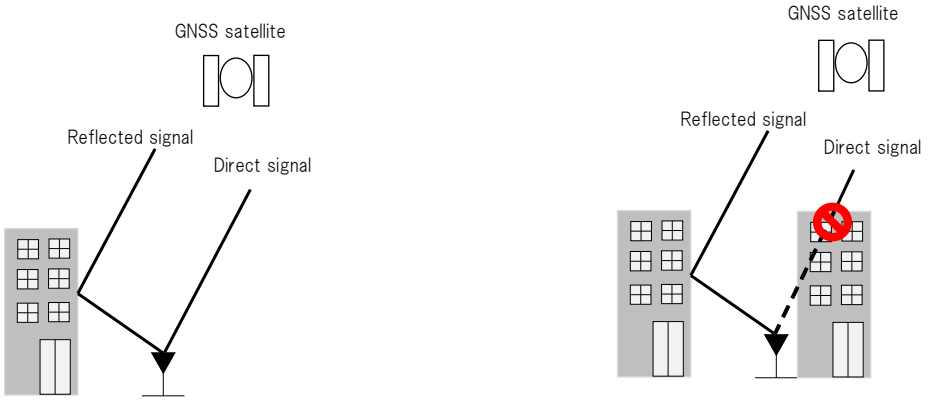

(a) Mutlipath signal:
A signal via multiple paths is received.

(b) NLOS signal:
A signal only via a reflected or diffracted path is received.

Figure 1.1: An illustration of multipath and NLOS signals

Measurement errors due to NLOS signals in pseudo ranges are potentially unbounded in contrast to the ones due to multipath signals. A measurement error due to a NLOS signal is equal to the path delay, which is the difference between the length of the path taken by the signal via a reflected and the (blocked) direct path between a satellite and a receiver. We cannot reduce measurement errors due to NLOS signals even using the GPS L5 signal mentioned above. Measurement errors due to NLOS signals are always positive and tend to be few tens of meters or more, i.e., they would be measurement outliers that can degrade position accuracy considerably. Since the EKF assumes that measurement errors are zero-mean and Gaussian, we must detect and reject measurements obtained from NLOS signals from the filter computation.

Since measurement errors due to NLOS signals depend on path delays, the state-of-the-art predicts path delays by ray tracing with a 3D-city model [13, 14]. Ray tracing is a technique to compute path delays regarding a signal from a satellite as a ray. Accurate ray tracing requires a high computational cost, and mapping cities worldwide is not very practical. Therefore, we consider a simple geometric model of the surrounding environments of a GNSS receiver instead of a 3D city model and assume signal reflection and diffraction models based on the geometric model. These reflection and diffraction models give predicted path delays with a low computational cost. We detect and reject measurement outliers due to NLOS signals based on the predicted path delays.

1.2.3 Satellite Geometry

Satellite geometry is a geometrical distribution of satellites as seen by a receiver and plays a role as translating measurement noise into position errors. Thus, position errors vary depending on satellite geometry even if measurement noise is equally added. This section begins with a simple example of two-dimensional position estimation problem to illustrate how satellite geometry effects on position errors.

This example is presented in the literature [27], which is the problem of two-dimensional position estimation. In this example, a receiver and stations whose positions are known instead of satellites are on the same plane, as shown in Fig. 1.2. The receiver measures its distance from a pair of stations S_1 and S_2 and computes the receiver's position based on trilateration. This example assumes that measurement noise is added to all range measurements. Fig. 1.2 illustrates the measurements from S_1 and S_2 as arcs of circles whose centers are the stations when measurement noise is zero and $\pm\varepsilon$. If the range measurements are perfect, i.e., measurement noise is zero, the receiver's position is determined precisely as lying at the intersection of two arcs centered at S_1 and S_2 as shown in Fig. 1.2. The measurements, however, are imperfect and have noise $\pm\varepsilon$. Trilateration using imperfect measurements results in position uncertainty in position estimates, thus, position errors. Position uncertainty is illustrated in Fig. 1.2 as the shaded region surrounding by arcs, which indicates that position errors can be distributed in this region.

Figs. 1.2a and 1.2b show the regions of position uncertainty from positioning based on trilateration with two different geometries of the stations. In Fig. 1.2a, two stations are distributed so that the lines of sight from a receiver are orthogonal. On the other hand, in Fig. 1.2b, they are located so that their lines of sight are almost parallel. The difference between the two distributions of stations is the angle between the lines of sight of the stations. Thus, the first is acute, and the second is obtuse. Unlike measurements obtained from two orthogonal directions in Fig. 1.2a, only measurements are obtained in a specific direction in Fig. 1.2b. Although measurement noise is equal to $\pm\varepsilon$ in Figs. 1.2a and 1.2b, these figures explain that the difference between the geometry of the stations results in the difference of the region of position uncertainty.

The region of position uncertainty is larger in Fig. 1.2b than in Fig. 1.2a. In particular, it does not evenly spread in each direction. The region of position uncertainty is more widely distributed in a specific direction determined by the geometry of the stations. This explains that

a direction with a larger position error may exist due to the geometry of stations.

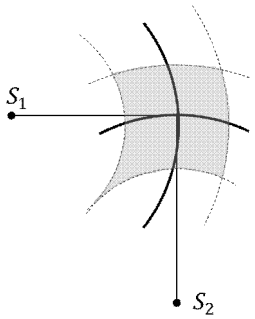

(a) The angle between the line of sight of S_1 and the one of S_2 is orthogonal.

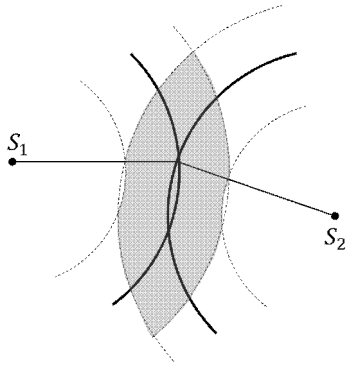

(b) The angle between the line of sight of S_1 and the one of S_2 is obtuse.

Figure 1.2: Examples of satellite geometry of two-dimensional position estimation [27]. The position accuracy depends on measurement noise and geometry of S_1 and S_2. The shaded region represents position uncertainty.

The region of position uncertainty in these examples depends on the geometrical distribution of stations, which shows that the region of position uncertainty in single point positioning could depend on satellite geometry. Fig. 1.3 illustrates examples of satellite geometry, geometrical distributions of satellites seen by a GNSS receiver on the ground. The illustration of satellite geometry is referred to as a sky plot, and Fig. 1.3a is a sky plot on a fish-eye camera image taken in an open sky area. Fig. 1.3a shows that blue dots that are visible satellites with no obstacles in the lines of sight from a GNSS receiver are scattered in almost directions. Since measurements from various directions would be available, this satellite geometry may make the region of position uncertainty small, as shown in Fig. 1.2a.

On the other hand, Fig. 1.3b is a sky plot taken in an urban canyon. The figure illustrates that satellites denoted as red dots are invisible due to buildings from a GNSS receiver on the ground. They are referred to as NLOS satellites, which means satellites with obstacles in the line of sight from a GNSS receiver. Since signals received from NLOS satellites are NLOS signals and should be removed from the position computation, only four measurements from satellites denoted as blue dots would be used for position computation in Fig. 1.3b. The four satellites are in a particular direction; their distribution is biased. The biased distribution, i.e., poor satellite geometry, results in positioning using measurements only in a particular direction.

This explains that the region of position uncertainty may be large and widely distributed in a particular direction, as shown in Fig. 1.2b.

Poor satellite geometry would be inevitable in urban canyons even if we use multiple GNSS constellations concurrently. Although the use of multiple satellite systems increases the number of satellites, satellite visibility may not be enhanced because of limitations due to obstacles in the lines of sight. One practical approach to improve accuracy in urban canyons is the integration of GNSS and other systems typified by GNSS/INS integration. INS stands for Inertial Navigation System. This approach aims to make up for the shortage of visibility of satellites by adding measurements from other sensors, such as inertial or visual sensors. The Kalman filter or extended Kalman filter usually accomplishes the integration.

As mentioned in Sec. 1.2.1, dynamics model uncertainties in the EKF make large position errors unexpectedly. To mitigate these unexpected errors, we often choose process noise covariance heuristically, e.g., through a trial-and-error process. The process noise covariance tends to be large to cover dynamics model uncertainties. In this thesis, we represent the process noise covariance in the EKF as $Q + \delta Q$, where Q is a nominal choice of process noise and δQ is a choice of fictitious noise to cover dynamics model uncertainties. Adding fictitious noise δQ to the dynamics model is called fictitious noise approach.

Our concern is what happens by adding fictitious noise when satellite geometry is poor. The region of position uncertainty with poor satellite geometry would be more widely distributed in a specific direction. Furthermore, fictitious noise might make the region more and more distributed in that direction. It eventually may lead to EKF performance degradation. To avoid degradation, it would be necessary to vary fictitious noise according to satellite geometry. Theoretical analysis and numerical examples show how fictitious noise and poor satellite geometry affect the EKF performance. Moreover, based on the analytical results, we propose a process noise model that chooses fictitious noise varying on satellite geometry.

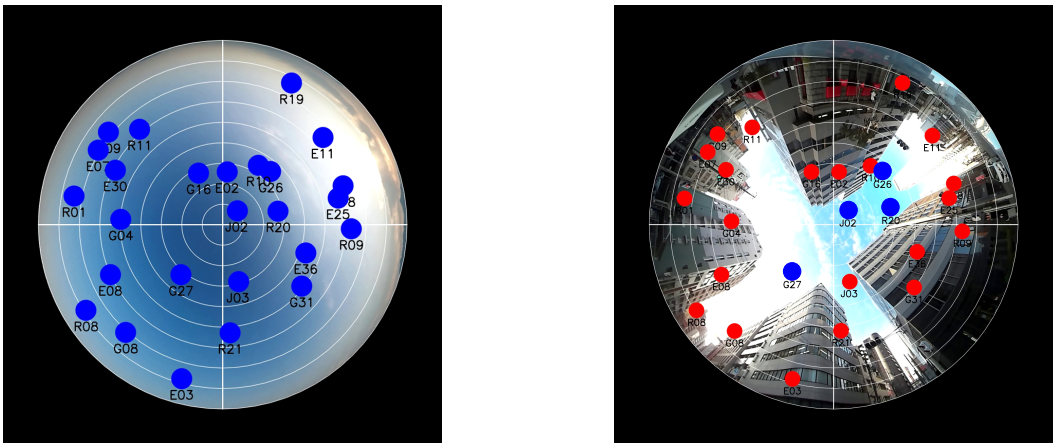

(a) Satellite geometry in an open sky area, Yasu-city, Japan.

(b) Satellite geometry in an urban canyon, Kobe-city, Japan.

Figure 1.3: Satellite geometry as seen by a receiver on a fish-eye camera image. Blue dots are visible satellites and red dots are NLOS satellites. G, E, R, and Q mean GPS, Galileo, GLONASS, and QZSS, respectively.

1.3 Extended Kalman Filter

This section is a mathematical introduction to the extended Kalman filter for single point positioning used in this thesis. In single point positioning, the state vector is chosen as

$$x = (r^{\mathrm{T}}, t_b, \dot{r}^{\mathrm{T}}, \dot{t}_b)^{\mathrm{T}}, \tag{1.1}$$

where r [m] and $\dot{r}$ [m/s] are position and velocity vectors represented in Earth-Centered Earth-Fixed (ECEF) coordinates and t_b [m] and $\dot{t}_b$ [m/s] are a clock bias and a clock drift. The measurement vector consists of pseudo ranges and Doppler frequencies as

$$y = (\rho^{\mathrm{T}}, \dot{\rho}^{\mathrm{T}})^{\mathrm{T}}, \tag{1.2}$$

where pseudo ranges are $\rho^{\mathrm{T}} = (\rho_1, \ldots, \rho_m)$ [m] and Doppler frequencies are $\dot{\rho}^{\mathrm{T}} = (\dot{\rho}_1, \ldots, \dot{\rho}_m)$ [m/s]. The number of satellites is denoted as m. Although the unit of Doppler frequencies is hertz, the unit is converted to meter-per-second by multiplying the wavelength of a signal. State

and measurement equations are given as

$$x_{k+1} = Fx_k + w_k, \tag{1.3}$$

$$y_k = h(x_k) + v_k, \tag{1.4}$$

where

$$F = \begin{pmatrix} I & \delta t I \\ O & I \end{pmatrix}, \tag{1.5}$$

$$h_i(x_k) = \|r_k^i - r_k\| + t_b, \tag{1.6}$$

$$h_{i+m}(x_k) = \frac{(r_k^i - r_k)^{\mathrm{T}}}{\|r_k^i - r_k\|}(\dot{r}_k^i - \dot{r}_k) + \dot{t}_b. \tag{1.7}$$

The ith element of $h(x_k)$ is $h_i(x_k)$ and the state transition matrix is F. The ith satellite position and velocity are denoted as r_k^i and $\dot{r}_k^i$.

Since $h(x_k)$ in (1.4) is nonlinear, the EKF is used to estimate the state. The EKF computation is conducted as follows:

$$\hat{x}_k^- = F\hat{x}_{k-1}^+, \tag{1.8}$$

$$P_k^- = FP_{k-1}^+F^{\mathrm{T}} + Q_k, \tag{1.9}$$

$$\hat{x}_k^+ = \hat{x}_k^- + K_k[y_k - h(\hat{x}_k^-)], \tag{1.10}$$

$$P_k^+ = (I - K_kH_k)P_k^-, \tag{1.11}$$

$$K_k = P_k^-H_k^{\mathrm{T}}(H_kP_k^-H_k^{\mathrm{T}} + R_k)^{-1}, \tag{1.12}$$

where the state estimate and the estimation error covariance matrix are represented as $\hat{x}_k$ and P_k respectively, and K_k is Kalman gain. The superscripts $-$ and $+$ for $\hat{x}_k$ and P_k mean 'prior' and 'posterior'. The measurement matrix H_k is defined as

$$H_k = \left.\frac{\partial h(x_k)}{\partial x_k}\right|_{x_k=\hat{x}_k^-}. \tag{1.13}$$

Nominal noise covariance matrices are Q_k for process noise and R_k for measurement noise. The rest of this section shows where each topic in Sec. 1.2 locates in the EKF.

Sec. 1.2.2 introduces measurement outliers in urban canyons, i.e., NLOS signals. As measurement errors in pseudo ranges obtained from NLOS signals tend to be positive and large, v_k for NLOS signals would not be zero-mean. Furthermore, their covariance matrices may be larger than R_k given as a nominal value. As a result, measurement outliers due to NLOS signals can make biased estimates and large estimation errors. Therefore, they should be removed from the measurement update in (1.10).

Sec. 1.2.3 shows the role of satellite geometry, which is a geometrical distribution of satellites as seen by a GNSS receiver. Since the measurement matrix H_k is the function of satellite positions, it depends on satellite geometry. In urban canyons, H_k tends to degenerate and vary depending on the surrounding environment of a GNSS receiver. Keeping this in mind, the dynamics uncertainties introduced in Sec. 1.2.1 are recalled. To make estimation errors due to dynamics uncertainties small, a larger process noise covariance should be chosen as $Q_k + \delta Q_k$. Although Q_k would be known, it is difficult to choose an appropriate δQ_k heuristically because of the variation of H_k in urban canyons. Furthermore, if δQ_k is chosen naively, it may degrade the EKF performance.

1.4 Outline of This Thesis

This thesis is organized as follows: Chapter 2 presents a NLOS signal rejection method to improve the positioning accuracy of integrated GNSS and INS systems for a vehicle in urban canyons. Measurement errors due to NLOS signals are positive and may be large. Since they have significant negative impacts on EKF performance, we should eliminate measurements from NLOS signals from the EKF. Since measurement errors due to NLOS signals depend on path delays, we can predict them geometrically. Therefore, we assume a signal's reflection and diffraction model based on a simple geometric model of the surrounding environments of a vehicle. The reflection and diffraction model enables the prediction of path delays with a low-computational cost.

A large measurement errors result in a large innovation in the EKF. If an innovation is larger than its predicted path delay, this indicates that the signal via some reflected or diffracted path is received, i.e., a NLOS signal. Comparing innovations with predicted path delays, the method can remove measurements obtained from NLOS signals from the EKF. The prediction

of path delays with the reflection and diffraction is sometimes inaccurate. When innovations from NLOS signals are smaller than the inaccurately predicted path delays, the EKF uses the measurements. We further apply an adaptive-estimation technique to mitigate position errors due to accepted NLOS signals. It estimates measurement noise covariances based on innovations. We implement the EKF with the proposed method and the adaptive estimation technique to examine position accuracy. We demonstrate that the proposed method improves position accuracy in urban canyons with actual data.

Chapter 3 presents performance improvement with a novel process noise model for poor satellite geometry based on theoretical analysis of the estimation error covariance matrix. Due to several studies about NLOS signal rejection, including the method proposed in Chapter 2, almost all NLOS signals can be excluded from calculating the position. However, precise NLOS rejection would make satellite geometry poor, especially in urban canyons. Through numerical simulations and theoretical analysis, we point out that poor satellite geometry leads to unintentional performance degradation of the Kalman filter with a conventional approach to prevent filter divergence. The conventional approach is to bump up the process noise covariance by adding fictitious noise to a dynamics model. When satellite geometry is poor, fictitious noise causes excessive inflation of the estimation error covariance matrix. We propose a novel choice of process noise covariance based on satellite geometry that reduces excessive inflation. Since satellite geometry is represented as measurement matrices in the EKF, the proposed model chooses fictitious noise based on the measurement matrix at each time step. If satellite geometry is poor, the method makes fictitious noise small. Numerical and experimental results demonstrate that the choice of process noise covariance matrix can improve performance even for poor satellite geometry.

Chapter 4 extends the process model derived in Chapter 3 and shows position accuracy improvement through three applications, i.e., stationary GNSS positioning, GNSS/INS positioning, and robot localization with a camera. This chapter begins with the sensitivity analysis of the estimation error covariance due to fictitious noise without assumptions introduced in Chapter 3. Although the sensitivity analysis in Chapter 3 is limited to a linear system whose state transition matrix is an identity matrix, this analysis is for the linearized system of a generic nonlinear system whose state transition matrix is arbitrary. Based on the analysis, this chapter presents two designs of a process noise model using measurement matrices. The first is with

a fixed parameter, and the second is the solution to the problem that minimizes the sum of the square of measurement residuals. For the first design, stationary positioning in an open sky area is performed by simulating poor satellite geometry. These experimental results show that position accuracy improves with the process noise model based on the first design. Vehicle positioning with a GNSS/INS integrated system is performed for the second design. Since the second design chooses the process noise adaptively based on the minimization of measurement residuals, it can improve position accuracy under environments that vary depending on traveling. GNSS/INS positioning results with the second design show that position accuracy improves in open sky areas and urban canyons. Moreover, the second design can be applied to other applications with an EKF. This chapter also shows improvement using the second design for robot localization which often uses an EKF. The EKF with the process noise model based on the second design is implemented in simulations of robot localization. Performance improvement is shown by comparing the estimation results with other process noise models.

Chapter 2

NLOS Signal Rejection Based on Simple Geometric Model

2.1 Introduction

Global Navigation Satellite System (GNSS) is a promising global positioning sensor in intelligent transportation systems, such as navigation systems, road pricing systems with electronic toll collection, and assistance systems for safe driving. GNSS Positioning with the extended Kalman filter (EKF) is inaccurate in urban canyons due to Non-Line-Of-Sight (NLOS) signal reception.

NLOS reception occurs where the signal via a direct path is blocked and the signal is received only via reflection or diffraction. Since measurement errors in pseudo ranges due to NLOS signals depend on path delays, they are always positive and tends to be large. Although the EKF assumes that measurement errors are zero-mean and Gaussian, measurement errors due to NLOS signals violate the assumption.

To improve position accuracy in urban canyons, we should remove measurements obtained from NLOS signals from the computation of the EKF. Since many GNSS receivers are consumer grade, we must achieve the improvement without additional costs. Therefore, we propose a novel algorithm-based method to reject measurements from signals that are supposed to be NLOS signals assuming the signal's reflection and diffraction models.

Inaccuracy in urban canyons is an unsolved GNSS problem. The state-of-the-art is to detect NLOS signals using a 3D city model [13, 14, 28]. The outcomes show that path delays of NLOS

signals can be predicted accurately by ray tracing with a 3D city model, a technique to simulate the propagation of GNSS signals. The prediction is based on a GNSS signal's geometrical reflection and diffraction models. However, a high-computational cost is needed to achieve accurate prediction. Furthermore, mapping cities worldwide to 3D city models is challenging due to cost.

Instead of using the state-of-the-art, we consider applying conventional outlier-rejection techniques. Since measurement errors due to NLOS signals are outliers, conventional methods may be effective. Receiver Autonomous Integrity Monitoring (RAIM) is a scheme to detect outliers using the redundancy of measurements [15, 18, 16, 17]. However, almost all measurements would be outliers in urban canyons, and RAIM may not work. A popular outlier rejection for the EKF is innovation filtering. The innovation filtering may result in biased estimates [9, 19]. Although an improved innovation filtering has been proposed for NLOS signal rejection [19], no results show performance improvement in urban canyons with actual data.

The work aims to develop a NLOS signal rejection method using the fact that measurement errors due to NLOS signals can be predicted by ray tracing. We assume signal's reflection and diffraction models to predict path delays based on a simple geometric model of the surrounding environments of a GNSS receiver. The predicted path delay gives a threshold to detect measurement outliers. Comparing innovations in the EKF with the threshold, we remove measurements obtained from signals that are supposed to be NLOS signals. We believe that this is the first time to propose a NLOS signal rejection method based on path delay prediction without a 3D city model.

Since the prediction is sometimes inaccurate, we cannot remove measurements from NLOS signals completely. Therefore, we concurrently use a noise-adaptive estimation technique in the EKF [22, 23, 29]. In this thesis, we refer to this technique as adaptive EKF. The adaptive EKF reduces the impacts of unexpected measurement errors by making measurement noise covariance for NLOS signals large based on innovations. We integrate the proposed method into the adaptive EKF and demonstrate peformance improvement through experiments with data sets obtained by actual driving in urban canyons.

2.2 Positioning with Adaptive Extended Kalman Filter

The adaptive extended Kalman filter (adaptive EKF) can reduce the impact of NLOS signals on position accuracy by being measurement noise covariance large based on innovations [29, 30]. The adaptive EKF can achieve more accurate positioning in urban canyons. In this study, we apply the adaptive EKF to the tightly coupled integration of GNSS and INS (Inertial Navigation system). INS composes of IMU (Inertial Measurement Unit) and VSP (Vehicle Speed Pulse). This section introduces the adaptive EKF that accomplishes the GNSS/INS integration.

Let state vector be

$$x = (r^{\mathrm{T}}, t_b, \dot{r}^{\mathrm{T}}, \dot{t}_b)^{\mathrm{T}}. \tag{2.1}$$

The position [m] and velocity [m/s] are $r = (r_x, r_y, r_z)^{\mathrm{T}}$ and $\dot{r} = (\dot{r}_x, \dot{r}_y, \dot{r}_z)^{\mathrm{T}}$. They are represented in the Earth-Centered-Earth-Fixed (ECEF) coordinates. The difference between the GPS's clock and a GNSS receiver's clock, namely, the clock bias, is t_b [m]. Further, the time variation of the clock bias is a clock drift $\dot{t}_b$ [m/s]. When we use multiple GNSS constellations concurrently, inter-system biases (ISBs), defined as the difference between the GPS's system clock and other GNSS systems'clock, should be added to the state vector. However, in this work, we assume that we can reduce ISBs enough to ignore by subtracting correction terms obtained from broadcast messages from pseudo ranges. Therefore, we do not add them to the state vector.

We use three types of measurements obtained from GNSS and INS. The first and second ones are pseudo ranges and Doppler frequencies from GNSS. We denote a pseudo range of the ith satellite as ρ_i and a Doppler frequency of the identical satellite as $\dot{\rho}_i$, where $i = 1, \cdots, m$. The third one is a vehicle velocity vector $v_{INS} = (v_x, v_y, v_z)^{\mathrm{T}}$ in the ECEF coordinates from INS.

We define a measurement vector y as

$$y = \begin{pmatrix} \rho_1 \\ \vdots \\ \rho_m \\ \dot{\rho}_1 \\ \vdots \\ \dot{\rho}_m \\ (v_x, v_y, v_z)^{\mathrm{T}} \end{pmatrix} = \begin{pmatrix} h_1(x) + v_1 \\ \vdots \\ h_m(x) + v_m \\ h_{1+m}(x) + v_{1+m} \\ \vdots \\ h_{2m}(x) + v_{2m} \\ \dot{r} + (v_{2m+1}, v_{2m+2}, v_{2m+3})^{\mathrm{T}} \end{pmatrix}, \tag{2.2}$$

where $\{v_1, \cdots, v_{2m+3}\}$ are measurement noise. Measurement functions can be written as

$$h_i(x) = \|r - r_i\| + t_b,\ 1 \le i \le m, \tag{2.3}$$

$$h_i(x) = e_{i-m}^{\mathrm{T}}(\dot{r} - \dot{r}_{i-m}^{SV}) + \dot{t}_b,\ 1 + m \le i \le 2m, \tag{2.4}$$

$$e_{i-m} = \frac{r - r_{i-m}^{SV}}{\|r - r_{i-m}^{SV}\|}. \tag{2.5}$$

The ith satellite's position and velocity are r_i^{SV} and $\dot{r}_i^{SV}$. They are computed from broadcast ephemerides. Assuming that measurement noise is mutually independent, a measurement update of the adaptive EKF can be processed by each element of y [6, 29, 30].

$$\hat{x}_k^+ = \hat{x}_k^- + K_k[y_i - h_i(\hat{x}_k^-)], \tag{2.6}$$

$$P_k^+ = P_k^- - K_{k,i} H_i P_k^-, \tag{2.7}$$

$$K_{k,i} = P_k^- H_i^{\mathrm{T}} (H_i P_k^- H_i^{\mathrm{T}} + R_i)^{-1}. \tag{2.8}$$

The estimate of x_k is $\hat{x}_k$ and its estimation error covariance is P_k. The superscripts, namely, + and −, mean posterior and prior, respectively. The Kalman gain for the ith element y_i is $K_{k,i}$,

and the Jacobian matrix of $h_i(x_k)$ is H_i.

$$H_i = \frac{\partial h_i(\hat{x}_k^-)}{\partial x_k} = (e_i^{\mathrm{T}}, 1, O_{1\times 7}),\ 1 \le i \le m, \tag{2.9}$$

$$H_i = \frac{\partial h_i(\hat{x}_k^-)}{\partial x_k} = (O_{1\times 4}, e_{i-m}^{\mathrm{T}}, 1, O_{1\times 3}),\ 1+m \le i \le 2m, \tag{2.10}$$

$$\begin{pmatrix} H_i \\ H_{i+1} \\ H_{i+2} \end{pmatrix} = \begin{pmatrix} \frac{\partial h_i(\hat{x}_k^-)}{\partial x_k} \\ \frac{\partial h_{i+1}(\hat{x}_k^-)}{\partial x_k} \\ \frac{\partial h_{i+2}(\hat{x}_k^-)}{\partial x_k} \end{pmatrix} = (O_{3\times 8}, I_{3\times 3}),\ i = 2m+1. \tag{2.11}$$

We denote a zero matrix whose size is $l \times n$ as $O_{l\times n}$ and an identity matrix whose size is $l \times l$ as $I_{l\times l}$. The measurement noise variance is R_i for the measurement y_i.

A time update of the adaptive EKF is

$$\hat{x}_{k+1}^- = F_k \hat{x}_k^+, \tag{2.12}$$

$$P_{k+1}^- = F_k P_k^+ {F_k}^{\mathrm{T}} + Q_k, \tag{2.13}$$

$$F_k = \begin{pmatrix} I_{4\times 4} & \Delta t I_{4\times 4} \\ O_{4\times 4} & I_{4\times 4} \end{pmatrix}, \tag{2.14}$$

where F_k is a state transition matrix, Q_k is a process noise covariance. We choose $\Delta t = 1$.

The rest of this section explains the adaptive estimation of R_i. The adaptive estimation of R_i is to estimate measurement noise covarariance using measurements y. The estimate of R_i can be computed as

$$\hat{R}_i = C_k - H_i P_k^- H_i^{\mathrm{T}}, \tag{2.15}$$

$$C_k = \frac{1}{N} \sum_{j=k-N+1}^{k} d_i(j)^2,$$

$$d_i(k) = y_i(k) - h_i(\hat{x}_k^-),$$

where we denote y_i at time step k as $y_i(k)$. Substituting $R_i = \hat{R}_i$ into (2.8), we obtain an adaptive Kalman gain. We call the filter with $\hat{R}_i$ *adaptive EKF*. We choose the time constant as $N = 1$ as well as the literature [29, 30].

Fig. 2.1 shows a process flow diagram of the adaptive EKF. The process flow depends on the

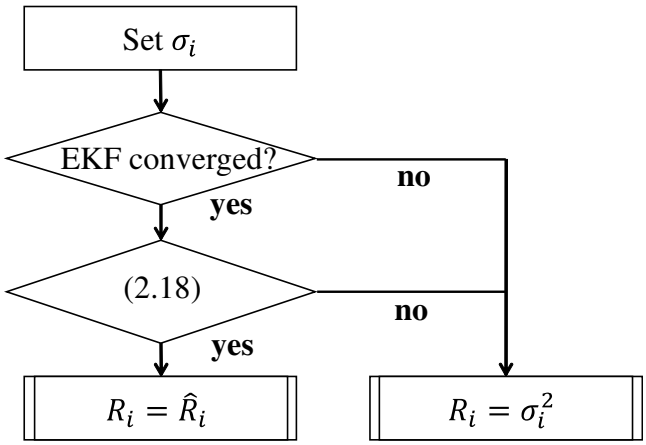

Figure 2.1: Process flow diagram for adaptive EKF

convergence of the adaptive EKF, where the convergence means that the sum of the diagonal elements of P_k^+ corresponding to r is smaller than 9 [m^2] and the time step is over 25 [step]. A standard deviation of measurement noise is σ_i in Fig. 2.1. We denote the Signal-Noise-Ratio (SNR) of the signal of the ith satellite as s_i. Standard deviations of measurement noise of pseudo ranges and Doppler frequencies are approximated as follows [29, 30, 31]:

$$\sigma_i = \sigma_\rho(s_i) = 0.64 + 784e^{-0.142 s_i},\ 1 \le i \le m, \tag{2.16}$$

$$\sigma_i = \sigma_{\dot{\rho}}(s_{i-m}) = 0.0125 + 6767e^{-0.267 s_{i-m}},\ m+1 \le i \le 2m. \tag{2.17}$$

A standard deviation of measurement noise usually depends on a GNSS receiver and an antenna which we use. Equations (2.16) and (2.17) are for a single frequency GNSS receiver (FURUNO GN-8720) and a GNSS antenna (Taoglass AA.171.301111). Since measurement noise due to SNR always exists, $\hat{R}_i$ should be larger than σ_i^2. Therefore, $R_i = \sigma_i^2$ if $\hat{R}_i \le \sigma_i^2$ in Fig. 2.1. Moreover, when $N = 1$, $\hat{R}_i > \sigma_i^2$ is equivalent to

$$|d_i(k)|^2 > H_i P_k^- H_i^{\mathrm{T}} + \sigma_i^2. \tag{2.18}$$

2.3 NLOS Signal Rejection Method

2.3.1 Overview of NLOS Signal Rejection Method

Many obstacles, such as buildings and walls, can block, reflect, and diffract signals from satellites in urban canyons. A NLOS signal is a reflected or diffracted signal without reception of a signal via a direct path. Since a NLOS signal usually arrives later than the blocked signal via a direct path, the measurement error of a NLOS signal is positive and apt to be large. Consequently, the innovation in the EKF of the measurement from a NLOS signal may also be positive and large. Since positive and large measurement errors may bias estimation errors, we should remove measurements obtained from NLOS signals from the adaptive EKF. In this section, we present a novel method that rejects measurements that are supposed to be obtained from NLOS signals based on pseudo-range innovations.

Measurement errors due to NLOS signals depend on path delays. Assuming that the signals are reflected and diffracted based on a simple geometric model of a GNSS receiver's surrounding environments, path delays can be calculated for each location of the GNSS receiver. Since the innovations in the EKF correspond approximately to measurement errors for an accurate prior estimate, the innovations for NLOS signals would be positive and excessively large. We can remove the measurements that are supposed to be from NLOS signals by comparing their innovations with the predicted path delays. We do not use these positive and large innovations at a measurement update step in the adaptive EKF.

The proposed method depends on a simple geometric model. Predicted path delays are sometimes inaccurate. Then, the adaptive EKF may use measurements obtained from NLOS signals whose errors are comparatively small than inaccurately predicted delays. The adaptive EKF could reduce the impact of the accepted NLOS signals by adjusting the measurement noise covariance.

2.3.2 Geometrical Model for NLOS Signals

This section describes a simple geometric model to predict path delays by assuming a geometric model for NLOS signals. We assume that both a satellite and a GNSS antenna locate on the orthogonal plane to the building, as shown in Fig. 2.2. We denote the distance from the building

to the antenna as L and the height of the building as H. The reflection and diffraction occur at the surface and edge of the building, where we denote the reflection and diffraction points as P.

Let the ith satellite's elevation angle be θ_i. We assume that reflection and incidence angles are equal at the reflection point P. The path delay $\varepsilon_1(\theta_i, L)$ due to the reflection is predicted with e_1 and f_1 defined in Fig 2.2a as follows:

$$\varepsilon_1(\theta_i, L) = e_1 - f_1 = 2L\cos\theta_i. \tag{2.19}$$

In addition, the path delay $\varepsilon_2(\theta_i, L, H)$ due to the diffraction is predicted as

$$\varepsilon_2(\theta_i, L, H) = e_2 - f_2 = \sqrt{L^2 + H^2} - L\cos\theta_i - H\sin\theta_i, \tag{2.20}$$

where e_2 and f_2 are distances from the diffraction point P, as shown in Fig. 2.2b. Note that $\varepsilon_1 \geq 0$ and $\varepsilon_2 \geq 0$ because of $0 \leq \theta_i \leq 90$ [deg].

Although we assume that a satellite and a receiver are on the orthogonal plane to the building in the simple geometric model, it does not always hold. The path delay of the reflected signal from a satellite not on the plane is smaller than the predicted delay in (2.19). Furthermore, the diffraction occurs by superimposing each diffracted signal from various diffraction points. This indicates that we cannot predict path delays for diffraction accurately based on the simple geometric model. In this thesis, we design a method to reject measurements whose errors are larger than (2.19) or (2.20). The adaptive EKF can reduce the impact of measurements obtained from accepted NLOS signals on the estimation.

Signals from satellites may reflect or diffract more than once in urban canyons. Since these path delays would be longer than the ones for the single reflection or diffraction, we can reject multiple reflected or diffracted signals based on (2.19) and (2.20). Further, signals also reflect at the surface of the ground. We assume that a GNSS antenna is on the rooftop of a car to block the reflected signals at the ground's surface.

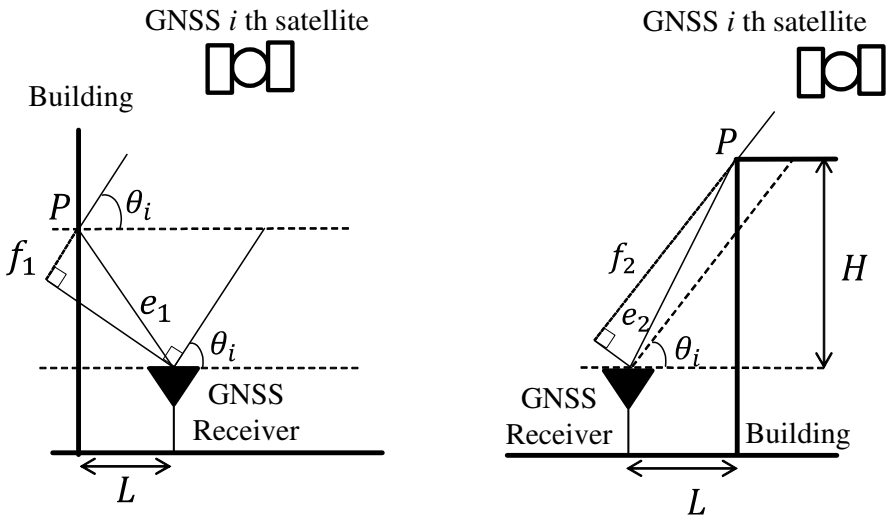

(a) Reflection (b) Diffraction

Figure 2.2: Geometric model of NLOS signals

2.3.3 Threshold for NLOS Signal Rejection

Let the innovation of the pseudo range of the ith satellite be

$$z_{k,i} = y_{k,i} - h_i(\hat{x}_k^-). \tag{2.21}$$

We compute an innovation threshold ε based on the predicted path delay with the simple geometric model and compare innovations with the threshold in the following way:

$$(z_{k,i} > \varepsilon) \wedge (\varepsilon^2 > H_i P_k^- H_i^{\mathrm{T}} + \sigma_{\rho_i}^2), \tag{2.22}$$

where

$$\varepsilon = \min(\varepsilon_1(\theta_i, L), \varepsilon_2(\theta_i, L, H)) - \sigma_{\rho_i}. \tag{2.23}$$

We design the threshold in (2.23) with the geometrical model as follows. From the reflection and diffraction models, we can predict the path delay, as shown in ε_1 or ε_2. Assuming that the predicted measreuements $h_i(\hat{x}_k^-)$ is accurate, innovations mainly consist of actual path delays and noise due to SNR. Therefore, to reject measurements obtained from NLOS signals as much

as possible, we choose the smaller delay (2.19) or (2.20) and then subtract σ_i from the smaller one.

Innovations obtained from NLOS signals would be positive and large. The first term in (2.22) can detect innovations whose actual path delays are longer than predicted ones. If ($z_{k,i} > \varepsilon$), the signals are likely to be received via longer reflected or diffracted paths.

The second term in (2.22) is for avoiding unintentional detection of signals from visible satellites. The threshold in (2.23) may become small depending on L, H, and θ_i. Since measurements are noisy due to SNR, innovations from visible satellites may exceed a small threshold. These measurements should not be removed. To this end, if $z_{k,i} > \varepsilon$, we choose ε so that (2.18) holds, i.e., $\hat{R}_i > \sigma_i^2$.

The value of ε in (2.23) depends on L and H. In this study, we assume that four-wheel vehicles drive in urban canyons and choose $L = 10$ [m] and $H = 150$ [m].

The rest of this section is devoted to checking the sensitivity of the threshold due to L and H through numerical analysis. Fig. 2.3 illustrates the threshold varying on s_i and θ_i for $0 \leq s_i \leq 54$ [dB-Hz] and $0 \leq \theta_i \leq 90$ [deg] with $H = 150$ [m] and $L = \{1, 10, 100\}$ [m]. When the value of ε calculated from (2.23) is negative for a point (s_i, θ_i), we draw $\varepsilon = 0$ at the point instead.

The threshold ε is 1 [m] at a maximum with $L = 1$ [m]. Setting $L = 1$ [m] is not effective for the following reasons. The first is that measurements whose errors depend on small path delays may be negligibly small relative to noise due to SNR. It would be unnecessary to remove these measurements. The second is that real road environments give a larger L than $L = 1$ [m] because of vehicle width and sidewalks.

If $L = 10$ [m] and $L = 100$ [m], the thresholds ε are 20 [m] and 80 [m] at a maximum, respectively. Removing measurements whose path delays are over these values may improve position accuracy. In addition, path delays with $L = 100$ [m] is larger than the ones with $L = 10$ [m], i.e., $\varepsilon|_{L=100} > \varepsilon|_{L=10}$, except for 40 [deg]$\leq \theta_i \leq 50$ [deg]. This indicates that, by setting L to be 10 [m], we can reject most measurements that are obtained from the path delays with $L = 100$ [m] as well as those from the path delays with $L = 10$ [m].

We next compute (2.23) with $L = 10$ [m] and $H = \{10, 150, 250\}$ [m], although we do not illustrate it by figures. The maximum value of ε in (2.23) is 3 [m] at maximum with $H = 10$ [m]. This means that we do not need to remove measurements for the same reason with $L = 1$ [m] and $H = 150$ [m]. For $H = 150$ [m] or 250 [m], the thresholds ε are almost the same at

each point (s_i, θ_i). Most measurements whose path delays are over ε with $H = 250$ [m] can be removed by setting $H = 150$ [m].

From the above results, the choice of $L = 10$ [m] and $H = 150$ [m] could effectively remove measurements obtained from NLOS signals via various paths. Although measurements from NLOS signals whose path delays are relatively small can not be rejected, we apply the adaptive EKF to reduce estimation errors due to accepted NLOS signals.

Fig. 2.4 illustrates path delays in (2.19) and in (2.20) with $L = 10$ [m] and $H = 150$ [m]. When a satellite's elevation angle is less than 68 [deg], measurements are rejected by the prediction in (2.19). Otherwise, they are rejected by the prediction in (2.20). Note that satellite's elevation angles θ_i are obtained from ephemerides broadcasted by satellites.

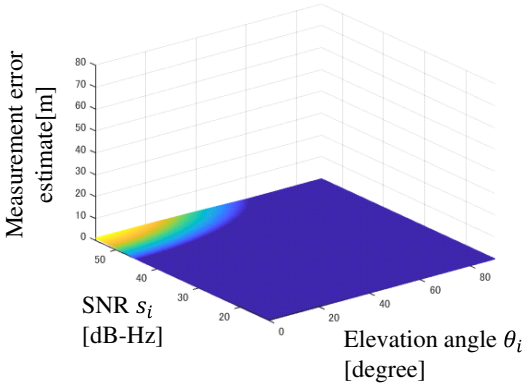

(a) $L = 1$ [m], $H = 150$ [m]

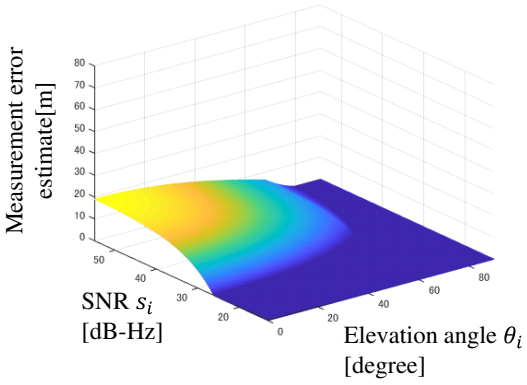

(b) $L = 10$ [m], $H = 150$ [m]

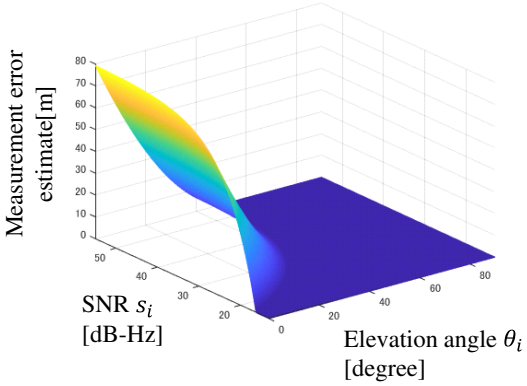

(c) $L = 100$ [m], $H = 150$ [m]

Figure 2.3: Measurement error estimate

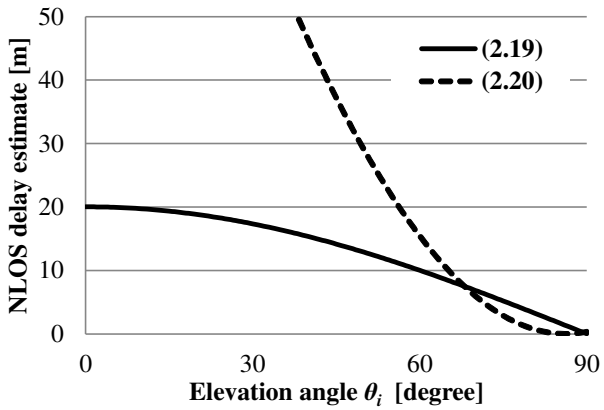

Figure 2.4: Delay estimates by reflection and diffraction for L = 10 [m], H = 150 [m]

2.3.4 Adaptive EKF with NLOS Signal Rejection

We summarize the process flow of the proposed method where the NLOS signal rejection in Sec. 2.3.3 is integrated into the adaptive EKF in Sec. 2.3.2 as in Fig. 2.5. The prediction of path delays can be applied only to pseudo ranges from the satellites. However, the Doppler frequencies from NLOS signals would not be reliable. When a pseudo range from a satellite is rejected by using (2.22), we also reject a Doppler frequency from the same satellite.

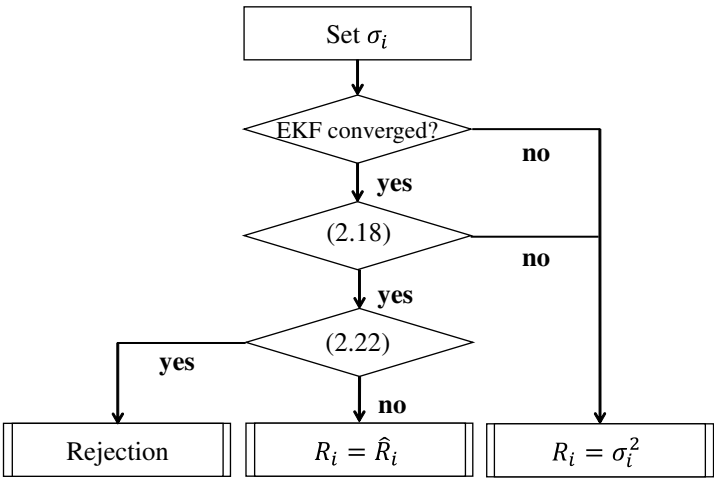

Figure 2.5: Process flow diagram for adaptive EKF with NLOS signal rejection

2.4 Position Accuracy in Urban Canyons

2.4.1 Overview of Experiments

This section shows position accuracy enhancement due to the proposed method through experiments in Shinjuku, Japan, where skyscrapers can block direct signals from satellites and lead to NLOS signal reception. We choose a driving course in Shinjuku as shown in Fig. 2.7. A test vehicle goes round the course to collect raw measurements to compute the vehicle's positions by post processing programs described later. Since position accuracy depends on the number of satellites and their geometry as seen by a GNSS receiver, the test vehicle drove the course three laps at different times, on October 18th, 2018. It took about 25 minutes to drive each lap.

The collected raw measurements include GNSS measurements, ephemerides, vehicle speed, and inertial sensor outputs. GNSS measurements and ephemerides are obtained from a single-frequency GNSS receiver (FURUNO GN-8720). Further, GNSS measurements obtained from GPS/QZSS L1C/A, QZSS L1S, GLONASS L1OF signals compose of pseudo ranges, Doppler frequencies and SLAS (Sub-meter Level Augmentation Service) messages to correct pseudo ranges from GPS/QZSS L1C/A signals. The used inertial sensor is a MEMS 6-axis inertial sensor (Bosch SMI130), and vehicle speed is measured based on the turning of wheels.

To compute the vehicle's positions using the raw measurements in three ways, three post-processing programs are implemented based on the adaptive EKF. The following difference between the three programs in terms of rejection of NLOS signals exists. The first is without the rejection of NLOS signals, the second is with the proposed method to reject NLOS signals, and the third is with the other rejection method that will be introduced in Sec. 2.4.3. The programs are referred to as method A, B, and C, respectively.

In the test vehicle, a reference system (Applanix POS-LV 520) is also installed to obtain accurate positions that can be regarded as true positions of the vehicle. The reference system provides highly accurate positions that are usually an accyracy within 10 [cm] using a ring laser gyroscope, an accelerometer, a precise speed sensor, and high-grade GNSS receivers. Position errors are defined as the difference between the positions with the reference system and the positions with each method. Comparing position errors by the three methods, the improvement due to the proposed method can be shown.

Figure 2.6: Vehicle used for the experiments and a vehicle-fixed coordinate frame

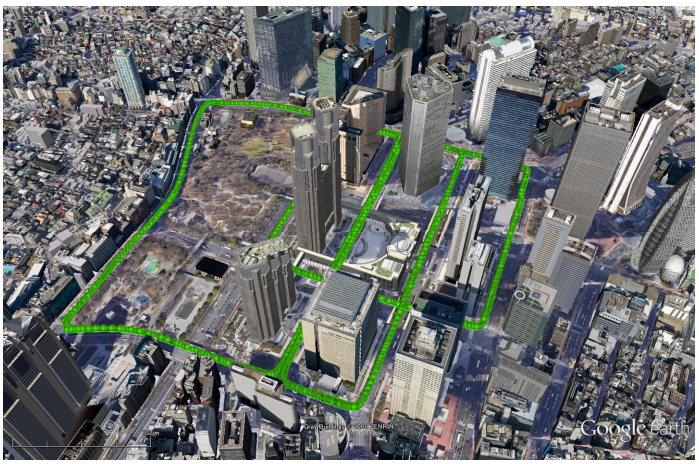

Figure 2.7: Path of the vehicle in Nishi-Shinjyuku area

2.4.2 Exprimental Results of Driving Tests

This subsection shows the position accuracy of each lap with the three methods introduced in the previous subsection. The position accuracy is represented by root mean squared (RMS) errors and peak to peak (P-P) errors computed from the position errors in each lap.

Position errors at time step k represented in the body coordinate as shown in Fig. 2.6 are denoted as $\Delta\tilde{r}_k = (x_k, y_k, z_k)^{\mathrm{T}}$, where x_k, y_k, and z_k are longitudinal (forward), lateral, and vertical errors. For example, using x_k, RMS and P-P errors in the longitudinal direction for each lap can

be computed as follows:

$$\text{RMS error} = \sqrt{\frac{1}{n_p}\sum_{k=1}^{n_p} x_k^2}, \tag{2.24}$$

$$\text{P} - \text{P error} = \max_{1\le k\le n_p}(x_k) - \min_{1\le k\le n_p}(x_k), \tag{2.25}$$

where n_p is the number of positioning in each lap.

Tables 2.1, 2.2, and 2.3 show RMS and P-P errors for each lap with the three methods. We can see that the RMS and P-P errors for method B are smaller than the method A in the tables. This explains that position accuracy for method B with NLOS signal rejection is better than method A without NLOS signal rejection. The reason for the better results with method B would be because some measurements from NLOS signals that may cause large position errors are removed with the proposed method. Note that position errors in z-axis is larger than in the x-axis and y-axis. This is caused by satellite geometry as seen by a GNSS receiver [32].

Table 2.1: RMS and P-P values for Lap 1

	RMS			P-P		
	x [m]	y [m]	z [m]	x [m]	y [m]	z [m]
(A)	2.77	2.75	6.28	17.95	15.60	34.50
(B)	2.51	2.59	4.82	14.98	13.14	20.94
(C)	2.43	2.40	5.19	14.07	12.59	22.14

(A) = method A without NLOS rejection
(B) = method B with NLOS rejection
(C) = method C with innovation filtering

Table 2.2: RMS and P-P values for Lap 2

	RMS			P-P		
	x [m]	y [m]	z [m]	x [m]	y [m]	z [m]
(A)	3.86	2.75	7.23	30.80	19.40	49.47
(B)	2.95	2.53	6.28	21.00	16.53	38.38
(C)	3.38	2.51	6.14	27.66	18.75	35.79

2.4.3 Discussion

This subsection discusses four topics based on additional experiments and through further data analysis: (1) The effectiveness due to method B. (2) The comparison with other methods. (3)

Table 2.3: RMS and P-P values for Lap 3

	RMS			P-P		
	x [m]	y [m]	z [m]	x [m]	y [m]	z [m]
(A)	4.48	3.86	11.65	26.79	22.33	35.10
(B)	3.46	3.25	8.05	22.30	15.82	28.39
(C)	6.48	5.33	15.21	31.98	30.79	45.20

The accuracy varying on the parameters, L and H, in the proposed model. (4) The accuracy with the proposed method in open-sky areas.

Effectiveness Due to NLOS Signal Rejection

This subsection examines the number of rejected measurements and the locations of satellites of the rejected measurements. Table 2.4 shows the number of measurements used in the experimental results introduced in Sec. 2.4.2 and computes the average number of measurements used in the n_p positionings in each lap.

In method A, fourteen measurements are used on average in all laps. However, method B uses ten or eleven measurements. This shows that method B removes three or four measurements on average in all laps. Since method B improves position accuracy, it could remove measurements that can degrade position accuracy, that is, NLOS signals. Further, Table 2.4 indicates that method B based on (2.22) can prevent degrading position accuracy with excessive rejections of measurements.

Table 2.4: Average number of signals used in positioning

	(A)	(B)	(C)
Lap 1	14.1	10.4	9.1
Lap 2	14.8	11.1	8.5
Lap 3	14.7	11.2	9.0

We next examine details of data in an area where position errors with method B are reduced compared to method A to show which measurements were rejected. The area, Tokyo metropolitan road 432, is illustrated in Fig. 2.8. The yellow arrow on the Fig. 2.8 designates the direction of travel of the test vehicle. We can see a park and buildings on the left and right sides along the direction of travel. The distance from the vehicle to the buildings is about 15 [m], and their height is about 167 [m].

In Fig. 2.8, we can see that position errors with method A are 11 [m] and the ones with method B are 5 [m]. Position errors with method B in this area become in half compared to method A. Besides, green dots (reference positions) distribute across the two roads in Fig. 2.8. This is caused by changing driving lanes, not position errors with the reference system.

We define the utilization rate of signals to show how often each signal is used in this area as follows:

$$u_{SV} = 100 \times \frac{M_{SV}}{F}. \tag{2.26}$$

The subscript SV is the satellite number of the received signal. The travel time along this road shown in Fig. 2.8 is F. The number of the use of a signal from the SVth satellite is M_{SV} during driving this road. We can see that the utilization rates of signals from satellites located on the left side of the direction of travel in Fig. 2.9 are lower than the ones for the other satellites. Trees in the park would block signals from satellites on the left side, and the buildings on the right would reflect the signals. The situation can be consistent with our assumption of NLOS signal reception. Thus, the proposed method based on (2.19) could reject the left-side satellites' signals. Fig. 2.9 also shows that satellites whose elevation angles are higher than 60 [deg] are rejected. Since trees in the park or skyscrapers can block direct signals from high-elevation satellites [33], these satellites' signals may be NLOS signals. Since the rejection due to a cut-off elevation angle cannot remove these signals, it would be one advantage of the proposed method to remove signals from high-elevation satellites.

Performance Comparison with Innovation Filtering

The literature [9, 19] introduces a generic outlier rejection method for Kalman Filter. We refer to the method as innovation filtering. The innovation filtering rejects measurement outliers whose innovations are more significant than a threshold. We integrate the innovation filtering into the adaptive EKF, and then compare position accuracy with the innovation filtering to the one with the proposed method.

We denote the adaptive EKF with the innovation filtering as method C. In method C, we

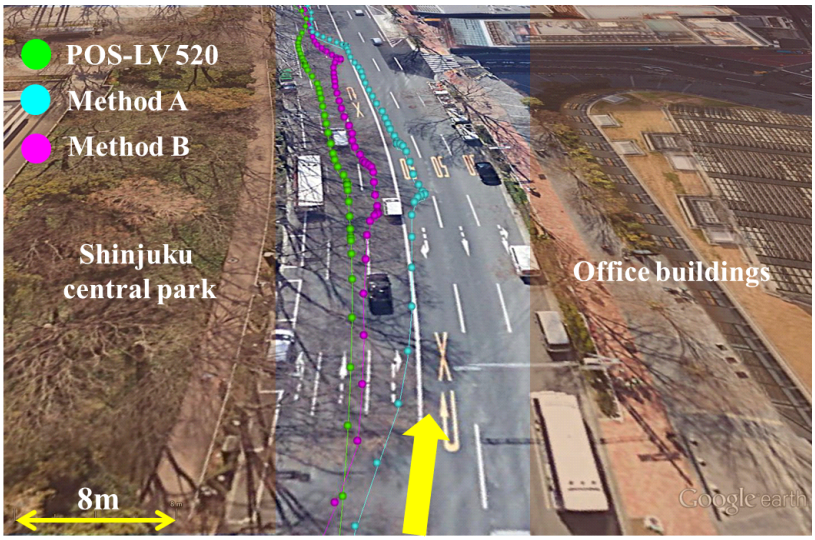

Figure 2.8: Positioning results with the method A(blue dots) and the method B(magenta dots)

replace (2.22) with

$$\frac{z_{k,i}^2}{(H_i P_k^- H_i^{\mathrm{T}} + \sigma_{\rho_i}^2)} > \kappa^2. \tag{2.27}$$

The left side in (2.27) is the normalized innovation of the signal from the ith satellite. The denominator is the analytical variance of the innovation $z_{k,i}$. A fixed threshold is κ and method C rejects measurements whose normalized innnovation is more significant than κ.

The literature [9, 19] has pointed out that the innovation filtering can make biased estimation errors if measurement errors are always positive, like NLOS signals. We choose $\kappa = 4$ as the literature [19] proposes and shows RMS and P-P errors for method C in Tables 2.1, 2.2, and 2.3. Moreover, the number of satellites that are used in positioning is shown in Table 2.4. Although position accuracy improves in the first and second laps, it degrades in the third lap even compared with the ones for method A. On the other hand, method B improves estimation accuracy in all laps. Since the number of satellites for method B is larger than the one for method C, this indicates that method B detects NLOS signals more accurately using (2.22).

In this work, we implement method C in the adaptive EKF. Since the adaptive EKF affects the estimation error covariance matrix P_k^+, it also has an impact on the threshold to reject signals. It is necessary to discuss the behavior for the combination of the adaptive EKF and the innovation filtering. Further, although (2.22) is for rejecting measurements outside of the assumed distribution, (2.27) is for passing through measurements that are distributed inside of

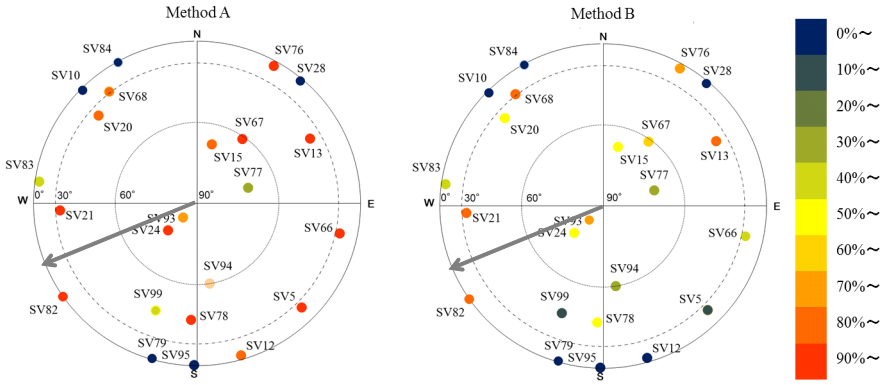

Figure 2.9: Utilization rate of each satellite. Satellites are plotted by dots according to their azimuth and elevation. The color of each satellite shows the utilization rate divided into 10 sections. N,S,E and W mean north, south, east and west respectively. SV1 ~ 32 are the GPS satellites, SV65 ~ 88 are the GLONASS satellites, and SV193 ~ 196 are the QZSS satellites. The elevation and azimuth angles of satellites are obtained from broadcast ephemeirdes. The arrow means the direction of the vehcle(246.8 [deg]).

the assumed distribution. We believe that using different methods simultaneously leads to more accurate positioning. We will further investigate the possibility of improvement in future works.

Instead of using the innovation filtering, it would be possible to replace (2.22) with $z_{k,i}^2 > \epsilon_c$, where ϵ_c is a fixed threshold. We chose an appropriate ϵ_c through a trial-and-error process based on the driving data. The results with a fixed ϵ_c showed that position accuracy is better than method A and almost the same as method B. Although position accuracy is almost the same as method B, the number of rejected signals with $z_{k,i}^2 > \epsilon_c$ is larger than the one with method B. Method B improves accuracy with a fewer number of eliminated signals than the method with $z_{k,i}^2 > \epsilon_c$. This shows that method B would remove signals effectively. It should be noted that method B may not eliminate signals whose innovations are large because of the second term in (2.22), even if they should be removed. We will further investigate and improve the proposed method for the second term in (2.22) by using the innovation filtering concurrently.

Sensitivity of Position Accuracy Due to L and H

Sec. 2.3.3 shows the sensitivity of the threshold due to a significant change of L and H. The results of the sensitivity analysis show that $(L, H) = (10, 150)$ [m] would be an appropriate value to remove signals via various reflected paths. We here show the sensitivity of position accuracy due to a slight shift in L and H with the same data above used.

Table 2.5: RMS and P-P values for (a) $(L,H) = (25,150)$ [m] and (b) $(L,H) = (10,130)$ [m], with the method B for Lap 3

	RMS			P-P		
	x [m]	y [m]	z [m]	x [m]	y [m]	z [m]
(a)	3.33	3.23	7.31	21.78	16.25	27.97
(b)	3.43	3.15	7.78	22.17	16.51	28.18

We choose $(L,H) = (25,150)$ and $(L,H) = (10,130)$ [m] and examine position accuracy with method B for Lap 3. Table 2.5 shows RMS and P-P errors with $(L,H) = (25,150)$ and $(L,H) = (10,130)$ [m]. Compared to the results in Table 2.3, Table 2.5 shows that method B with both choices of (L,H) improves position accuracy from method A. This explains that method B improves position accuracy, even if we approximately choose L and H.

Position Accuracy in Open Sky Area

Method B assumes reflection and diffraction models based on a simple geometric model of the surrounding environments of a vehicle in urban canyons. We examine position accuracy in open sky areas to show no unexpected degradation with method B due to the rejection of measurements. Open sky areas give good satellite visibility and satellite signals may rarely block. Thus, NLOS signal reception would not mostly occur.

We drove around Yoyogi - Park, Tokyo, an open sky area. Fig. 2.10 shows that the results of positioning with method A and B. The difference between positioning results with method A and B is slight. The dots on Fig. 2.10 for method A and B are overlapped. The average number of rejected satellites is less than one in positionings with method B around the park. Since method B does not reject signals whose measurement errors are small, position accuracy with method B would not degrade in open sky areas.

2.5 Conclusion

In this chapter, we proposed a novel method to reject the measurements obtained from NLOS signals based on a model where the signals are reflected and diffracted in a simplified surrounding environment. The models give a threshold to remove measurements from the adaptive extended Kalman filter. If an innovation in the adaptive EKF exceeds the threshold, it is re-

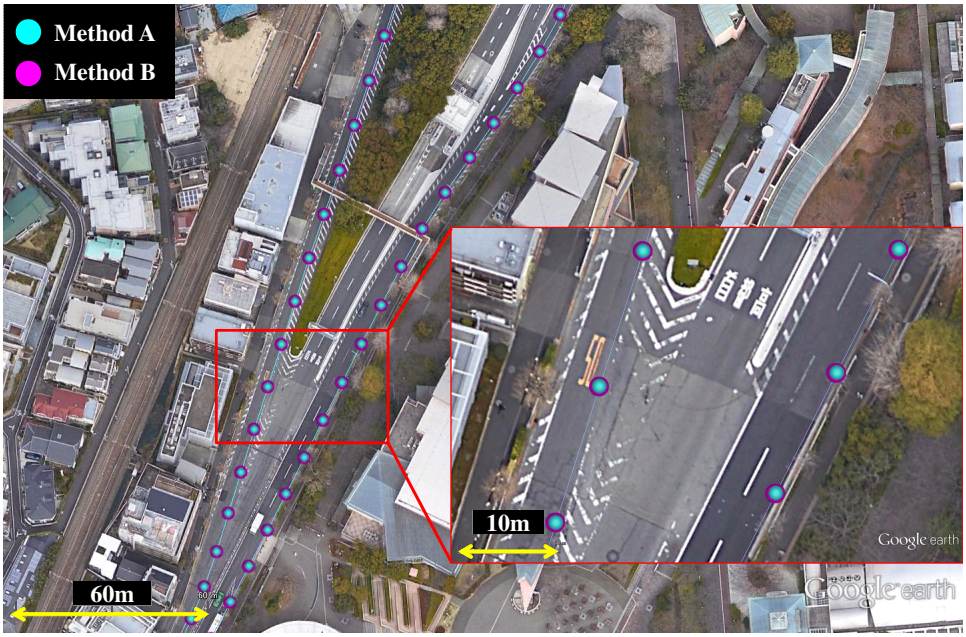

Figure 2.10: Positioning results near Yoyogi-Park. (Blue points for the method A and pink points for the method B are almost overlapped.)

moved from the filter computation. We performed experiments in urban canyons and showed that the method can improve position accuracy. Moreover, position accuracy with the proposed method does not degrade in open sky areas. The proposed method does not require additional external sensors, e.g., cameras, and can be applied to extensive surrounding environments of a vehicle.

Chapter 3

Performance Improvement with Process Noise Model for Poor Satellite Geometry

3.1 Introduction

Global Navigation Satellite System (GNSS) is an absolute positioning sensor widely used in various applications. GNSS can determine the location of a receiver based on trilateration by using pseudo-ranges between GNSS satellites and a receiver. It is well-known that positioning performance is dramatically degraded because of Non-Line-Of-Sight (NLOS) signal reception in urban environments [7]. NLOS signal reception occurs where tall buildings block Line-Of-Sight (LOS) direct signals from satellites and the signals are received via reflection and/or diffraction. Pseudo ranges obtained from NLOS signals have tendency to be positive outliers [29, 30], because they are computed from the times of flight of the signals. We, therefore, have to reject NLOS signals from position calculation to improve positioning accuracy in urban environments.

Many researchers have developed NLOS signal rejection methods based on measurement residuals [19, 9, 34], fisheye-camera images [35, 36], 3D city maps with ray tracing [14, 28, 37], and so on. It is possible to reject NLOS signals precisely by applying these methods, and then positioning performance can be improved if a sufficient number of satellites are available. Unfortunately almost all signals in dense urban environments could be NLOS signals. The precise rejection of NLOS signals would greatly reduce the number of satellites available in position calculation, thus cause poor satellite geometry, that is, a biased distribution of visible satellites.

Since accuracy of trilateration is highly dependent on the geometric locations of the satellites as seen by a receiver, poor satellite geometry may result in inaccurate positioning. The above mentioned studies have not sufficiently dealt with the problem of poor satellite geometry caused by NLOS rejection. Taking satellite geometry into account in addition to NLOS rejection might yield more accurate positioning.

The estimate of position usually can be obtained by using Kalman filter [5, 38] under some assumptions about process model, measurement model, and noise statistics. However, the estimation by Kalman Filter may suffer from its divergence [6, 39]. A typical example of filter divergence occurs when the assumptions are inconsistent with actual model. The estimation error covariance becomes excessively small due to the model errors, the filter gain is therefore small, and eventually the filter begins to ignore new measurements. As a consequence, estimate errors will be biased or diverge. Since these model errors are in general unknown and unbounded, it is difficult to solve the divergence theoretically.

A conventional and simple technique [40] to prevent filter divergence is to bump up process noise covariance to cover the uncertainty of model errors. This technique is easy to implement, that is, we have only to add fictitious process noise covariance to its nominal value. Since this technique is largely heuristic, it is important to discuss its effect not only on divergence but also on filter performance.

In the application of the technique to GNSS positioning [9], bumping up process noise covariance inflates estimation error covariance in the prediction step. The inflated covariance can be reduced by processing observations right after the inflation, if satellite geometry is good. Consequently, the size of estimation error covariance is kept to be large enough to avoid the divergence, but not too large. However, if satellite geometry is poor, what would be happened? The inflation cannot be reduced in a certain direction according to the geometry, and the estimation error covariance would become larger than expected. This unexpectedly large covariance would lead to inaccurate positioning.

A proper choice of the process noise covariance has been of interest to many researchers so far. Some filtering techniques have been developed to have an estimation error covariance that is insensitive to changes in process noise covariance, through the steady-state analysis of estimation error covariance [41, 42]. Furthermore, also noise-adaptive estimation techniques have been proposed [43, 44, 23]. However, these techniques cannot handle with preventing the

performance degradation caused by poor satellite geometry, because they do not take satellite geometry into account.

There are some approaches that can be used to avoid the performance degradation caused by poor satellite geometry. Constrained Kalman filter techniques can be utilized to mitigate the degradation [45, 46]. The techniques automatically detect poor satellite geometry, and estimate only the state variables for which poor satellite geometry would not cause the degradation. However, it is difficult to choose a proper threshold for detecting poor satellite geometry in a heuristic manner. The positioning degradation can also be resolved by integrating other sensors such as IMU (Inertial Measurement Unit) and LiDAR (Light Detection and Ranging) device into GNSS Kalman filter [9]. The observations from the sensors can compensate for the lack of information due to poor satellite geometry. However, adding those sensors is often unacceptable in terms of cost and installation space.

The main contribution of this work is twofold. First, we clarify the fundamental relationship between process noise and satellite geometry through theoretical analysis. The analysis shows that the inflation of estimation error covariance by fictitious process noise can be unexpectedly large for poor satellite geometry. Secondly, from the theoretical results, we propose a novel way to choose process noise covariance based on satellite geometry in order to remove the unexpected inflation. Comparing with the approaches mentioned above, our approach is based on a theoretical sensitivity analysis, and does not require other additional sensors.

3.2 Positioning from Poor Satellite Geometry

3.2.1 Poor Satellite Geometry Caused By NLOS Signal Rejection

This section illustrates the problem caused by poor satellite geometry. Fig. 3.1 is an example of a satellite sky plot superimposed on a fisheye-camera image taken at Kobe city, Japan. As shown in Fig. 3.1, tall buildings surround the location and can block almost all direct signals from satellites. We suppose that satellites overlapped on buildings are NLOS satellites (denoted as red dots), and the others are LOS satellites (denoted as blue dots). If complete NLOS satellite rejection is done, only the five satellites will remain. We can see that remained satellites are located along the northeast direction. If we bump up process noise covariance to avoid the filter

divergence, position uncertainty in the direction of southeast will become larger unintentionally. Although it will be explained from a theoretical point of view in Section 3.3, we will show it through a simulation study in this section.

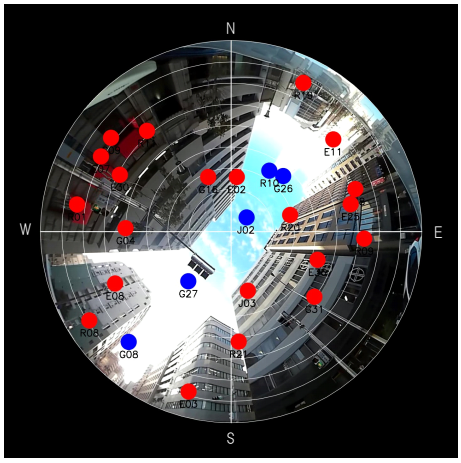

Figure 3.1: A sky plot onto a fisheye-camera image taken at Kobe city, Japan. A blue dot represents a LOS satellite and a red dot represents a NLOS satellite. N, S, E, and W stand for North, South, East, and West, respectively.

3.2.2 Motivating Examples for Poor Satellite Geometry

In order to show the problem clearly, we present some simulation results using a simplified model for GNSS, under the assumption that five satellites are stationary and located in poor satellite geometry. A GNSS receiver is also assumed to remain stationary on a horizontal surface. Let the dynamical system and the linear measurement equations be as follows:

$$x_k = x_{k-1} + w_k, \tag{3.1}$$

$$y_k = H x_k + v_k, \tag{3.2}$$

$$H = \begin{pmatrix} -\cos\theta_1 \sin\psi_1 & -\cos\theta_1 \cos\psi_1 & -\sin\theta_1 \\ \vdots & \vdots & \vdots \\ -\cos\theta_5 \sin\psi_5 & -\cos\theta_5 \cos\psi_5 & -\sin\theta_5 \end{pmatrix},$$

where $x_k = (r_e, r_n, r_u)^{\mathrm{T}}$ is a position vector represented in the ENU (East-North-Up) coordinates, y_k is a measurement vector composed of ranges from five satellites to a receiver, H is a 5×3 measurement matrix, v_k is a measurement noise vector, and w_k is a process noise vector. We

assume that $x_0 \sim N(0, I)$, $E\{w_k\} = E\{v_k\} = 0$, $E\{w_k w_l^{\mathrm{T}}\} = Q(k)\delta_{kl} = 0.01I\delta_{kl}$[1], and $E\{v_k v_l^{\mathrm{T}}\} = R(k)\delta_{kl} = 4I\delta_{kl}$. $E\{a\}$ is the expectation of a random variable a, and δ_{kl} is the Kronecker delta. w_k and v_k are produced numerically by random number. θ_i and ψ_i are the elevation angle and the azimuth angle of the ith satellite, respectively.

The five satellites are supposed to be located as shown in Figure 3.2. Their elevation angles are $\theta = \{90, 15, 15, 15, 15\}$ [degree], and their azimuth angles are $\psi = \{0, 40, 50, 220, 230\}$ [degree]. The satellites are located along the northeast direction as in Figure 3.1. We can determine whether the satellite geometry[2] is poor or not by evaluating the eigenvalues of $H^{\mathrm{T}}H$; If one of eigenvalues is zero or close to zero, $H^{\mathrm{T}}H$ is singular or almost singular, and such a satellite geometry is called poor. The eigenvectors of $H^{\mathrm{T}}H$ corresponding to the minimum and maximum eigenvalues coincide with a southeast direction and a northeast direction in this satellite geometry (the locations of the five satellites were chosen so that the directions of the eigenvectors of $H^{\mathrm{T}}H$ are intuitively obvious. Although this work presents the results when the elevation angles θ_i for four satellites are 15 degrees ($i = 2, \cdots, 5$), similar numerical results are obtained for $\theta_i = 0, 30$, or 45 degrees).

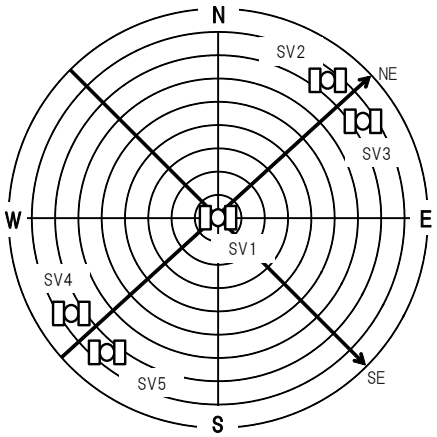

Figure 3.2: A sky plot for simulation study. SV, NE, and SE stand for Satellite Vehicle, a northeast direction, and a southeast direction respectively.

Simulation results are obtained by Kalman filter that will be described in Section 3.3, with

[1]Since the position vector x_k is stationary, w_k and $Q(k)$ should be zero originally. However, such a choice of w_k and $Q(k)$ would lead to numerical problems of Kalman filter [1]. To avoid the problems, small w_k and $Q(k)$ are usually assumed to exist. In this work, we suppose that "true process noise" denoted by w_k and $Q(k)$ includes this inevitable small noise.

[2]It is well-known that DOP (Dilution of Precision) parameters characterize satellite geometry. In this work, we attempt to integrate satellite geometry into Kalman filter.

two parameter settings. For setting (1), the process noise covariance $\tilde{Q}$ in Kalman filter is chosen as the true one Q. For setting (2), $\tilde{Q}$ is set by adding fictitious noise δqI to Q. Fig. 3.3 shows the estimated positions in a r_e-r_n plane that were obtained by repeating the filter computation 1000 times with different initial position estimates and different noise realizations.

Table 3.1 shows standard deviations that are computed by projecting the plotted estimate errors to two eigenvectors of $H^{\mathrm{T}}H$, where σ_{SE} and σ_{NE} are standard deviations in the directions of two eigenvectors, southeast direction and northeast direction. The differences between σ_{SE} and σ_{NE} mainly come from the satellite geometry in both (1) and (2). Since there is no model error in these simulations, the plotted estimation errors spread depending on the satellite geometry and the settings of process and measurement noises, and are consistent with the estimation error covariance calculated from Kalman filter. However, we should note that the values of σ_{SE}/σ_{NE} in (1) and (2) are quite different—3.48 and 4.22, respectively. This means that the estimation errors in southeast direction are spread more widely than in northeast direction even though the fictitious process noise is added equally in each direction. The fictitious noise to avoid the filter divergence makes the estimation errors worse unintentionally in the southeast direction that corresponds to the eigenvector of the smallest eigenvalue.

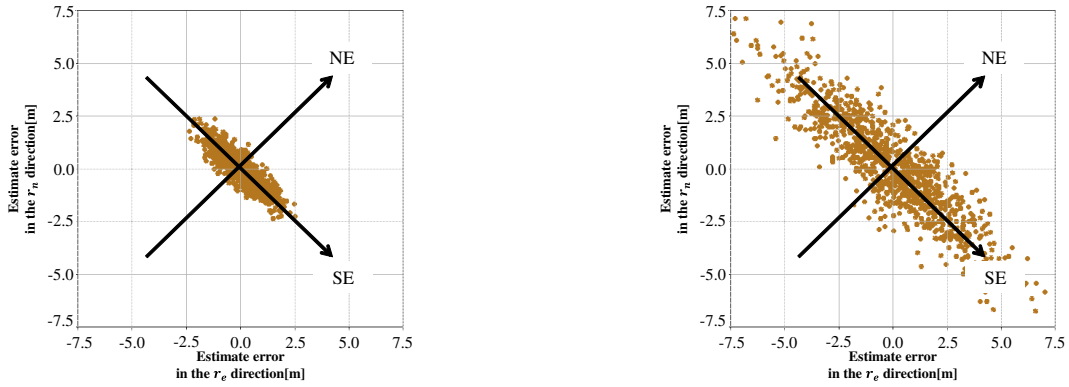

(a) Filter results with setting (1)

(b) Filter results with setting (2)

Figure 3.3: Estimated positions obtained by repeating Kalman filter computation 1000 times.

We devote Section 3.3 to reveal the theoretical relationship among the inflation of estimation error covariance, process noise covariance, and satellite geometry. Then, in Section 3.4, we will describe how to reduce the unnecessary inflation of estimation error covariance.

Table 3.1: Standard deviations of estimate errors.

Settings	**(1)**	**(2)**
σ_{SE}[m]	1.08	3.38
σ_{NE}[m]	0.31	0.80
σ_{SE}/σ_{NE}	3.48	4.22

3.3 Sensitivity Analysis of Estimation Error Covariance

We consider a linear system and Kalman filter for it:

$$x_k = F_{k-1}x_{k-1} + w_k, \tag{3.3}$$

$$y_k = H_k x_k + v_k, \tag{3.4}$$

$$\hat{x}_k^- = F_{k-1}\hat{x}_{k-1}^+, \tag{3.5}$$

$$P_k^- = F_{k-1}P_{k-1}^+ F_{k-1}^{\mathrm{T}} + \tilde{Q}_k, \tag{3.6}$$

$$\hat{x}_k^+ = \hat{x}_k^- + K_k(y_k - H_k\hat{x}_k^-), \tag{3.7}$$

$$P_k^+ = [(P_k^-)^{-1} + H_k^{\mathrm{T}}\tilde{R}_k^{-1}H_k]^{-1}, \tag{3.8}$$

$$K_k = P_k^- H_k^{\mathrm{T}}[H_k P_k^- H_k^{\mathrm{T}} + \tilde{R}_k]^{-1}, \tag{3.9}$$

where we use the same notations as in (3.1) and (3.2), and variables in the filter are listed in Table 3.2. We suppose that $\tilde{R}_k$ and $\tilde{Q}_k$ are different from their true ones R_k and Q_k.

First of all, we derive the difference equation between P_{k-1}^+ and P_k^+. Since $H_k^{\mathrm{T}}\tilde{R}_k^{-1}H_k$ is symmetric, it can be diagonalized by an orthogonal matrix G, i.e., $H_k^{\mathrm{T}}\tilde{R}_k^{-1}H_k = G_k\tilde{\Lambda}_k G_k^{\mathrm{T}}$, where $\tilde{\Lambda}_k$ is a diagonal matrix whose diagonal elements are the eigenvalues of $H_k^{\mathrm{T}}\tilde{R}_k^{-1}H_k$. Now we make the following assumptions:

Assumption 3.3.1. *$F_k = I$.*

Assumption 3.3.2. *$G_k^{\mathrm{T}}P_{k-1}^+G_k$ and $G_k^{\mathrm{T}}\tilde{Q}_k G_k$ are diagonal.*

We drop the notation $_k$ for simplicity except for P_{k-1}^+ and P_k^+. Using Assumption 3.3.1 and substituting $H^{\mathrm{T}}\tilde{R}^{-1}H = G\tilde{\Lambda}G^{\mathrm{T}}$ into (3.8), we can rewrite it as

$$\begin{aligned} P_k^+ &= [(P_k^-)^{-1} + H^{\mathrm{T}}\tilde{R}^{-1}H]^{-1} \\ &= G[(G^{\mathrm{T}}P_{k-1}^+G + G^{\mathrm{T}}\tilde{Q}G)^{-1} + \tilde{\Lambda}]^{-1}G^{\mathrm{T}}. \end{aligned} \tag{3.10}$$

Table 3.2: Filter variables.

Variable	Definition
$\hat{x}_k^-$	Prior estimate
$\hat{x}_k^+$	Posterior estimate
P_k^-	Prior estimation error covaraiance
P_k^+	Posterior estimationerror covaraiance
F_k	State transition matrix
y_k	Measurement vector
H_k	Measurement matrix
$\tilde{R}_k$	Measurement noise covariance
$\tilde{Q}_k$	Process noise covariance
K_k	Filter gain matrix
k	Time step

Multiplying G^{T} and G to both sides of (3.10), we obtain

$$G^{\mathrm{T}}P_k^+G = [(G^{\mathrm{T}}P_{k-1}^+G + G^{\mathrm{T}}\tilde{Q}G)^{-1} + \tilde{\Lambda}]^{-1}. \tag{3.11}$$

From (3.11) and Assumption 3.3.2, $G^{\mathrm{T}}P_k^+G$ is also diagonal. Then the iith element of $G^{\mathrm{T}}P_k^+G$ denoted as $\tilde{P}_{i,k}$ can be written as

$$\tilde{P}_{i,k} = \frac{\tilde{P}_{i,k-1} + \tilde{q}_i}{1 + \tilde{\lambda}_i(\tilde{P}_{i,k-1} + \tilde{q}_i)}, \tag{3.12}$$

where $\tilde{\lambda}_i$ is the iith element of $\tilde{\Lambda}$, and $\tilde{q}_i$ is the iith element of $G^{\mathrm{T}}\tilde{Q}G$. Equation (3.12) is the difference equation of estimation error covariance from $k-1$ to k, and shows that $\tilde{P}_{i,k}$ depends on $\tilde{q}_i$ and $\tilde{\lambda}_i$, that is, process noise covariance and satellite geometry.

By using the true process noise covariance Q and a fictitious process noise δq, we represent $\tilde{Q}$ as $\tilde{Q} = Q + \delta q$. It is assumed that each component in $\tilde{Q}$ is diagonalized by G, that is, $G^{\mathrm{T}}QG$ and $G^{\mathrm{T}}\delta qG$ are diagonal matrices. Then, (3.12) can be rewritten as:

$$\tilde{P}_{i,k} = \frac{\tilde{P}_{i,k-1} + q_i + \delta q_i}{1 + \tilde{\lambda}_i(\tilde{P}_{i,k-1} + q_i + \delta q_i)}, \tag{3.13}$$

where q_i and δq_i are the iith element of $G^{\mathrm{T}}QG$ and $G^{\mathrm{T}}\delta qG$, respectively. Now we define the

variation of $\tilde{P}_{i,k}$ due to δq_i as ΔP_i. From (3.13), ΔP_i is approximated as the following equation.

$$\begin{aligned}\Delta P_i &\approx \left.\frac{\partial \tilde{P}_{i,k}}{\partial \delta q_i}\right|_{\delta q_i=0} \delta q_i \\ &= \frac{1}{\{1+\tilde{\lambda}_i(\tilde{P}_{i,k-1}+q_i)\}^2}\delta q_i. \end{aligned} \tag{3.14}$$

From (3.14), we examine the sensitivity of ΔP_i with respect to $\tilde{\lambda}_i$. Since $H^{\mathrm{T}}\tilde{R}^{-1}H$ is a positive semidefinite matrix, $\tilde{\lambda}_i \geq 0$ and

$$\frac{\partial \Delta P_i}{\partial \tilde{\lambda}_i} < 0, \text{ for } \delta q_i > 0. \tag{3.15}$$

That is, $\Delta P_i(\tilde{\lambda}_i)$ decreases monotonically as $\tilde{\lambda}_i$ goes from zero to infinity. At the limits $\tilde{\lambda}_i \to +0$ and $\tilde{\lambda}_i \to \infty$, the values of $\Delta P_i(\tilde{\lambda}_i)$ are given as

$$\lim_{\tilde{\lambda}_i \to 0} \Delta P_i = \delta q_i, \quad \lim_{\tilde{\lambda}_i \to \infty} \Delta P_i = 0.$$

For good satellite geometry, there is no eigenvalue $\tilde{\lambda}_i$ close to zero. The inflations of $\tilde{P}_{i,k}$ that are caused by the fictitious noise δq_i between time steps $k-1$ and k are suppressed for all i by the observation at time step k, according to (3.14). By choosing an appropriate value of δq_i through trial and error, we can keep the covariance P_k^+ reasonably large to avoid the filter divergence even for the system with model errors. On the other hand, at least one of eigenvalues is zero or close to zero for poor satellite geometry. If we choose the size of δq_i for good satellite geometry, it may be too large for poor satellite geometry and cause unintentionally large inflation of $\tilde{P}_{i,k}$. Too large covariance $\tilde{P}_{i,k}$ leads to widely distributed estimation errors along the corresponding direction and degrades the filter performance.

In the next section, we will propose a new way to choose the fictitious process noise δq_i based on satellite geometry $H_k^{\mathrm{T}}H_k$ to reduce the inflation. To derive the choice, we make an additional assumption:

Assumption 3.3.3. *$\tilde{R}_k = r_k I$, where r_k is a positive scalar.*

From Assumption 3.3.3, $H_k^{\mathrm{T}}\tilde{R}_k^{-1}H_k$ can be rewritten as

$$H_k^{\mathrm{T}}\tilde{R}_k^{-1}H_k = \frac{1}{r_k}G_k\Lambda_k G_k^{\mathrm{T}},$$

where Λ_k is diagonal. From (3.13) and (3.14), we obtain

$$\tilde{P}_{i,k} = \frac{r_k(\tilde{P}_{i,k-1} + q_i + \delta q_i)}{r_k + \lambda_i(\tilde{P}_{i,k-1} + q_i + \delta q_i)}, \tag{3.16}$$

$$\Delta P_i \approx \frac{r_k^2}{(r_k + \lambda_i(\tilde{P}_{i,k-1} + q_i))^2}\delta q_i, \tag{3.17}$$

where λ_i is the iith element of Λ_k. It should be noted that λ_i is an eigenvalue of $H_k^{\mathrm{T}} H_k$ and, unlike $\tilde{\lambda}_i$, represents the satellite geometry independently of $\tilde{R}_k$.

Moreover, we can compute a steady-state solution of (3.12) (or (3.16)), under the assumptions that $\tilde{R}_k$, H_k and $\tilde{Q}_k$ are time-invariant, and $G^{\mathrm{T}} P_0^+ G$ is diagonal. Denoting the steady values of $\tilde{P}_{i,k}$ and $\tilde{P}_{i,k-1}$ as $\tilde{P}_i$ and substituting them into (3.12), we can obtain a steady-state solution:

$$\tilde{P}_i = \frac{-\tilde{q}_i + \sqrt{\tilde{q}_i^2 + \frac{4\tilde{q}_i}{\tilde{\lambda}_i}}}{2}. \tag{3.18}$$

The solution in (3.18) is equivalent to the solution of an algebraic Riccati equation of estimation error covariance [47]. It should be noted that the solution in (3.18) is consistent with the results in Section 3.2.2. The values of $\tilde{P}_i$ that are calculated with $\tilde{\lambda}_i$ and $\tilde{q}_i$ for the motivating example coincide with the standard deviations in Table 3.1. Even though a steady-state solution is well-known, the analysis in this section revealed how the covariance $\tilde{P}_{i,k}$ is inflated at each time step depending on the fictitious noise δq_i and the satellite geometry λ_i (or $\tilde{\lambda}_i$). By using the analytical result in (3.17), we will propose a novel process noise model in the next section to avoid an unintentionally large inflation at each time step.

3.4 Novel Process Noise Model for GNSS Stationary Positioning

3.4.1 Extended Kalman Filter for Stationary Positioning

In this section, we describe the extended Kalman filter for GNSS stationary positioning. Since the pseudo-range and Doppler frequency measurement equations are non-linear, the extended Kalman filter (referred as EKF) is generally used. We define the state vector as $x = [r^{\mathrm{T}}, t_s^{\mathrm{T}}, t, \dot{t}]^{\mathrm{T}}$,

where r[m] is the position vector of a receiver, t[m] is a clock bias, and $\dot{t}$[m/s] is a clock drift. t_s[m] is an inter-system bias (ISB) vector between GPS time and other GNSS's time. We suppose to use a multi-GNSS single frequency receiver, for example, FURUNO GN-8720, and t_s consists of three elements that are GPS-QZSS, GPS-GLONASS, and GPS-Galileo ISBs.

The dynamical system and the measurement equations are given as follows:

$$x_k = F_{k-1}x_{k-1} + w_k, \tag{3.19}$$

$$y_k = h(x_k) + v_k, \tag{3.20}$$

$$h^{(j)}(x_k) = \|r_k - r_k^{(j)}\| + t + t_m, \tag{3.21}$$

$$h^{(j+M)}(x_k) = -\frac{(r_k - r_k^{(j)})^{\mathrm{T}}\dot{r}_k^{(j)}}{\|r_k - r_k^{(j)}\|} + \dot{t}, \tag{3.22}$$

where

$$F_k = \begin{bmatrix} I_{6\times6} & O_{6\times2} \\ O_{2\times6} & \bar{F} \end{bmatrix}, \bar{F} = \begin{bmatrix} 1 & \Delta t \\ 0 & 1 \end{bmatrix}, \tag{3.23}$$

$h^{(j)}(x_k)$ and $h^{(j+M)}(x_k)$ are the jth and the $j+M$th elements of $h(x_k)$, $r_k^{(j)}$ and $\dot{r}_k^{(j)}$ are the position and velocity vectors of the jth satellite, and t_m is the ISB of the GNSS system to which the jth satellite belongs. M is the number of satellites.

The EKF for this system consists of the computations outlined from (3.5) to (3.9), but with (3.7) replaced by

$$\hat{x}_k^+ = \hat{x}_k^- + K_k[y_k - h(\hat{x}_k^-)], \tag{3.24}$$

and H_k computed as

$$H_k = \left.\frac{\partial h(x_k)}{\partial x_k}\right|_{x_k=\hat{x}_k^-}.$$

The EKF may often produce a biased estimate and diverge due to unmodeled measurement errors, dynamics errors, and non-linear effects of (3.21) [48]. To cover the uncertainties by a

fictitious process noise, we usually choose the process noise covariance in the EKF as

$$\tilde{Q} = Q + \delta\bar{q}. \tag{3.25}$$

For the EKF in this work, we set Q to $0.01I$ to avoid the numerical problems as in Section 3.2.2. This $\tilde{Q}$ makes gain matrix K_k large from (3.6) and (3.9), thus the EKF updates the estimate $\hat{x}$ by overweighting current observations. It should be noted that a larger R cannot be effective in preventing filter divergence, since a larger $\tilde{R}$ makes K_k smaller. We choose $\tilde{R}$ so that it represents actual measurement noise level. In this work, $\tilde{R}$ is determined based on the Signal-Noise-Ratios (SNRs) of the receiver FURUNO GN-8720 as follows [29, 30]:

$$\begin{aligned} \tilde{R} &= \mathrm{diag}(\sigma_1^2(s_1), \ldots, \sigma_M^2(s_M), \mu_1^2(s_1), \ldots, \mu_M^2(s_M)), \\ \sigma_k &= 0.64 + 784e^{-0.142 s_k}, \\ \mu_k &= 0.0125 + 6767e^{-0.267 s_k}, \quad k = 1, \ldots, M, \end{aligned} \tag{3.26}$$

where s_k, σ_k and μ_k are the SNR, the standard deviations of pseudo-range noise and Doppler frequency noise for the kth satellite signal.

3.4.2 Process Noise Covariance Based on Satellite Geometry

In practical applications of EKF, it is not easy to find an appropriate choice of the fictitious noise $\delta\bar{q}$ in (3.25). It is often chosen and fixed through a trial and error process, so that a required performance of EKF is obtained. If the satellite geometry is always good and all the eigenvalues λ_i are equally large, such a choice of $\delta\bar{q}$ could work well. In this work, we call it the conventional choice, and consider only $\delta\bar{q}$ in the following form:

$$\delta\bar{q} = \delta q I, \tag{3.27}$$

where δq is a positive scalar. However, if the satellite geometry is poor, the conventional choice of $\delta\bar{q}$ would cause an unintentional inflation of P as described in Sections 3.2 and 3.3.

In this section, we propose a novel way to choose the fictitious noise $\delta\bar{q}$ based on satellite geometry by assuming that (3.16) approximately holds in our EKF. The basic idea is to choose

$\delta\bar{q}$ so that ΔP_i in (3.17) is less than or equal to a specified value c_i at each time step k in order to suppress the unintentional inflation. The fictitious noise is chosen as follows.

$$\begin{aligned} \delta\bar{q} &= G_k Q G_k^{\mathrm{T}}, \\ Q_i &= \begin{cases} \delta q_i' & \text{if } \delta q_i' \leq \delta q \\ \delta q & \text{else} \end{cases}, \\ \delta q_i' &= \frac{(r_k + \lambda_i(\tilde{P}_{i,k-1} + q_i))^2}{r_k^2} c_i, \end{aligned} \tag{3.28}$$

where the matrix Q is diagonal, and Q_i is the ith diagonal element of Q, and δq is a positive scalar for the conventional choice. From (3.17) and (3.28), if $\delta q_i' \leq \delta q$, ΔP_i satisfies $\Delta P_i \approx c_i$ even for a small λ_i. If $\delta q_i' > \delta q$, $\Delta P_i < c_i$ holds approximately even for $\delta q_i = \delta q$. Consequently, we can expect that the unintentional inflation of P is suppressed, because ΔP_i is limited to the maximum value of c_i, regardless of satellite geometry λ_i. For the proposed choice of $\delta\bar{q}$, we can keep an appropriate inflation of P by the parameters c_i. We will determine c_i through simulation study in Section 3.5.

Moreover, the steady-state solution $\tilde{P}_i$ in (3.18) does not hold for $\delta\bar{q}$ in (3.28), because $\tilde{q}_i$ in (3.12) includes $\tilde{P}_{i,k-1}$. By substituting (3.28) into (3.16), we can obtain the following equation:

$$\tilde{\lambda}_i^3 c_i \tilde{P}_i^3 + (\tilde{\lambda}_i + \tilde{\lambda}_i^2 c_i + 2\tilde{\lambda}_i^3 c_i q_i)\tilde{P}_i^2 + (\tilde{\lambda}_i q_i - \tilde{\lambda}_i c_i + \tilde{\lambda}_i^3 c_i q_i^2)\tilde{P}_i - (c_i + q_i + 2\tilde{\lambda}_i c_i q_i + \tilde{\lambda}_i^2 c_i q_i^2) = 0. \tag{3.29}$$

By solving the above equation numerically, we can obtain an approximate steady-state solution $\tilde{P}_i$.

Strictly speaking, (3.16) does not hold for the EKF in this section, because the three assumptions in Section 3.3 may be unsatisfied, that is to say, (1) $F_k \neq I$, (2) $G_k^{\mathrm{T}} P_{k-1}^- G_k$ is not diagonal, and (3) $\tilde{R}_k \neq r_k I$. For Assumption 3.3.3 we choose $\tilde{R}_k$ as diagonal and give its diagonal elements based on SNRs in this work. Since SNRs of LOS signals usually have similar values, we can expect that $\tilde{R}_k \approx r_k I$ and Assumption 3.3.3 is approximately satisfied. For Assumptions 3.3.1 and 3.3.2, we cannot justify them theoretically. Although Assumption 3.3.1 is necessary to show that both P_k^+ and P_{k-1}^+ are diagonalized by G_k, they are almost diagonalized for the experimental results shown in Section 3.6. Therefore, Assumption 3.3.2 is approximately satisfied

in the experimental results, and then we do not need Assumption 3.3.1 to show it. However, for $F \neq I$, (3.11) itself does not hold. In this work, we suppose that the effects of F with $\bar{F}$ in (3.23) are small, because only one nondiagonal element is nonzero. We also note that, in Assumption 3.3.2, $\tilde{Q}$ can be chosen with $\delta\bar{q}$ in (3.28) such that $G_k^{\mathrm{T}}\tilde{Q}G_k$ is diagonal. As a result, we believe that (3.16) approximately holds in our EKF.

We finally summarize the proposed noise model. Employing the fictitious noise $\delta\bar{q}$ in (3.28), $\tilde{Q}$ varies depending on satellite geometry, and $\Delta\tilde{P}_i$ can be insensitive to satellite geometry. We, therefore, call the model *satellite-geometry adaptive model*. Although a noise-adaptive model introduced in Section 3.1 is well known, $\tilde{Q}$ is estimated based on recent observations, and an accurate estimation would be difficult for poor satellite geometry. To our best knowledge, our model is the first process noise model that changes with $H^{\mathrm{T}}H$, i.e., satellite geometry.

3.5 Simulation Study

We present here some simulation results of the proposed process noise model to demonstrate its effectiveness and to determine an appropriate value of c_i. The model is applied to the Kalman filter for the simplified system in Section 3.2.2, where all the assumptions in Section 3.3 are satisfied and (3.16) holds.

We consider the following three settings of the process noise $\tilde{Q}$.

Setting (1) No fictitious process noise:

$$\tilde{Q} = Q \tag{3.30}$$

Setting (2) Conventional choice of fictitious process noise:

$$\tilde{Q} = Q + \delta q I \tag{3.31}$$

Setting (3) Proposed choice of fictitious process noise:

$$\tilde{Q} = Q + G_k Q G_k^{\mathrm{T}} \tag{3.32}$$

The first and second settings are the same as the settings in Fig. 3.4a and 3.4b, where δq is

chosen as $\delta q = 1$ in (3.31). In this work, we assume that, for (3.32), all the c_i are the same, that is, $c_i = c$ for $\forall i$. Numerical simulations for setting (3) were performed with different values of c: (3-a) with $c = 1.0$ to (3-f) with $c = 0.01$ as shown in Table 3.3. The standard deviations σ_{SE}, σ_{NE}, and their ratios for all the settings are summarized in Table 3.3, where the results for settings (1) and (2) in Table 3.1 are shown again. The Root Mean Squared Error (RMSE) d is also computed for the three-dimensional position to show the positioning accuracy in the table.

For determining an appropriate value of c, we should pay attention to two points: avoiding the filter divergence and suppressing the unintentional inflation of P along the eigenvectors corresponding to small eigenvalues λ_i. For the first point, σ_{NE}, that is the standard deviation along the direction with a large eigenvalue, is increased to 0.80 in setting (2), comparing with setting (1). A similar magnitude of σ_{NE} would be necessary even in setting (3) for the divergence avoidance. For the second point, we check the ratio of σ_{SE} to σ_{NE}. In setting (1), the ratio comes only from the satellite geometry, because there is no model error or fictitious noise. Therefore, we suppose that the ratio in setting (1) is desirable even in setting (3) for suppressing the inflation. From these two points, we can choose setting (3-c) $c = 0.36$ for the proposed noise covariance model in this work. Moreover, it should be noted that the values of standard deviations in (3-a) to (3-f) are consistent with the steady-state solutions computed from (3.29).

Table 3.3: Standard deviations, their ratios, and RMSEs with different process noise settings.

Settings	**(1)**	**(2)**	**(3-a)**	**(3-b)**	**(3-c)**	**(3-d)**	**(3-e)**	**(3-f)**
σ_{SE}[m]	1.08	3.38	3.52	3.14	2.71	2.22	1.63	1.29
σ_{NE}[m]	0.31	0.80	0.92	0.87	0.80	0.68	0.49	0.38
σ_{SE}/σ_{NE}	3.48	4.22	3.82	3.61	3.39	3.26	3.32	3.39
d	1.21	3.65	3.83	3.45	3.01	2.49	1.84	1.46

The settings from (3-a) to (3-f) are with $c = \{1.0, 0.64, 0.36, 0.16, 0.04, 0.01\}$.

The effectiveness of the proposed noise model is verified by comparing the simulation results in settings (2) and (3-c). The estimated positions in a r_e-r_n plane for the two settings are plotted in Figure 3.4a,b, where the filter computation was repeated 1000 times for each setting as in Section 3.2.2 and Fig. 3.4a is the same as Fig. 3.3b. Ellipsoids in these figures are the 1σ contours of probability density function (Gaussian) that are calculated from (3.18) for Fig. 3.4a and from (3.29) for Fig. 3.4b. The distribution of horizontal position errors obtained by numerical simulations coincides with the ellipsoid obtained theoretically for each setting.

We can see that the estimation errors in setting (3-c) are reduced in the direction of southeast, that is, the direction of the minimum eigenvalue of $H^{\mathrm{T}}H$. In this numerical results, the proposed noise model suppresses the unintentional inflation of σ_{SE} by about 20%. It should be noted that these results show that both precision and accuracy of positioning in the horizontal plane are improved in setting (3-c), because the mean value of estimation errors is almost zero. We can also check the positioning accuracy that includes the vertical errors, by comparing the RMSEs for settings (2) and (3-c) in Table 3.3.

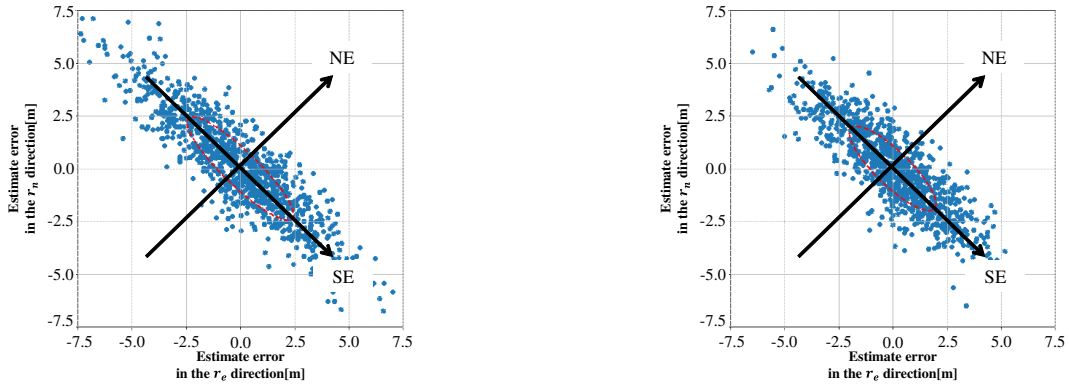

(a) Filter results with setting (2)

(b) Filter results with setting (3-c)

Figure 3.4: Estimated positions obtained for settings (2) and (3-c).

3.6 Experimental Results of Stationary Positioning

This section presents experimental results to show the effectiveness of the proposed process noise model by applying it to actual data obtained in an urban canyon. The data was collected at the time and location shown in Table 3.4, and Fig. 3.5 is a fisheye-camera image with a satellite sky plot at the beginning of data collection. We used a multi-GNSS single frequency receiver, FURUNO GN-8720, that can receive the signals of GPS, QZSS L1C/A, GLONASS L1OF, and Galileo E1, and acquired about ten minutes the data that includes pseudo-ranges, Doppler frequencies, navigation messages, and so on. The receiver was fixed at the location that corresponds to the center of Fig. 3.5 during the experiment, and the pseudo-ranges and Doppler frequencies were used as the measurements for EKF. In the figure, blue dots are LOS satellites, and red dots are NLOS satellites, as in Section 3.2.1. By detecting NLOS satellites

from the fisheye-camera images, the signals from them were excluded from the measurements. The LOS satellites are quite close to each other, and the satellite geometry can be considered as poor, because the minimum eigenvalue of the LOS satellite geometry is always about 0.01 in the data[3].

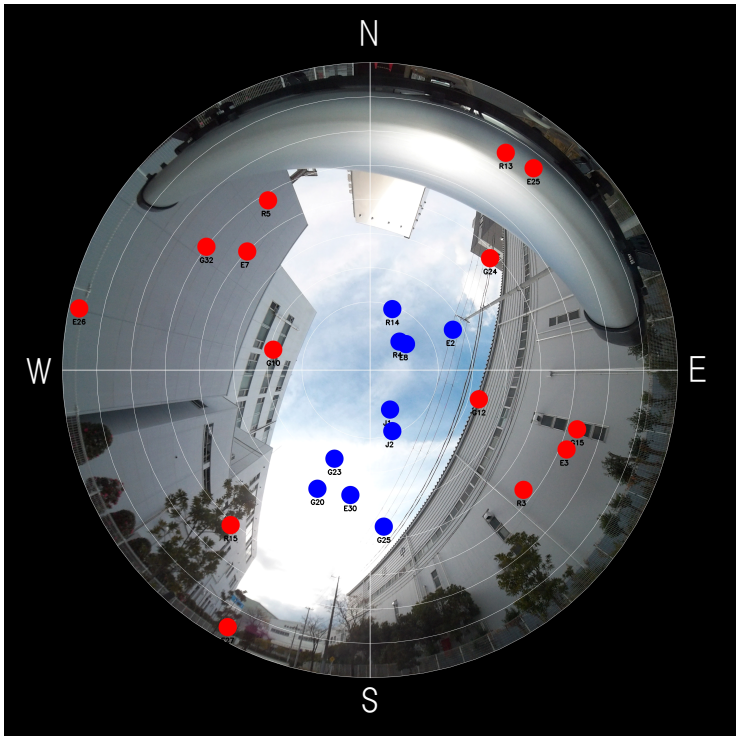

Figure 3.5: A fisheye-camera image taken at the place where we gathered data.

Based on the numerical results shown in Section 3.5, we examine positioning performance of the EKF in Section 3.4.1 with two parameter settings for process noise covariance: Setting (2) with $\delta q = 1$ and Setting (3-c) with $c = 0.36$. The EKFs with the conventional and the proposed noise settings were implemented in a laptop computer as post-processing programs, by customizing the EKF program implemented in FURUNO GN-8720. The EKFs compute the estimated position of the receiver by using only the measurements from LOS satellites.

In order to obtain an ensemble average of estimation errors, we make N measurement data sets whose length is l, from the data acquired for about ten minutes, by shifting the start point by one step. The EKF calculation is performed for each of the N data sets, $Y_1 = \{y_1, y_2, \cdots, y_l\}, Y_2 =$

[3]Although multipath signals may occur via diffraction/reflection even for LOS satellites, they would be largely attenuated compared to LOS direct signals. In this work, we do not consider the effects of multipath signals by assuming that they are sufficiently small

$\{y_2, y_3, \cdots, y_{l+1}\}, \cdots, Y_N = \{y_N, y_{N+1}, \cdots, y_{l+N-1}\}$, with the initial conditions shown in Table 3.4. The length l of each data set is chosen such that the changes in $\hat{x}$ and P become sufficiently small in the EKF as the time step k approaches l. We focus on the estimation error in position at the final step, $\hat{r}(l|l) - r$, where the true position r is known as in Table 3.4, and denote it as $\tilde{r}_m$ for mth data set.

Table 3.4: Algorithm and experimental settings.

Configurations and Parameters		**Remarks**
True location	34.713817 N	Latitude[degree]
	135.335599 E	Longitude[degree]
	40.49	Ellipsoidal height[m]
Date of experiment	18/12/2020 04:15:37–04:26:20	UTC
Antenna	Taoglass AA171.301111	
δq	1	(3.31)
c	0.36	(3.28) and (3.32)
$\hat{x}(0\|0)$	$\hat{x}_0 \sim N(x_{true}(0), 100I)$	$x_{true}(0)$ is the true state of x_0
P_0^+	$100I$	Initial value of P
l	120	Length of each data set
N	534	Number of data sets

We can compute estimation error covariance Σ and RMSE (Root Mean Squared Error) d as follows:

$$\Sigma = \frac{1}{N-1} \sum_{m=1}^{N} (\tilde{r}_m - \bar{r})(\tilde{r}_m - \bar{r})^{\mathrm{T}}, \tag{3.33}$$

$$\bar{r} = \frac{1}{N} \sum_{m=1}^{N} \tilde{r}_m,$$

$$d = \sqrt{\frac{1}{N} \sum_{m=1}^{N} \tilde{r}_m^{\mathrm{T}} \tilde{r}_m}. \tag{3.34}$$

The minimum and maximum standard deviations σ_{min} and σ_{max} of the estimation errors $\tilde{r}_m$ are obtained by calculating the minimum and maximum eigenvalues of Σ. Table 3.5 summarizes the values of σ_{min}, σ_{max}, $\sigma_{max}/\sigma_{min}$ and d for the two settings. The following two points can be seen in Table 3.5:(a) σ_{max} and $\sigma_{max}/\sigma_{min}$ in setting (3-c) are less than the ones in setting (2), while the values of σ_{min} in both settings are almost the same, and (b) RMSE d in setting (3-c) is also less than the one in setting (2). The first point (a) would indicate that the proposed noise

model can suppress the unintentional inflation of estimation error covariance even for actual data in an urban canyon. From the second point (b), the positioning accuracy with the proposed noise model is also improved compared to the conventional noise model. The estimation errors $\tilde{r}_m$ for the two settings are shown in Figure 3.6a,b, where the errors $\tilde{r}_m$ are projected to the plane spanned by the unit eigenvectors e_{min} and e_{max} that correspond to σ_{min} and σ_{max}, respectively. The ellipsoid in each figure is the 1σ contour of probability density function that is supposed to be Gaussian with the standard deviations σ_{min} and σ_{max} in Table 3.5.

Table 3.5: Standard deviations from estimation error covariance Σ, their ratios, and RMSEs.

Settings	**(2)**	**(3-c)**
σ_{max}[m]	4.50	4.11
σ_{min}[m]	0.31	0.30
$\sigma_{max}/\sigma_{min}$	14.33	13.57
d	4.90	4.44

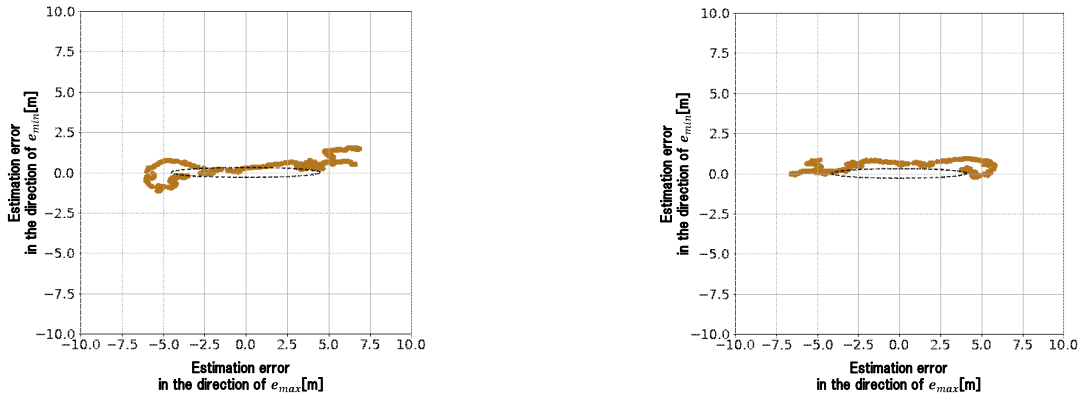

(a) Filter results with setting (2)

(b) Filter results with setting (3-c)

Figure 3.6: Estimated position errors in the plane spanned by e_{min} and e_{max}.

Although the results in this section demonstrate that the suppression of covariance inflation is achieved by the proposed noise model, it should be noted that the eigenvector corresponding to σ_{max} is almost along the altitude direction. The standard deviations σ_{min} and σ_{max} in Table 3.5 are also quite different from the ones calculated from (3.18) and (3.29). These differences from the simulation results in Section 3.5 may be due to the following two reasons. First, the satellite geometry in Fig. 3.5 is largely different from the one for the simulation results, because there is no LOS satellite with a low elevation angle in Fig. 3.5. The uncertainty

in the altitude direction would be large due to the clock bias t_b for such a satellite geometry[4]. Secondly, Assumption 1 is not satisfied in the EKF in Section 3.4.1. Equations (3.18) and (3.29) do not hold without the assumption. The non-diagonal component of $\bar{F}$ in (3.23) would be non-negligible, especially because the position estimation in the altitude direction is highly dependent on the clock bias t_b.

The above inconsistency between the simulation results and the experimental results could be resolved by extending the proposed process noise model to the systems without the assumptions in Section 3.3. As shown in the next chapter, theoretical extension of the sensitivity analysis is possible, and it will allow us to develop a process noise model in a more consistent manner for the systems without the assumptions. Further improvement of the estimation performance may also be possible by changing the choice of c or $\delta\bar{q}$ itself. The extension and improvement will be developed in the next chapter.

3.7 Conclusion

This chapter pointed out that a fictitious process noise to prevent the filter divergence can degrade the filter performance for a poor satellite geometry due to an unintentional inflation of estimation error covariance. A sensitivity analysis of estimation error covariance by fictitious process noise and satellite geometry was performed under some assumptions, and we proposed a novel model of the fictitious process noise based on satellite geometry in order to suppress the unintentional inflation of estimation error covariance. The effectiveness of the proposed noise model was shown via simulation and experimental results. Although the sensitivity analysis and the proposed model derived from it are based on the assumptions, the approach in this chapter can be extended to the systems without the assumptions. The extension and further improvement of the proposed approach will be presented in the next chapter.

[4]If the elevation angles of all the satellites are close to 90 degrees, the errors in altitude estimation and clock bias estimation would be indistinguishable. Through numerical simulations based on the simplified simulation model introduced in Section 3.2.2 for the same satellite geometry as in Fig. 3.5, we can see that the uncertainty in the altitude direction with clock bias estimation is much larger than the one without it

Chapter 4

Adaptive Choice of Process Noise Covariance Using Measurement Matrices

4.1 Introduction

Improving the accuracy of GNSS positioning in urban canyons is a challenging topic, especially for low-cost GNSS receivers. Although Non-Line-Of-Sight (NLOS) signals can be rejected by various methods, the number of satellites available in position calculation decreases, and their geometric distribution is biased. In Kalman filter for GNSS positioning, the process noise covariance is often bumped up to avoid the filter divergence in the presence of unknown model errors, by assuming that there is a fictitious process noise in addition to the nominal process noise.

For systems with inaccurate models, many approaches have been proposed so far to mitigate the increase in estimation errors or to avoid the filter divergence by choosing appropriately the covariances of process noise and measurement noise in the filters. A common heuristic approach is to add fictitious noises to the nominal covariances of the original system model. Because of the fictitious noises for process noise and measurement noise, the covariance of state estimation error in the filter becomes sufficiently large to cover the model error, and the filter divergence is avoided. Although the fictitious noises are often given by trial and error, naively chosen fictitious noises tend to unintentionally inflate the state estimation error covariance and result in degraded estimation accuracy, especially for the systems where the number of measurements is less than the number of state variables, as we pointed out in [49, 50]. Fad-

ing Memory Filter (FMF) can be viewed as one of fictitious noise approaches. By weighting the estimation errors according to their time steps, FMF takes more account of the recent estimation error, which is equivalent that the process noise covariance is increased by a certain fictitious noise. Even when FMF is employed, the degradation of estimation accuracy with the unintentional inflation of estimation error covariance has been reported in [24, 42, 51, 52].

Another common approach is to adaptively modify the process noise and measurement noise covariances using actual measurements [43, 53]. The appropriate values of the covariances are estimated based on the measurements obtained in multiple steps under the assumption that noise statistics are ergodic. However, when the noise statistics vary with time steps, it is difficult to choose how many measurement steps should be used for estimation. In addition, it has been known that the estimation of the process noise covariance matrix cannot be determined uniquely when the number of measurements is less than the number of state variables [22, 23].

Chapter 3 pointed out that fictitious noise can make the estimation error covariance excessively large with poor satellite geometry, and the unintended inflation may degrade filter performance in urban canyons. We proposed a process noise model based on satellite geometry to suppress the unintended inflation. However, the results of Chapter 3 have three problems to be resolved. (1) The sensitivity analysis for the estimation error covariance due to fictitious noise is limited to a linear system whose state transition matrix is an identity matrix. (2) Although the proposed model in Chapter 3 requires a threshold to switch fictitious noise to the smaller one, it is difficult to choose an appropriate threshold for various satellite distributions. (3) We verified performance improvement with the proposed model through numerical simulations and experiments. However, they have been performed under the conditions that the number of satellites is always the same and their geometry is the same or almost the same.

This chapter presents an extended process noise model based on measurement matrices. The outcomes in this chapter overcome the three problems mentioned above. We show the sensitivity of the estimation error covariance due to fictitious noise without assumptions defined in Chapter 3. The extended process noise model based on the sensitivity analysis is developed to improve the model presented in Chapter 3. The improved model give fictitious noise adaptively based on the measurement matrix at each time step. This indicates that fictitious noise due to this model varies depending on satellite geometry. We perform experiments, and the results show (1) the same effect as in the previous model derived in Chapter 3 and (2) the improve-

ment under the conditions that the number of satellites and their geometry varies on time. The former is to suppress the unintentional inflation of the estimation error covariance matrix, and the latter shows that the extended model improve the EKF performance with various satellite distributions.

The contribution of this work is twofold: First, to the best of our knowledge, the proposed model is the first to choose the process noise covariance adaptively to the measurement matrix to overcome the accuracy degradation caused by inaccurate model. Second, it is shown that the proposed model works well for GNSS stationary positioning and GNSS/INS positioning with various satellite distributions.

The rest of this chapter begins with an overview of the extended Kalman filter. We develop sensitivity equations of the estimation error and its covariance matrix due to fictitious noise for a linearized system. We propose the extended process noise model based on the sensitivity analysis by extending the previous one presented in Chapter 3. In this model, we design two types of the choice of fictitious noise. The difference between the two types is how to determine fictitious noise level. The first is to choose it with a fixed parameter, and the second is to minimize the sum of squared residuals. We last present the results of experiments with each model derived in this chapter. Further, we demonstrate numerical simulations of robot localization to show that the proposed models can be employed in applications other than GNSS.

4.2 Sensitivity Analysis for Discrete Nonlinear Systems

4.2.1 Extended Kalman Filter for Discrete Nonlinear Systems

We consider a discrete nonlinear system:

$$x_k = f(x_{k-1}) + w_k, \tag{4.1}$$

$$y_k = h(x_k) + v_k, \tag{4.2}$$

where the state vector and the measurement vector at time step k are denoted as $x_k \in \mathbb{R}^n$ and $y_k \in \mathbb{R}^m$ respectively. The process noise and measurement noise are represented by $w_k \in \mathbb{R}^n$ and $v_k \in \mathbb{R}^m$, and the sequences $\{w_k\}$ and $\{v_k\}$ are assumed to be white, zero-mean and uncorrelated with one another. The covariance matrices for w_k and v_k are expressed by Q_k and R_k, respectively.

Assuming that the functions f and h are differentiable as necessary, the system in (4.1) and (4.2) can be linearized around a prior estimate $\hat{x}_k^-$ as follows:

$$x_k = F_{k-1}x_{k-1} + u_{k-1} + w_k, \tag{4.3}$$

$$\eta_k = H_k x_k + v_k, \tag{4.4}$$

where

$$F_k = \left.\frac{\partial f(x_k)}{\partial x_k}\right|_{x_k=\hat{x}_k^+}, \; H_k = \left.\frac{\partial h(x_k)}{\partial x_k}\right|_{x_k=\hat{x}_k^-}, \tag{4.5}$$

$$u_k = f(\hat{x}_k^+) - F_k\hat{x}_k^+, \; \eta_k = y_k - h(\hat{x}_k^-) + H_k\hat{x}_k^-. \tag{4.6}$$

The extended Kalman filter (EKF) for the system in (4.3) and (4.4) can be written as follows:

$$\hat{x}_k^- = f(\hat{x}_{k-1}^+), \tag{4.7}$$

$$P_k^- = F_{k-1}P_{k-1}^+F_{k-1}^{\mathrm{T}} + Q_k, \tag{4.8}$$

$$\hat{x}_k^+ = \hat{x}_k^- + K_k[y_k - h(\hat{x}_k^-)], \tag{4.9}$$

$$P_k^+ = (I - K_kH_k)P_k^- \tag{4.10}$$

$$= (I - K_kH_k)P_k^-(I - K_kH_k)^{\mathrm{T}} + K_kR_kK_k^{\mathrm{T}} \tag{4.11}$$

$$= [(P_k^-)^{-1} + H_k^{\mathrm{T}}R_k^{-1}H_k]^{-1}, \tag{4.12}$$

$$K_k = P_k^-H_k^{\mathrm{T}}(H_kP_k^-H_k^{\mathrm{T}} + R_k)^{-1}, \tag{4.13}$$

$$= P_k^+H_k^{\mathrm{T}}R_k^{-1}, \tag{4.14}$$

where $\hat{x}_k$ and P_k denote respectively the state estimate and the estimation-error covariance matrix, and K_k is Kalman gain. The superscripts $-$ and $+$ for $\hat{x}_k$ and P_k mean 'prior' and 'posterior'. In (4.10)-(4.14), P_k^+ and K_k are represented in several ways for later use.

We also define estimation errors in $\hat{x}_k^-$ and $\hat{x}_k^+$ for convenience of later use as follows:

$$e_k^- \equiv x_k - \hat{x}_k^-, \tag{4.15}$$

$$e_k^+ \equiv x_k - \hat{x}_k^+. \tag{4.16}$$

From (4.9), by ignoring higher order terms, e_k^+ and e_k^- satisfy the following linearized equation:

$$e_k^+ = \Psi_k e_k^- - K_k v_k, \tag{4.17}$$

where a filter transition matrix Ψ_k is defined as

$$\Psi_k = I - K_k H_k. \tag{4.18}$$

In general, EKF works well if the functions f and h and the matrices F_k, G_k, H_k, Q_k, and R_k accurately approximate the actual system. However, it often suffers from model errors, and inaccurate models tend to result in large or biased estimation errors; in particular, process model uncertainties may cause filter divergence [6, 39].

One approach to coping with the model errors is to add fictitious noises to w_k and v_k and inflate Q_k and R_k appropriately. The inflated Q_k and R_k may cover uncertainties due to model errors and mitigate unexpected large or biased estimation errors. However, it would be difficult to find appropriate fictitious noises, especially for the systems where the number and quality of measurements vary with the environment. If fictitious noises are chosen in a naïve manner, the filter performance can be even worse, as shown in Sections 3.5 and 3.6 in Chapter 3.

In this paper, we consider adding fictitious noise to the process model in (4.3) based on the measuremetn matrix H_k. In the following subsection, when the process noise covariance is bumped up as $Q_k + \delta Q_k$ by fictitious noises, we will analyze the variations of P_k^+ and K_k due to δQ_k.

4.2.2 Sensitivity of Estimation Error Covariance Due to Fictitious Noise

In this subsection, we assume that filter computations at time step $k-1$ are completed and P_{k-1}^+ is given, and that a fictitious noise is added to w_k at time step k. Then, in the EKF expressed in (4.7) through (4.14), (4.8) is replaced by the following equation:

$$P_k^-(\delta Q_k) = F_{k-1} P_{k-1}^+ F_{k-1}^{\mathrm{T}} + Q_k + \delta Q_k, \tag{4.19}$$

where δQ_k is a positive semi-definite matrix in $\mathbb{R}^{n\times n}$ that corresponds to the fictitious noise.

The variations of P_k^+ and K_k due to δQ_k are defined as

$$\Delta K_k \equiv K_k(\delta Q_k) - K_k(0), \tag{4.20}$$

$$\Delta P_k \equiv P_k^+(\delta Q_k) - P_k^+(0). \tag{4.21}$$

Note that P_k^-, P_k^+ and K_k are expressed as the functions of δQ_k, that is, $P_k^-(\delta Q_k)$, $P_k^+(\delta Q_k)$ and $K_k(\delta Q_k)$, in (4.19), (4.20) and (4.21). When δQ_k is a zero matrix, they are denoted as $P_k^-(0)$, $P_k^+(0)$ and $K_k(0)$ that coincide with those in the EKF without fictitious noise.

For a given δQ_k, ΔK_k and ΔP_k can be calculated from the following lemma.

Lemma 4.2.1. *ΔK_k and ΔP_k satisfy the following equations:*

$$\Delta K_k = \Delta P_k H_k^{\mathrm{T}} R_k^{-1}, \tag{4.22}$$

$$\Delta P_k = [I - K_k(0)H_k]\delta Q_k\{[I - K_k(0)H_k]^{-\mathrm{T}} + H_k^{\mathrm{T}} R_k^{-1} H_k \delta Q_k\}^{-1}. \tag{4.23}$$

Proof. From (4.14) and (4.21),

$$\begin{aligned} K_k(\delta Q_k) &= P_k^+(\delta Q_k) H_k^{\mathrm{T}} R_k^{-1} \\ &= [P_k^+(0) + \Delta P_k] H_k^{\mathrm{T}} R_k^{-1}. \end{aligned}$$

Substituting the above equation into (4.20), we have (4.22). From (4.10),

$$\begin{aligned} P_k^+(\delta Q_k) &= [I - K_k(\delta Q_k)H_k]P_k^-(\delta Q_k) \\ &= [I - (K_k(0) + \Delta K_k)H_k](P_k^-(0) + \delta Q_k). \end{aligned}$$

Substituting (4.22) into the above equation and noting that $[I - K_k(0)H_k]^{-\mathrm{T}} = I + H_k^{\mathrm{T}} R_k^{-1} H_k P_k^-(0)$ from (4.10) and (4.12), we obtain (4.23). □

On the other hand, if ΔP_k is given, the corresponding value of δQ_k can be obtained from the following lemma.

Lemma 4.2.2. *Under the assumption that $P_k^-(\delta Q_k)$ is positive definite, δQ_k corresponding to a*

given ΔP_k is obtained as

$$\delta Q_k = [I - (K_k(0) + \Delta K_k)H_k]^{-1}[\Delta P_k - \Delta K_k(H_k P_k^-(0)H_k^{\mathrm{T}} + R_k)\Delta K_k^{\mathrm{T}}][I - (K_k(0) + \Delta K_k)H_k]^{-T}, \tag{4.24}$$

where ΔK_k is calculated from (4.22)*.*

Proof. From (4.11), ΔP_k in (4.21) can be written as

$$\begin{aligned}\Delta P_k &= [I - (K_k(0) + \Delta K_k)H_k][P_k^-(0) + \delta Q_k][I - (K_k(0) + \Delta K_k)H_k]^{\mathrm{T}} \\ &\quad + (K_k(0) + \Delta K_k)R_k(K_k(0) + \Delta K_k)^{\mathrm{T}} - [I - K_k(0)H_k]P_k^-(0)[I - K_k(0)H_k]^{\mathrm{T}} - K_k(0)R_k K_k^{\mathrm{T}}(0) \\ &= [I - (K_k(0) + \Delta K_k)H_k]\delta Q_k[I - (K_k(0) + \Delta K_k)H_k]^{\mathrm{T}} + \Delta K_k[H_k P_k^-(0)H_k^{\mathrm{T}} + R_k]\Delta K_k^{\mathrm{T}}, \end{aligned} \tag{4.25}$$

where we used the following equation:

$$\begin{aligned}\Delta K_k R_k K_k^{\mathrm{T}}(0) &= \Delta K_k R_k R_k^{-1} H_k P_k^+(0) \\ &= \Delta K_k H_k P_k^+(0) \\ &= \Delta K_k H_k P_k^-(0)(I - K_k(0)H_k)^{\mathrm{T}}.\end{aligned}$$

By solving (4.25) for δQ_k, we have (4.24). Note that $[I - (K_k(0) + \Delta K_k)H_k]^{-1}$ always exists because

$$\begin{aligned}[I - (K_k(0) + \Delta K_k)H_k]^{-1} &= [I - P_k^+(\delta Q_k)H_k^{\mathrm{T}}R_k^{-1}H_k]^{-1} \\ &= [(P_k^+(\delta Q_k))^{-1} - H_k^{\mathrm{T}}R_k^{-1}H_k]^{-1}(P_k^+(\delta Q_k))^{-1} \\ &= P_k^-(\delta Q_k)(P_k^+(\delta Q_k))^{-1} \\ &= I + P_k^-(\delta Q_k)H_k^{\mathrm{T}}R_k^{-1}H_k,\end{aligned}$$

where, from (4.12) and $P_k^-(\delta Q_k) > 0$, we used

$$(P_k^+(\delta Q_k))^{-1} = (P_k^-(\delta Q_k))^{-1} + H_k^{\mathrm{T}}R_k^{-1}H_k.$$

□

It should be noted that, while the filter is working properly, we can expect that $P_k^-(0) > 0$ and the assumption that $P_k^-(\delta Q_k) > 0$ would hold. If $P_k^-(0) > 0$, $P_k^-(\delta Q_k)$ is positive definite from (4.19) for $\delta Q_k \geq 0$. In addition, ΔP_k is a positive semi-definite matrix from (4.25) for $\delta Q_k \geq 0$.

4.3 Process Noise Model with a Fixed Parameter

This section derives a process noise model with a fixed parameter α_k based on the sensitivity analysis in Sec. 4.2. Since Lemma 4.2.2 gives δQ_k corresponding to ΔP_k, we can choose ΔP_k as the decision variable instead of δQ_k. Moreover, as will be discussed in Sec. 3.2.2, we assume that ΔP_k is in the form of

$$\Delta P_k = \alpha_k H_k^{\mathrm{T}} R_k^{-1} H_k. \tag{4.26}$$

From Lemma 4.2.2, δQ_k corresponding to the above ΔP_k is

$$\delta Q_k \approx \alpha_k [I - K_k(0) H_k]^{-1} \Delta P_k [I - K_k(0) H_k]^{-T}, \tag{4.27}$$

where we suppose that α_k is small.

An intuitive explanation of the effect of $\Delta P_k = \alpha_k H_k^{\mathrm{T}} R_k^{-1} H_k$ in (4.26) is as follows: $\Delta P_k = \alpha_k H_k^{\mathrm{T}} R_k^{-1} H_k$ means that the inflation is restricted in the direction of $H_k^{\mathrm{T}} R_k^{-1} H_k$. From (4.12), Kalman filter can reduce the estimation-error covariance P_k only along the direction of $H_k^{\mathrm{T}} R_k^{-1} H_k$ through each measurement update. If δQ_k inflates P_k along other directions, the inflation at each time step is accumulated without suppression at the measurement update, and would result in unintentionally large P_k in the directions. The choice of δQ_k in (4.27) can avoid the accumulation by eliminating the inflation along the directions other than $H_k^{\mathrm{T}} R_k^{-1} H_k$.

4.4 Process Noise Model Based on Measurement Residuals

4.4.1 Minimization of Measurement Residuals

In Kalman Filter, the Kalman gain K_k is derived so that the trace of the covariance matrix for e_k^+, that is, $E\{\|e_k^+\|^2\}$ is minimized [6], where $E\{a\}$ means the expectation of a randam variable

a. In this paper, utilizing the parameter δQ_k, we minimize the expectation of measurement residual to build a filter that gives more credence to the recent measurement without using the measurement itself. The measurement residual m_k is represented as a function of δQ_k by the following equation:

$$\begin{aligned} m_k(\delta Q_k) &\equiv y_k - h(\hat{x}_k^+(\delta Q_k)) \approx H_k(x_k - \hat{x}_k^+(\delta Q_k)) + v_k \\ &= H_k e_k^+(\delta Q_k) + v_k. \end{aligned} \tag{4.28}$$

There are two reasons to focus on the measurement residual $m_k(\delta Q_k)$; First, many adaptive filtering approaches utilize the measurements to modify Q_k and R_k, because we can see the estimation accuracy only through the measurement residuals or innovations. Even though we use no measurement directly unlike conventional adaptive filters, the idea of modifying the filter based on the measurements would be reasonable. Second, only the component of e_k^+ that corresponds to the measurement residual can be reduced by using δQ_k as shown in Appendix A.

Denoting $I - K_k(0)H_k$ as $\Psi_k(0)$, $e_k^+(\delta Q_k)$ can be approximated as follows.

$$\begin{aligned} e_k^+(\delta Q_k) &= x_k - \hat{x}_k^+(\delta Q_k) \\ &\approx [I - (K_k(0) + \Delta K_k)H_k]e_k^- - (K_k(0) + \Delta K_k)v_k \\ &= (\Psi_k(0) - \Delta P_k H_k^{\mathrm{T}} R_k^{-1} H_k)e_k^- - (K_k(0) + \Delta P_k H_k^{\mathrm{T}} R_k^{-1})v_k. \end{aligned} \tag{4.29}$$

Substituting (4.29) into (4.28), the measurement residual $m_k(\delta Q_k)$ can be rewritten as

$$m_k(\delta Q_k) = H_k[(\Psi_k(0) - \Delta P_k H_k^{\mathrm{T}} R_k^{-1} H_k)e_k^- - (K_k + \Delta P_k H_k^{\mathrm{T}} R_k^{-1})v_k] + v_k. \tag{4.30}$$

To formulate the problem of minimizing $m_k(\delta Q_k)$, we introduce the following function:

$$\begin{aligned} J_k(\Delta P_k) &= E\{\|m_k(\delta Q_k)\|^2_{R_k^{-1}}\} \\ &= E\{\|(\Psi_k(0) - \Delta P_k H_k^{\mathrm{T}} R_k^{-1} H_k)e_k^-\|^2_{H_k^{\mathrm{T}} R_k^{-1} H_k}\} + E\{\|(I - H_k K_k - H_k \Delta P_k H_k^{\mathrm{T}} R_k^{-1})v_k\|^2_{R_k^{-1}}\}. \end{aligned} \tag{4.31}$$

It should be noted that the objective function J_k is defined as a function of ΔP_k. Since Lemma 4.2.2 gives δQ_k corresponding to ΔP_k, we can choose ΔP_k as the decision variable instead of δQ_k.

Moreover, we denote a norm of a vector b with a weighting matrix W as

$$\|b\|_W^2 = b^{\mathrm{T}} W b.$$

Minimizing (4.31) gives

$$\Delta P_k^\star = \operatorname{argmin} J_k(\Delta P_k). \tag{4.32}$$

Substituting $\Delta P_k = \Delta P_k^\star$ into (4.24), we have

$$\delta Q_k^\star = [I - (K_k(0) + \Delta K_k^\star) H_k]^{-1} [\Delta P_k^\star - \Delta K_k^\star (H_k P_k^-(0) H_k^{\mathrm{T}} + R_k) \Delta K_k^{\star\mathrm{T}}] [I - (K_k(0) + \Delta K_k^\star) H_k]^{-T}, \tag{4.33}$$

where $\Delta K_k^\star = \Delta P_k^\star H_k^{\mathrm{T}} R_k^{-1}$ from (4.22).

4.4.2 Restriction on Fictitious Noise

Although the minimization problem is formulated by (4.32) in Sec. 4.4.1, it would be difficult to find the optimal $\Delta P_k^\star$ among all $n \times n$ positive semi-definite matrices. In this paper, we will find the solution of (4.32) by restricting ΔP_k to a certain form.

To introduce the form of ΔP_k, we make the following assumption in this subsection.

Assumption 4.4.1. *For the measurement matrix $H_k \in \mathbb{R}^{m \times n}$, $\mathrm{rank}(H_k) = m \leq n$, that is, $(H_k H_k^{\mathrm{T}})^{-1}$ exists.*

Under the assumption, H_k can be represented through singular value decomposition as follows.

$$H_k = G_k \Sigma_k S_k^{\mathrm{T}}, \tag{4.34}$$

where $G_k \in \mathbb{R}^{m \times m}$ and $S_k \in \mathbb{R}^{n \times n}$ are orthogonal matrices and $\Sigma_k \in \mathbb{R}^{m \times n}$ is expressed as

$$\Sigma_k = \begin{pmatrix} \tilde{\Sigma}_k & O_{m \times (n-m)} \end{pmatrix}. \tag{4.35}$$

$\tilde{\Sigma}_k \in \mathbb{R}^{m \times m}$ is a diagonal matrix whose diagonal elements are non-zero singular values of H_k.

Since $H_k^{\mathrm{T}} R_k^{-1} H_k$ is symmetric, it can be represented as

$$H_k^{\mathrm{T}} R_k^{-1} H_k = S_k \begin{pmatrix} \Lambda_k & O_{m\times(n-m)} \\ O_{m\times(n-m)} & O_{(n-m)\times(n-m)} \end{pmatrix} S_k^{\mathrm{T}}, \tag{4.36}$$

where $\Lambda_k \in \mathbb{R}^{m\times m}$ is a positive definite matrix whose eigenvalues are positive eigenvalues of $H_k^{\mathrm{T}} R_k^{-1} H_k$.

Then, we restrict the decision variable ΔP_k to the following form:

$$\Delta P_k = \alpha_k H_k^{\mathrm{T}} R_k^{-1} H_k + \beta_k \mathcal{H}_k^{\perp}, \tag{4.37}$$

where α_k and β_k are non-negative scalar parameters, and $\mathcal{H}_k^{\perp}$ is defined using an arbitrary positive semi-definite matrix $\Lambda_k^{\perp} \in \mathbb{R}^{(n-m)\times(n-m)}$ as

$$\mathcal{H}_k^{\perp} = S_k \begin{pmatrix} O_{m\times m} & O_{m\times(n-m)} \\ O_{m\times(n-m)} & \Lambda_k^{\perp} \end{pmatrix} S_k^{\mathrm{T}}. \tag{4.38}$$

Note that the following equation is satisfied:

$$H_k \mathcal{H}_k^{\perp} = O_{m\times n}. \tag{4.39}$$

In the rest of this subsection, we will describe the choice of the parameter β_k, because α_k will be obtained through minimization of $J_k(\Delta P_k)$ in Sec. 4.4.3. Substituting (4.37) into (4.31) and using (4.39), we obtain

$$\begin{aligned} &J_k(\Delta P_k) \\ &= E\{\|(\Psi_k(0) - \alpha_k (H_k^{\mathrm{T}} R_k^{-1} H_k)^2) e_k^-\|^2_{H_k^{\mathrm{T}} R_k^{-1} H_k}\} + E\{\|(I - H_k K_k - \alpha_k H_k H_k^{\mathrm{T}} R_k^{-1} H_k H_k^{\mathrm{T}} R_k^{-1}) v_k\|^2_{R_k^{-1}}\} \end{aligned} \tag{4.40}$$

From (4.40), the objective function $J_k(\Delta P_k)$ is depedent only on α_k by restricting ΔP_k to the form of (4.37)[1].

[1]Even if $\alpha_k H_k^{\mathrm{T}} R_k^{-1} H_k$ is replaced by $\alpha_k H_k^{\mathrm{T}} C_k H_k$ with an arbitrary positive semi-definite matrix C_k in (4.37), $J_k(\Delta P_k)$ is depedent only on α_k. That is, C_k can also be a parameter in the proposed method. In this paper, for simplicity, we choose C_k as R_k^{-1}.

Since $J_k(\Delta P_k)$ is independent of β_k, we can choose any non-negative value of β_k in the sense of minimizing $J_k(\Delta P_k)$. However, non-zero β_k may make the estimation error covariance matrix P_k^+ excessively large and cause a severe degradation of filter performance especially at the time step when H_k changes significantly from the previous ones H_{k-i}, as described in Appendix B. Therefore, we choose $\beta_k = 0$ in this paper, and then, ΔP_k becomes

$$\Delta P_k = \alpha_k H_k^{\mathrm{T}} R_k^{-1} H_k. \tag{4.41}$$

4.4.3 H-Adaptive Filter

In this section, we find the solution $\Delta P_k^\star$ of the minimization problem (4.32) under the condition that ΔP_k is restricted to the form of (4.41). Since the decision variable is reduced to only α_k, we can obtain $\Delta P_k^\star$ analytically.

To derive the analytical solution that does not need the measurements y_k themselves, we make the following assumption:

Assumption 4.4.2. *$E\{(e_k^-)(e_k^-)^{\mathrm{T}}\}$ can be approximated as $E\{(e_k^-)(e_k^-)^{\mathrm{T}}\} = P_k^-$.*

For brevity of notation, we denote $H_k^{\mathrm{T}} R_k^{-1} H_k$ as O_k in this subsection.

Noticing that we can suppose that O_k is a non-zero and positive semi-definite matrix, $\Delta P_k^\star$ is given by the following lemma.

Lemma 4.4.1. *Under the Assumption 4.4.2, the solution to the minimization problem* (4.32) *is derived for ΔP_k in the form of* (4.41) *as follows.*

$$\Delta P_k^\star = \alpha_k^\star O_k, \tag{4.42}$$

$$\alpha_k^\star = \frac{\mathrm{tr}\,[O_k^2]}{\mathrm{tr}\,[O_k^5 P_k^- + O_k^4]}. \tag{4.43}$$

Proof. Since $J(\Delta P_k)$ is a quadratic function of α_k, we can solve the problem by finding $\alpha_k^\star$ that satisfies

$$\left.\frac{\partial J(\Delta P_k)}{\partial \alpha_k}\right|_{\alpha_k = \alpha_k^\star} = 0. \tag{4.44}$$

The left-hand side of (4.44) can be calculated as

$$
\begin{aligned}
&\frac{1}{2}\frac{\partial J(\Delta P_k)}{\partial \alpha_k} \\
&= E\{-e_k^{-\mathrm{T}} O_k^3 \Psi_k(0) e_k^- + \alpha_k e_k^{-\mathrm{T}} O_k^5 e_k^- - v_k^{\mathrm{T}} R_k^{-1} H_k O_k H_k^{\mathrm{T}} R_k^{-1} (I - H_k K_k(0)) v_k + \alpha_k v_k^{\mathrm{T}} R_k^{-1} H_k O_k^3 H_k^{\mathrm{T}} R_k^{-1} v_k\} \\
&= \mathrm{tr}\,[\alpha_k O_k^5 P_k^-] - \mathrm{tr}\,[O_k^3 P_k^- \Psi_k^{\mathrm{T}}(0)] + \mathrm{tr}\,[\alpha_k O_k^4] - \mathrm{tr}\,[H_k O_k H_k^{\mathrm{T}} (I - H_k K_k(0))^{\mathrm{T}} R_k^{-1}] \\
&= \alpha_k \mathrm{tr}\,[O_k^5 P_k^- + O_k^4] - \mathrm{tr}\,[O_k^2], \qquad (4.45)
\end{aligned}
$$

where we used (4.14) and the following equations.

$$
\begin{aligned}
\mathrm{tr}\,[H_k O_k H_k^{\mathrm{T}} (I - H_k K_k(0))^{\mathrm{T}} R_k^{-1}] &= \mathrm{tr}\,[H_k O_k H_k^{\mathrm{T}} R_k^{-1} - H_k O_k H_k^{\mathrm{T}} K_k^{\mathrm{T}}(0) H_k^{\mathrm{T}} R_k^{-1}] \\
&= \mathrm{tr}\,[O_k^2] - \mathrm{tr}\,[K_k(0) H_k O_k^2], \\
\mathrm{tr}\,[O_k^3 P_k^- \Psi_k^{\mathrm{T}}(0)] &= \mathrm{tr}\,[O_k^2 H_k^{\mathrm{T}} R_k^{-1} H_k P_k^+(0)] \\
&= \mathrm{tr}\,[K_k(0) H_k O_k^2].
\end{aligned}
$$

From (4.44) and (4.45), we obtain (4.43). □

It should be noted that, from (4.43), $\alpha_k^\star$ satisfies $\alpha_k^\star > 0$.

From Lemma 4.2.1, 4.2.2 and 4.4.1, the filter proposed in this paper is summarized as follows.

Time update:

$$
\begin{aligned}
\hat{x}_k^- &= f(\hat{x}_{k-1}^+), \\
P_k^-(\delta Q_k^\star) &= F_{k-1} P_{k-1}^+ F_{k-1}^{\mathrm{T}} + Q_{k-1} + \delta Q_k^\star, \qquad (4.46)
\end{aligned}
$$

Measurement update:

$$
\begin{aligned}
\hat{x}_k^+(\delta Q_k^\star) &= \hat{x}_k^- + K_k(\delta Q_k^\star)[y_k - h(\hat{x}_k^-)], \qquad (4.47) \\
P_k^+(\delta Q_k^\star) &= [I - K_k(\delta Q_k^\star) H_k] P_k^-(\delta Q_k^\star) \\
&= P_k^+(0) + \Delta P_k^\star, \qquad (4.48) \\
K_k(\delta Q_k^\star) &= P_k^-(\delta Q_k^\star) H_k^{\mathrm{T}} [H_k P_k^-(\delta Q_k^\star) H_k^{\mathrm{T}} + R_k]^{-1} \\
&= K_k(0) + \Delta K_k^\star, \qquad (4.49)
\end{aligned}
$$

where

$$
\begin{aligned}
O_k &= H_k^{\mathrm{T}} R_k^{-1} H_k, \\
\alpha_k^\star &= \frac{\operatorname{tr} O_k^2}{\operatorname{tr} O_k^5 P_k^- + O_k^4}, \\
\Delta P_k^\star &= \alpha_k^\star O_k, \\
\Delta K_k^\star &= \Delta P_k^\star H_k^{\mathrm{T}} R_k^{-1}, \\
\delta Q_k^\star &= [I - (K_k(0) + \Delta K_k^\star) H_k]^{-1} [\Delta P_k^\star - \Delta K_k^\star (H_k P_k^-(0) H_k^{\mathrm{T}} + R_k) \Delta K_k^{\star\mathrm{T}}] [I - (K_k(0) + \Delta K_k^\star) H_k]^{-T}.
\end{aligned}
$$

In the above filter, fictitious noise $\delta Q_k^\star$ is chosen at each time step depending on the measurement matrix H_k, not on the measurement itself. Therefore, we call the filter with the proposed choice of fictitious noise H-adaptive filter.

The H-adaptive filter inflates the estimation error covariance matrix P_k^+ in the row space of H_k. Thus, the H-adaptive filter forgets information to some extent in the row space of H_k compared to the standard Kalman filter. In this sense, it can be regraded as one fading memory filter. However, the fading memory filter forgets information uniformly in every direction, while the H-adaptive filter forgets only in the row space of H_k. Since new information can be obtained in the row space of H_k at time step k, forgetting some prior information in the row space would not degrade the estimation accuracy. On the other hand, forgetting prior information perpendicular to the row space of H_k excessively would lead to the degradation of estimation accuracy, because no information in that direction is provided from the measurement.

Moreover, Lemma 4.2.2 does not guarantee that $\delta Q_k^\star$ corresponding to $\Delta P_k^\star$ is a positive semi-definite matrix, although $\delta Q_k^\star$ was always positive semi-definite in the numerical and experimental examples shown in the following two sections. If $\delta Q_k^\star$ becomes negative in the above filter, we could replace at that time step (4.42) with $\Delta P_k^\star = s_k \alpha_k^\star O_k$ to get a positive semi-definite $\delta Q_k^\star$ by using $s_k \in (0, 1)$.

4.5 Application

4.5.1 Stationary Positioning

This section shows experimental results in stationary positioning with the proposed process noise model derived in Sec. 4.3. We recall the extended Kalman filter for stationary positioning introduced in Sec. 3.4.1 in Chapter 3, but the state vector is replaced with

$$x = [r^{\mathrm{T}}, t_s^{\mathrm{T}}, t, \dot{t}]^{\mathrm{T}}, \tag{4.50}$$

where r [m] is the position vector of a GNSS receiver, t [m] is a clock bias, and $\dot{t}$ [m/s] is a clock drift. Note that we remove ISBs from the state vector. Although we use multiple GNSS constellations concurrently in Chapter 3, we use only GPS in this experiment to simulate poor satellite geometry by reducing the number of satellites. We use (4.19) in a time update to apply fictitious noise δQ_k to the EKF.

We demonstrate the effectiveness of the process noise model presented in Sec. 4.3 in the scenario of GNSS positioning in urban environments. As shown in Fig. 4.1, we collected GNSS data (raw measurements and ephemerides) through an antenna fixed at the roof of a building by using a single-frequency GNSS receiver, Furuno GN-8720, for twelve hours. Although the antenna is in open-sky conditions, we create 72 data sets of 600 [s] by assuming that the satellites whose elevation angles θ satisfy $\theta \geq 15^\circ$ are visible from the start to 299 time steps, and the satellites that satisfy $\theta \geq 55^\circ$ are visible from 300 time steps to the end. Those data sets are intended to simulate the data sets of antennas that move from open sky areas to urban areas. For the data sets, the average number of visible satellites is 7.8 for $\theta \geq 15^\circ$, and 2.1 for $\theta \geq 55^\circ$ (See Fig. 4.2 for satellite geometry in the data sets). We used only GPS L1C/A signals at each time step.

We also assume that there is a modeling error in the clock drift dynamics, in order to show that δQ_k in (4.27) can avoid the filter divergence while suppressing the degradation due to the unintentional inflation of P_k. A constant bias b was introduced in the clock drift dynamics as follows:

$$\dot{t}_k = \dot{t}_{k-1} + b + w_{tk}, \tag{4.51}$$

Figure 4.1: Data collection by a fixed GNSS antenna. The antenna is located at 34.7136832 [deg] north latitude and 135.3353441 [deg] east longitude. There are few obstacles around the antenna that block direct signals from satellites.

where w_{tk} is the process noise of clock drift, and b was chosen as $b = 0.1$ [m/s]. As mentioned in Chapter 1, a modeling error in the clock drift dynamics can occur for low-cost GNSS receivers due to temperature changes, acceleration, and so on.

Using the above 72 data sets, we estimated the state vector x in (4.50) by the extended Kalman filter with the following three settings of fictitious noise.

Setting (1): Nominal choice, $\delta Q_k = O$.

Setting (2): Conventional choice in a naïve manner, $\delta Q_k = qI$, where $q = 0.01$.

Setting (3): Proposed choice with a fixed parameter, $\delta Q_k = \alpha W_k$, where $\alpha = 0.01$.

The process noise covariance Q_k was chosen from the literature [1] as

$$Q_k = \begin{pmatrix} O_{3\times3} & 0 & 0 \\ O_{1\times3} & 0.013 & 0.005 \\ O_{1\times3} & 0.005 & 0.01 \end{pmatrix}. \tag{4.52}$$

Note that the value of Q_k achieves an accuracy of less than 6 [m] (2DRMSE) in open-sky conditions with Setting (1), if the cut-off elevation angle is low. The accuracy is almost the same as the one of a typical consumer receiver.

To compare the results obtained with the three settings, we define the following variable $r_k(i)$ that represents the norm of estimation-errors in (e, n, u, t) at time step k for ith data set:

$$r_k(i) = \sqrt{\tilde{x}_k^{\mathrm{T}}(i)\tilde{x}_k(i)}, \tag{4.53}$$

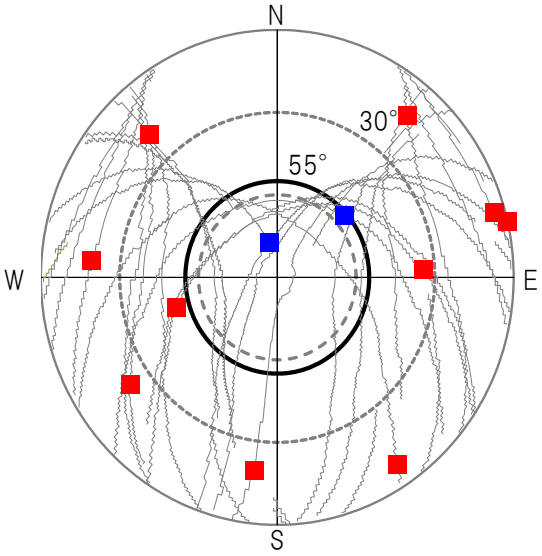

Figure 4.2: Satellite geometry for 12 hours as seen by a receiver. The blue and red dots represent an example of skyplot at 12:02:38(UTC), December 11, 2020. A blue dot is a satellite whose elevation angle is above 55 [deg], and a red dot is a satellite whose elevation angle is below it.

where $\tilde{x} = [\tilde{e}(i), \tilde{n}(i), \tilde{u}(i), \tilde{t}(i))]^{\mathrm{T}}$, and $\tilde{e}$, $\tilde{n}$, $\tilde{u}$ and $\tilde{t}$ are the estimation-errors of e, n, u and t respectively. Then, the ensemble averages of $r_k(i)$ and estimation-error of clock drift $\tilde{t}_k(i)$ are computed as

$$\bar{\tilde{t}}_k = \frac{1}{N}\sum_{i=1}^{N}\tilde{t}_k(i), \quad \bar{r}_k = \frac{1}{N}\sum_{i=1}^{N} r_k(i), \tag{4.54}$$

where $N = 72$.

Fig. 4.3 shows the ensemble averages $\bar{\tilde{t}}_k$ and $\bar{r}_k$ obtained for the three settings of process noise model. Both errors $\bar{\tilde{t}}_k$ and $\bar{r}_k$ for Setting (3) are much smaller than those for Setting (1) at each time step. Although $\bar{\tilde{t}}_k$ for Setting (1) increases from the start time due to the bias error b, $\bar{\tilde{t}}_k$ for Setting (3) remains almost zero because of the fictitious process noise in (4.26) or (4.27). Even after the number of visible satellites is reduced for $k \geq 300$, $\bar{\tilde{t}}_k$ for Setting (3) is kept sufficiently small. The error $\bar{r}_k$ for Setting (3) is reduced by 20 [%] for $k \geq 300$ and 10 [%] for $k < 300$ compared with the one for Setting (1). On the other hand, $\bar{\tilde{t}}_k$ for Setting (2) is reduced to some extent because of the fictitious process noise $\delta Q_k = qI$. However, the error $\bar{r}_k$ for Setting (2) increases from the start time compared to Setting (1), and rapidly for $k \geq 300$. This could be because the fictitious process noise $\delta Q_k = qI$ makes the estimation-error covariance P_k inflate unintentionally along a certain direction. These results show that Setting (3) can achieve the

mitigation of estimation errors caused by modeling errors and the reduction of the unintentional inflation of P_k simultaneously.

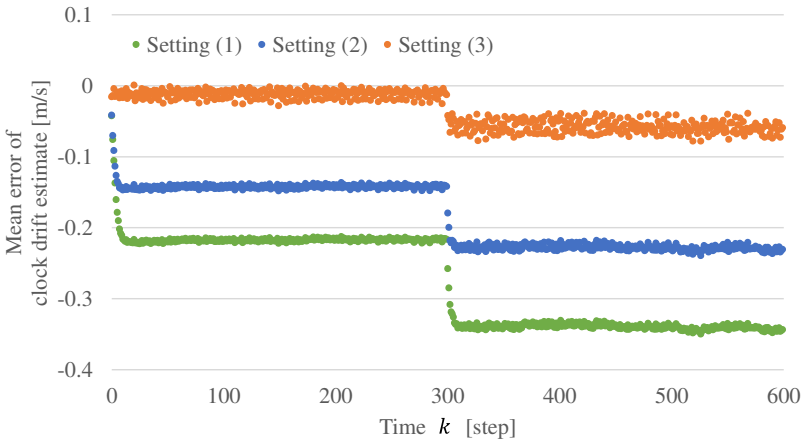

(a) Ensemble average $\bar{t}_k$.

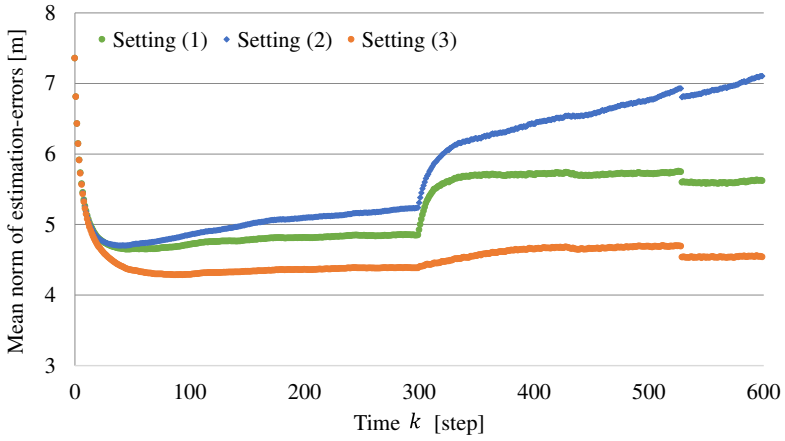

(b) Ensemble average $\bar{r}_k$.

Figure 4.3: Estimation errors for three settings of process noise model.

4.5.2 GNSS/INS Positioning

This section presents a practical application of the H-adaptive filter to a vehicle positioning with Global Navigation Satellite System (GNSS) and Inertial Navigation System (INS) (Fig. 4.4). Since GNSS and INS are complementary in terms of error characteristics, their integration is commonly employed to improve positioning accuracy for automobiles. The integration is accomplished in a tightly coupled manner by the extended Kalman filter as shown in Fig. 4.5.

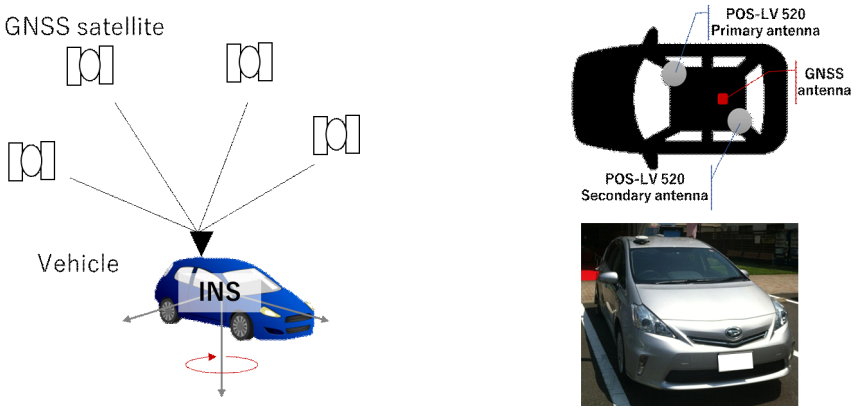

(a) (b)

Figure 4.4: Positioning system with GNSS/INS for a test vehicle. (a) Vehicle positioning with GNSS/INS. (b) Test vehicle.

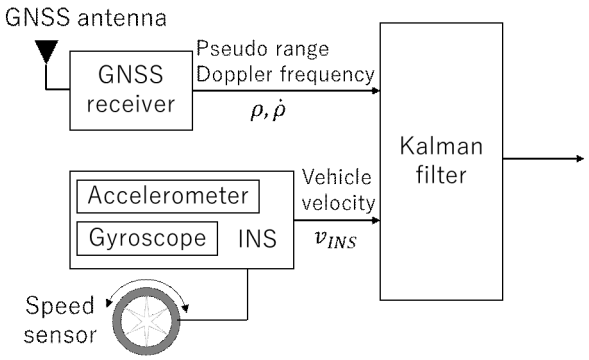

Figure 4.5: Block diagram of a tightly coupled integration of GNSS and INS.

The state and measurement vectors are given as

$$x = (r^{\mathrm{T}}, \delta t, \dot{r}^{\mathrm{T}}, \delta \dot{t}, b^{\mathrm{T}})^{\mathrm{T}}, \tag{4.55}$$

$$y = (\rho^{\mathrm{T}}, \dot{\rho}^{\mathrm{T}}, v_{INS}^{\mathrm{T}})^{\mathrm{T}}, \tag{4.56}$$

where r [m] is a position vector in $\mathbb{R}^3$ represented in the Earth-Centered-Earth-Fixed(ECEF) coordinates, and $\dot{r}$ [m/s] is a velocity vector in the ECEF coordinates. The clock bias and drift of GNSS receiver are denoted as δt [m] and $\delta \dot{t}$ [m/s] in $\mathbb{R}$ respectively. When multiple $(l+1)$ GNSS constellations such as GPS and Galileo are used for positioning, inter-system biases (ISBs), defined as the difference between the GPS's system clock and other GNSS systems'clock, are included as a $l-$dimensional vector b [m] in x. In the measurement vector y, pseudo ranges and Doppler frequencies obtained from the signals of m satellites are denoted as ρ [m] and $\dot{\rho}$ [m/s]

in $\mathbb{R}^m$ respectively. The velocity vector provided from INS is represented as $v_{INS} \in \mathbb{R}^3$. For further details on GNSS/INS positioning, see, for example, [9, 1, 54].

The state and measurement equations for this system are

$$\begin{aligned} x_{k+1} &= f(x_k) + w_k \\ &= F x_k + w_k, \end{aligned} \tag{4.57}$$

$$y_k = h(x_k) + v_k, \tag{4.58}$$

where, denoting the ith element of $h(x_k)$ as $h_i(x_k)$,

$$h_i(x_k) = \begin{cases} \|r_k - r_k^i\| + \delta t_k + b_k(i) & 1 \le i \le m \\ e_{i,k}^{\mathrm{T}}(\dot{r}_k - \dot{r}_k^i) + \delta \dot{t}_k & m+1 \le i \le 2m \end{cases}, \tag{4.59}$$

$$(h_{2m+1}(x_k), h_{2m+2}(x_k), h_{2m+3}(x_k))^{\mathrm{T}} = \dot{r}_k, \tag{4.60}$$

$$e_{i,k} = \frac{r_k - r_k^i}{\|r_k - r_k^i\|}, \tag{4.61}$$

$$F = \begin{pmatrix} I_{4\times4} & \Delta t I_{4\times4} & O_{4\times l} \\ O_{4\times4} & I_{4\times4} & O_{4\times l} \\ O_{l\times4} & O_{l\times4} & I_{l\times l} \end{pmatrix}.$$

In (4.59), r_k^i denotes the position vector of satellite i, and $b_k(i)$ is the ISB of the constellation that satellite i belongs to.

To construct the extended Kalman filter, nominal noises Q_k and R_k are set based on [1, 30, 49, 50, 55] as follows:

$$Q_k = \begin{pmatrix} Q_1 & \tilde{Q} & O_{4\times l} \\ \tilde{Q}^{\mathrm{T}} & Q_2 & O_{4\times l} \\ O_{l\times4} & O_{l\times4} & 0.01 I_{l\times l} \end{pmatrix}, \ \tilde{Q} = \begin{pmatrix} O_{3\times3} & O_{3\times1} \\ O_{1\times3} & 0.005 \end{pmatrix}, \tag{4.62}$$

$$Q_1 = \begin{pmatrix} \mathrm{diag}(0.16, 0.003\|v_{INS}\|^2, 10^{-5}) & O_{3\times1} \\ O_{1\times3} & 0.013 \end{pmatrix}, \ Q_2 = \begin{pmatrix} \mathrm{diag}(0.64, 10^{-5}, 10^{-5}) & O_{3\times1} \\ O_{1\times3} & 0.01 \end{pmatrix},$$

$$R_k = \mathrm{diag}(\sigma_1^2, \ldots, \sigma_m^2, \dot{\sigma}_1^2, \ldots, \dot{\sigma}_m^2, c_1, c_2, c_3), \tag{4.63}$$

where, denoting the SNR of the signal from the ith satellite as s_i ($i = 1, \cdots, m$), $\sigma_i = 0.64 + 784e^{-0.142 s_i}$, $\dot{\sigma}_i = 0.0125 + 6767e^{-0.267 s_i}$, and $c_1 = c_2 = c_3 = 0.16$.

However, note that the process model of the GNSS/INS integration mainly depends on INS accuracy. The INS accuracy often decreases due to unexpected sensor errors, which would make the process model inaccurate. Consequently, the above nominal Q_k may be relatively small.

In addition, it is also known that estimation accuracy in the lateral and vertical directions of a vehicle tends to degrade in urban areas [49, 50]. As shown in Fig. 4.6, satellite signals from the lateral direction of a vehicle are often blocked by obstacles such as tall buildings. The information from the satellite signals is nearly degenerate due to a biased distribution of visible satellites.

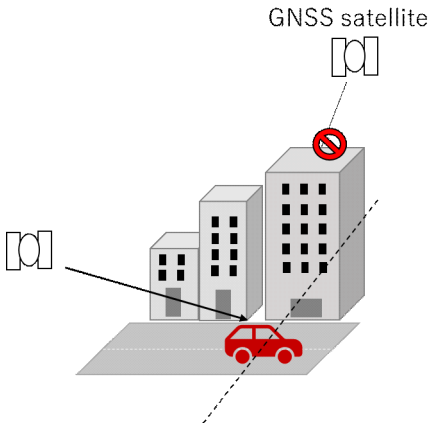

Figure 4.6: Biased distribution of visible satellites in urban areas.

Experimental Results

Let us begin with the introduction to settings for process nosie covariance. The extended Kalman filter for GNSS/INS positioining is constructed in the following three settings.

Setting (1): The filter is a conventional extended Kalman filter with

$$\delta Q_k = O. \tag{4.64}$$

Setting (2): The filter corresponds to fading memory filter [51, 42] by choosing δQ_k as

$$\delta Q_k = c F_{k-1} P^+_{k-1} F_{k-1}, \tag{4.65}$$

where $c = 0.03$.

Setting (3): The filter is H-adaptive filter with

$$\delta Q_k = \delta Q_k^\star, \tag{4.66}$$

where $\delta Q_k^\star$ is given by (4.33).

In Setting (2), c was set to be 0.03, because the estimation accuracy with $c = 0.03$ was the highest among those with $c = \{0.01, 0.02, \cdots, 0.07\}$. By using the test vehicle shown in Fig. 4.4, we collected the measurement data and performed the state estimation by the filters in the three settings.

The measurements y were obtained by a vehicle positioning system (FURUNO GN-87, Bosch SMI130, and vehicle speed pulse sensor) installed in the test vehicle. A reference system (Applanix POS-LV 520) was also installed to provide highly accurate positions. We can calculate the positioning errors of the three filters by using the positions from the reference system as true positions.

The test vehicle made eight laps of the route shown in Fig. 4.7, running for 4330 seconds. The visibility of satellites from the vehicle varies significantly on the route. At A point, the vehicle is surrounded by a lot of objects located in its lateral direction. At B point, there is no object blocking the signals from the satellites to the vehicle.

We show the visibility of satellites on the route by introducing the well-known indicator PDOP (Position Dilution of Precision) [1]. PDOP at the time step k is defined as

$$\mathrm{PDOP}(k) = \sqrt{\sum_{p=1}^{3} [(\tilde{H}_k^{\mathrm{T}} \tilde{H}_k)^{-1}]_p},$$

where $[A]_p$ means the pth diagonal element of a matrix A, and, denoting the estimated value of $e_{i,k}$ as $\hat{e}_{i,k}$,

$$\tilde{H}_k = \begin{pmatrix} \hat{e}_{1,k} & \cdots & \hat{e}_{m,k} \\ 1 & \cdots & 1 \end{pmatrix}^{\mathrm{T}}.$$

When PDOP is larger, the visibility of satellites is lower, and the positioning accuracy tends to degrade. The average value of PDOP for all the time steps of 4330 [sec] was 2.8, and the

maximum and minimum value in the experiment were 15.8 and 1.8. At A point, PDOP was about 4.3, that is, the visibility was lower than at other points. At B point, PDOP was about 2.1, and the visibility was higher.

Figure 4.7: Route of the positioning experiment by a test vehicle in Nishinomiya city, Japan. It is shown by green dots obtained from the reference system (Applanix POS-LV 520).

The positioning accuracies on the entire route in the three settings were computed as RMSEs in the body coordinate frame, and are summarized in Table 4.1, where x, y and z are RMSEs in the longitudinal (forward), lateral and vertical directions of the vehicle. We can see that the accuracy in Setting (3) is the highest in every direction among them. Although the measurement matrix H_k varied largely according to the visibility of satellites on the route, the H-adaptive filter reduced the estimation error by choosing the fictitious noise δQ_k appropriately.

To examine the positioning accuracy near A and B points, we computed the RMSEs using the data from the time steps when the vehicle was in the neighborhood of each point. Tables 4.2 and 4.3 show the results for A and B points respectively, where the RMSEs were calculated from 80 data points created by collecting 10 time step data points around A or B point in each lap. In Table 4.2 for A point, the accuracies in all the settings degrade due to the lower visibility of satellites. However, the degradation is the smallest in Setting (3), and the H-adaptive filter achieves quite better accuracy compared to other two filters. In Table 4.3 for B point, the accuracies in all the settings become better because of the higher visibility of satellites. Even when sufficient information is obtained from the measurements, the H-adaptive filter works well while achieving the same level of accuracy as the fading memory filter.

Table 4.1: RMSEs for positioning on the entire route.

	x [m]	y [m]	z [m]
(1) Extended Kalman filter	2.0	2.2	4.4
(2) Fading memory filter	1.9	2.0	3.7
(3) H-adaptive filter	1.9	1.8	3.1

Table 4.2: RMSEs for positioning around A point.

	x [m]	y [m]	z [m]
(1) Extended Kalman filter	2.2	3.3	6.3
(2) Fading memory filter	2.2	3.1	3.9
(3) H-adaptive filter	1.9	2.4	3.1

4.5.3 Robot Localization

Localization for Motion Robot

In this section, we demonstrate the effectiveness of H-adaptive filter through numerical simulations for localization of a mobile robot [56]. We consider a mobile robot that moves on the XY plane where there are several landmarks, as in Fig. 4.8. The position and heading angle of the robot are denoted as $r = (r_X, r_Y)^{\mathrm{T}}$ [m] and θ [rad] respectively. The position of the jth landmark is represented as $m_j = (m_{j,X}, m_{j,Y})^{\mathrm{T}}$ [m], and assumed to be known. It is also supposed that a camera is installed in the robot along its heading to measure distances and angles from the robot to visible landmarks. Measurements from the jth landmark are expressed as $y_j = (l_j, \varphi_j)^{\mathrm{T}}$, where l_j [m] is the distance and φ_j [rad] is the angle.

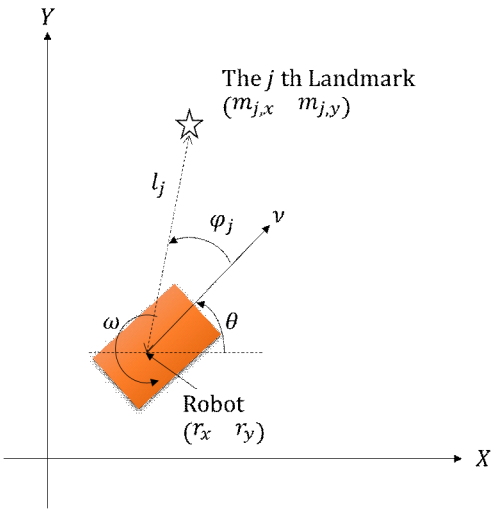

Figure 4.8: Localization of a mobile robot

Table 4.3: RMSEs for positioning around B point.

	x [m]	y [m]	z [m]
(1) Extended Kalman filter	1.1	0.9	3.7
(2) Fading memory filter	1.1	0.9	1.7
(3) H-adaptive filter	1.1	0.9	1.6

The state and velocity input vectors for the robot are defined as $x = (r_X, r_Y, \theta)^{\mathrm{T}}$ and $u = (\nu, \omega)^{\mathrm{T}}$, where ν [m/s] is the translational velocity and ω [rad/s] is the angular velocity. The state and measurement equations are as follows:

$$\begin{aligned} x_k &= f(x_{k-1}, u_k) \\ &= x_{k-1} + \begin{pmatrix} \nu_k \omega_k^{-1} [\sin(\theta_{k-1} + \omega_k \Delta t) - \sin\theta_{k-1}] \\ \nu_k \omega_k^{-1} [-\cos(\theta_{k-1} + \omega_k \Delta t) + \cos\theta_{k-1}] \\ \omega_k \Delta t \end{pmatrix}, \end{aligned} \tag{4.67}$$

$$\begin{aligned} y_{j,k} &= h_j(x_k) + v_{j,k} \\ &= \begin{pmatrix} \sqrt{(m_{j,X} - r_{k,X})^2 + (m_{j,Y} - r_{k,Y})^2} \\ \arctan 2((m_{j,Y} - r_{k,Y}), (m_{j,X} - r_{k,X})) - \theta \end{pmatrix} + v_{j,k}, \end{aligned} \tag{4.68}$$

where $v_{j,k}$ is a Gaussian measurement noise, that is, $v_{j,k} \sim N(0, R_{j,k})$. Note that, if $\omega_k = 0$, (4.67) becomes $x_k = x_{k-1} + (\nu_k \Delta t \cos(\theta_{k-1}), \nu_k \Delta t \sin(\theta_{k-1}), 0)^{\mathrm{T}}$.

The uncertainties in the process model (4.67) are introduced by adding a disturbance w_k to the velocity vector u_k as

$$u'_k = u_k + w_k. \tag{4.69}$$

The disturbance w_k was set based on [56] in the simulations below, assuming that it consists of two components: bias due to, e.g., the load imbalance of a robot and random noise due to, e.g., pebbles on the robot's path. Then, (4.67) is replaced with

$$x_k = f(x_{k-1}, u'_k). \tag{4.70}$$

Simulation Results

We performed numerical simulations where the robot moves at $u_k = (0.2, 0.0)^{\mathrm{T}} (k \geq 1)$ from $x_0 = (-2.0, 0, 0)^{\mathrm{T}}$ on the XY plane. Three landmarks whose positions are $(m_{1,k,X}, m_{1,k,Y}) = (4.5, 0)$, $(m_{2,k,X}, m_{2,k,Y}) = (4.5, 2.0)$, and $(m_{3,k,X}, m_{3,k,Y}) = (4.5, -2.0)$ exist on the plane. Referring to [56], the jth landmark is assumed to be visible when it satisfies the following conditions: $|\bar{\mathfrak{l}}_j| < \varepsilon_l \wedge |\bar{\varphi}_j| < \varepsilon_\varphi$ for $j = 1$ and $|\bar{\mathfrak{l}}_j| < \varepsilon_l \wedge |\bar{\varphi}_j| < \varepsilon_\varphi \wedge z_{j,k} > \varepsilon$ for $j = 2, 3$, where $\bar{\mathfrak{l}}_j$ and $\bar{\varphi}_j$ are the true distance and angle of the jth landmark, and $z_{j,k}$ is a uniformly distributed random variable on $[0, 1]$. The parameters ε_l, ε_φ and ε were chosen as 6.0 [m], $\pi/3$ [rad] and 0.99 respectively. These conditions mean that measurements $y_{2,k}$ and $y_{3,k}$ can rarely be obtained due to large ε, that is, the observability is degenerate at almost all time steps.

Localization was accomplished by the EKF in the same three settings as in Sec. 4.5.2. Recall that Setting (1) is for conventional extended Kalman filter, Setting (2) is for fading memory filter, and Setting (3) is for H-adaptive filter. Note that, in Setting (2), the parameter c was set to 0.04 in this experiment. In all the settings, the nominal Q_k is computed at each time step assuming the covariances of the noises in v_k and ω_k to be 0.0025 and 0.0027 respectively, and the nominal $R_{j,k}$ is given as $\mathrm{diag}(0.01, 0.001)$.

The numerical simulations were performed 25 times with different noise sequences $\{w_k\}$ and $\{v_k\}$ for the filters in the above three settings, where the time step k was increased from 0 to 250 with $\Delta t = 0.1$ [s]. The estimation accuracy at the final time step $k = 250$ was examined by calculating the root mean squared error (RMSE) for 25 estimated states at $k = 250$ for each setting, as shown in Table 4.4. The highest accuracy was obtained with the setting (3), namely H-adaptive filter.

To illustrate the accuracy difference among the three settings, the behaviors of the true robot and the estimated state on the XY plane for one set of noise sequences $\{w_k\}$ and $\{v_k\}$ are shown in Fig. 4.9 as an example. In the figure, the true position and estimated position of the robot are drawn by the black and blue lines respectively. The estimation error covariance P_k^+ calculated by the filter is also drawn in blue every 50 steps as a 3σ ellipse [57]. The behaviors in each setting will be described below.

In Setting (1), the true position of robot is outside the ellipse at the final time step in Fig. 4.9(a). We can see that the estimation error covariance matrix becomes very small, and the filter divergence is caused. It would be because the nominal Q_k is too small to cover the

model error. Moreover, the ratio of the major and minor axes of the final ellipse is 4.11.

In Setting (2), the true positions of robot are inside the ellipses even at the final time step in Fig. 4.9(b), but all the ellipses are too large. The unnecessarily inflated ellipses cause very large estimation errors (see also Appendix B), although they avoid the filter divergence. Moreover, the ratio of the major and minor axes of the last ellipse is 10.2 in this setting. The ellipses are more inflated in the direction perpendicular to the line of sight of the first landmark as shown in Fig. 4.9(b), which results in the larger ratio compared to the one in Setting (1).

In Setting (3), the true positions are inside the ellipses at all the time steps, and the size of the ellipses looks to be kept reasonable. As a result, the H-adaptive filter achieves the highest estimation accuracy. The ratio of the major and minor axes is 4.09, which is close to the one in Setting (1). It indicates that the H-adaptive filter avoided excessive inflation of P_k^+ along the direction perpendicular to the row space of H_k by choosing $\beta_k = 0$.

Table 4.4: RMSEs in state estimation at the final time step.

	r_x [m]	r_y [m]	θ [rad]
(1) Extended Kalman filter	0.32	0.55	0.29
(2) Fading memory filter	0.21	0.43	0.25
(3) H-adaptive filter	0.10	0.17	0.12

4.6 Conclusion

This chapter presented the extended process noise model that is the first to choose process noise based on measurement matrices as far as we know. The model enables the filter to reduce unexpected estimation errors due to dynamics uncertainties while avoiding performance degradation due to fictitious noise. We call the filter with the extended process noise model H-adaptive filter. Since the H-adaptive filter is based on the sensitivity analysis of the estimation error covariance matrix due to fictitious noise for a generic linearized system, they can be be employed in applications other than GNSS positioning, such as GNSS/INS positioning and robot localization. We demonstrated the H-adaptive filter to show the improvement of estimation accuracy through experiments and numerical simulations.

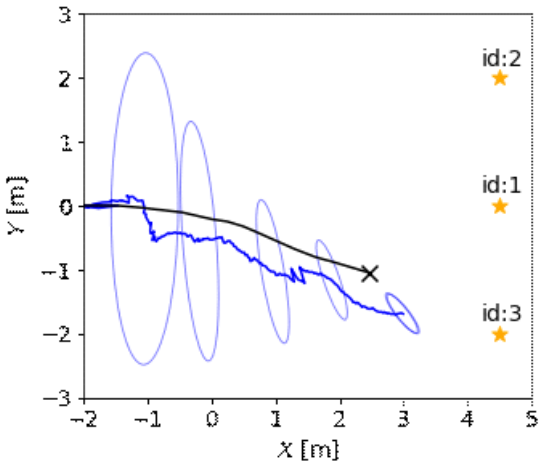

(a) Extended Kalman filter

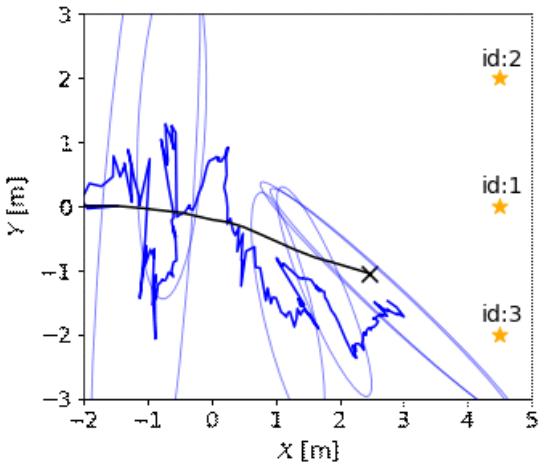

(b) Fading memory filter

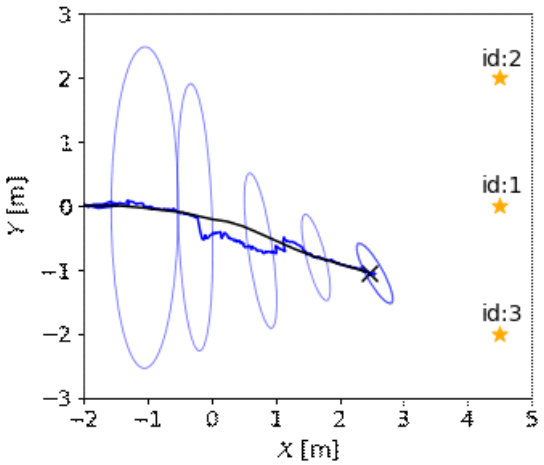

(c) H-adaptive filter

Figure 4.9: Numerical results for localization of a robot by three filters. Black and blue lines are the true and estimated positions of the robot respectively, and blue ellipses represent 3σ error ellipses. (a) Setting (1): Extended Kalman filter. (b) Setting (2): Fading memory filter. (c) Setting (3): H-adaptive filter.

Chapter 5

Conclusion

This thesis reported the research results on performance improvement of the extended Kalman filter for single point positioning in urban canyons. First, this chapter reviews the contents of each chapter from Chapter 1 to 4. Second, the contribution of this thesis is summarized with the possibility of expanding the proposed process noise model derived in Chapter 4 to other applications and nonlinear filters. Finally, future work is described to obtain more accurate positions in urban canyons.

Chapter 1 described the current GNSS status from the point of view of position accuracy and introduced the problem of inaccuracy in urban canyons. Three background materials were provided, i.e., the single point positioning with the EKF, NLOS and multipath signals, and satellite geometry. Further, this chapter wrote a mathematical introduction to the EKF for single point positioning used throughout this thesis.

Chapter 2 was devoted to developing a method to reject measurement outliers due to NLOS reception that can considerably degrade position accuracy in urban canyons. This chapter began with an introduction to the adaptive EKF, a filter that can adjust the noise input level of measurement outliers. And then, this chapter introduced a model that represents the surrounding environment of a GNSS receiver to predict path delays due to reflection or diffraction. The rejection method is based on the model and can reject measurements whose innovations are unexpectedly significant compared to the predicted path delays. Performance improvement with the proposed method was shown through driving tests in an urban area, Shinjuku, Tokyo, Japan.

Chapter 3 began with numerical examples and theoretical analysis showing the unintended degradation of position accuracy in urban canyons caused by rejecting NLOS signals. The re-

jection of NLOS signals would result in poor satellite geometry. Poor satellite geometry is a biased distribution of satellites. Keeping this in mind, recall that process noise covariance in the EKF tends to be chosen heuristically. The theoretical analysis showed that a naïve choice of process noise could unintentionally make the estimation error covariance in the EKF large with poor satellite geometry. Since this inflation can degrade accuracy, this chapter proposed a process noise model based on satellite geometry to suppress the unintended inflation of the estimation error covariance under some assumptions. It was demonstrated that position accuracy was improved through experiments in stationary positioning.

Chapter 4 presented an extended process noise model based on the model derived in Chapter 3. The extended process noise model is designed to vary fictitious noise depending on measurement matrices, that is, satellite geometry. This chapter began with the sensitivity analysis of the estimation error covariance matrix due to fictitious noise without the assumptions introduced in Chapter 3. From the sensitivity analysis, fictitious noise makes the estimation error covariance matrix variation. And then, this chapter designed two patterns of fictitious noise based on measurement matrices and demonstrated performance improvement with each design of fictitious noise. Moreover, the numerical simulation of robot localization was shown with the extended process noise model to show the possibility that the model can be applied to other applications. The contribution of the extended process noise is given in the rest of this chapter.

Poor satellite geometry caused by NLOS signal rejection can degrade position accuracy unintentionally in urban canyons with the extended Kalman filter. We have proposed a process noise model based on satellite geometry to avoid preventing degradation. Since the model can be implemented into all types of GNSS receivers, the model could be conducive to solving the problem of inaccuracy in urban canyons.

Although many researchers have approached problem-solving for inaccuracy in urban canyons from the point of view of rejecting measurement outliers, they have yet to show how poor satellite geometry caused by rejection affects the EKF as far as we know. This thesis has pointed out that fictitious noise to cover dynamics uncertainty in the EKF causes unintentional inflation of the estimation error covariance in the EKF. The unintended inflation can degrade the EKF performance in urban canyons. We have shown the sensitivity of the estimation error covariance matrix due to fictitious noise and proposed a process noise model based on satellite geometry. The process noise model would play an essential role in single point positioning in urban

canyons with the EKF. The outcomes of our work could be new findings in the GNSS field.

The process noise model can be applied to other applications. Measurement degeneracy, like poor satellite geometry, often occurs in other applications [58]. For example, a robot localization usually uses a camera or a range sensor to measure the distance between a robot and landmarks around the robot. The lack of geometrical structures for range sensors or the scarcity of texture features for vision sensors is analogous to poor satellite geometry in GNSS. Further, the dynamics model of a robot is often uncertain. A fictitious noise approach has to be taken to construct the extended Kalman filter for robot localization. This explains that our model can be effective in improving the performance of the EKF for robot localization. Numerical simulations in a mobile robot localization show performance improvement in Chapter 4.

The process noise model can be applied to non-linear filters other than the extended Kalman filter, such as the unscented and ensemble Kalman filters [59, 60, 61] and the particle filter [62]. These filters also suffer from divergence or biased estimation errors. For example, the particle filter has a resampling step to reproduce particles. If the step unintentionally reproduces many identical particles, the filter will diverge. To avoid divergence, particles should be distributed effectively based on process noise in a time update step. The proposed process noise model could be helpful for distributing particles in a time update step.

The process noise model is based on satellite geometry and measurement matrices. This model has $\Delta P = \alpha H_k^{\mathrm{T}} R_k^{-1} H_k$ as a decision variable. Although α is determined to minimize the sum of squared residuals, $H_k^{\mathrm{T}} R_k^{-1} H_k$ is based on an intuitive sense. We will further examine the appropriateness of $H_k^{\mathrm{T}} R_k^{-1} H_k$ by comparing performance due to several settings based on measurement matrices.

Although Chapter 2 presented the method to reject measurements from NLOS signals, we have not shown the results of the EKF in urban canyons with both the rejection method and the process noise model. We will implement the EKF with the rejection method and the process noise model in a GNSS receiver that can use the modernized L5 signal that can reduce the impact due to multipath signals. We will show position accuracy in urban canyons.

It was assumed in this thesis to improve the position accuracy in urban canyons without additional costs. Since adding other sensors, such as LiDAR devices and cameras, requires an extra cost, we have not used these sensors. However, autonomous and air mobility vehicles will equip these sensors for advanced safety systems. This indicates that the EKF can use

measurements from these sensors without additional costs. We will develop a sensor fusion scheme in the EKF of GNSS and other sensors to obtain more accurate positions in urban canyons [63]. The results of this thesis could play an essential role also in a fusion scheme.

Bibliography

[1] S. J. James J., A. Penina, P. Bradford W., and E. Per, *Global Positioning System: Theory and Applications, Volume I*. Reston, VA, USA: American Institude of Aeronautics and Astronautics, 1996.

[2] Y. T. Morton and M. Jade, *Position, Navigation, and Timing Technologies in the 21st Century: Integrated Satellite Navigation, Sensor Systems, and Civil Applications, Volume 1*. Hoboken, NJ, USA: John Wiley & Sons, Ltd, 2020.

[3] J. F. Zumberge, M. B. Heflin, D. C. Jefferson, M. M. Watkins, and F. H. Webb, "Precise point positioning for the efficient and robust analysis of GPS data from large networks," *Journal of Geophysical Research: Solid Earth*, vol. 102, no. B3, pp. 5005–5017, 1997.

[4] P. Teunissen, "A new method for fast carrier phase ambiguity estimation," in *Proceedings of 1994 IEEE Position, Location and Navigation Symposium - PLANS'94*, 1994, pp. 562–573.

[5] R. E. Kalman, "A new approach to linear filtering and prediction problems," *ASME Journal of Basic Engineering*, vol. 82, no. 1, pp. 35–45, 1960.

[6] A. H. Jazwinski, *Stochastic Processes and Filtering Theory*. Cambridge, MA, USA: Academic Press, 1970.

[7] P. Groves, Z. Jiang, M. Rudi, and P. Strode, "A portfolio approach to NLOS and multipath mitigation in dense urban areas," in *Proceedings of the 26th International Technical Meeting of the Satellite Division of The Institute of Navigation (ION GNSS+ 2013)*, 2013, pp. 3231–3247.

[8] Z. Jiang and P. Groves, "NLOS GPS signal detection using a dual-polarisation antenna," *GPS Solutions*, vol. 18, 01 2014.

[9] P. Groves, *Principles of GNSS, Inertial, and Multisensor Integrated Navigation Systems, Second Edition*. Boston, MA, USA: Artech House, 2013.

[10] O. Mubarak and A. Dempster, "Analysis of early late phase in single-and dual-frequency GPS receivers for multipath detection," *GPS Solutions*, vol. 14, pp. 381–388, 09 2010.

[11] A. Soloviev and F. van Graas, "Utilizing multipath reflections in deeply integrated GPS/INS architecture for navigation in urban environments," in *2008 IEEE/ION Position, Location and Navigation Symposium*, 2008, pp. 383–393.

[12] J. Meguro, T. Murata, J.-i. Takiguchi, Y. Amano, and T. Hashizume, "GPS multipath mitigation for urban area using omnidirectional infrared camera," *IEEE Transactions on Intelligent Transportation Systems*, vol. 10, no. 1, pp. 22–30, 2009.

[13] M. Spangenberg, J.-Y. Tourneret, V. Calmettes, and G. Duchateau, "Detection of variance changes and mean value jumps in measurement noise for multipath mitigation in urban navigation," in *2008 42nd Asilomar Conference on Signals, Systems and Computers*, 2008, pp. 1193–1197.

[14] A. Bourdeau, M. Sahmoudi, and J.-Y. Tourneret, "Tight integration of GNSS and a 3D city model for robust positioning in urban canyons," *25th International Technical Meeting of the Satellite Division of the Institute of Navigation 2012, ION GNSS 2012*, vol. 2, pp. 1263–1269, 01 2012.

[15] Y. C. Lee, "Analysis of range and position comparison methods as a means to provide GPS integrity in the user receiver," in *Proceedings of the 42nd Annual Meeting of The Institute of Navigation (1986)*, 1986, pp. 1–4.

[16] N. Zhu, J. Marais, D. Bétaille, and M. Berbineau, "GNSS position integrity in urban environments: A review of literature," *IEEE Transactions on Intelligent Transportation Systems*, vol. 19, no. 9, pp. 2762–2778, 2018.

[17] S. Hewitson and J. Wang, "GNSS receiver autonomous integrity monitoring with a dynamic model," *Journal of Navigation - J NAVIG*, vol. 60, 05 2007.

[18] A. Grosch, O. Garcia Crespillo, I. Martini, and C. Gunther, "Snapshot residual and Kalman filter based fault detection and exclusion schemes for robust railway navigation," 05 2017, pp. 36–47.

[19] Z. Berman, "Outliers rejection in Kalman filtering - Some new observations," in *2014 IEEE/ION Position, Location and Navigation Symposium - PLANS 2014*, 2014, pp. 1008–1013.

[20] M. Tahsin, S. Sultana, T. Reza, and M. Hossam-E-Haider, "Analysis of DOP and its preciseness in GNSS position estimation," in *2015 International Conference on Electrical Engineering and Information Communication Technology (ICEEICT)*, 2015, pp. 1–6.

[21] R. A. Singer, "Estimating optimal tracking filter performance for manned maneuvering targets," *IEEE Transactions on Aerospace and Electronic Systems*, vol. AES-6, no. 4, pp. 473–483, 1970.

[22] R. Mehra, "Approaches to adaptive filtering," *IEEE Transactions on Automatic Control*, vol. 17, no. 5, pp. 693–698, 1972.

[23] ——, "On the identification of variances and adaptive kalman filtering," *IEEE Transactions on Automatic Control*, vol. 15, no. 2, pp. 175–184, 1970.

[24] G. Gawrys and V. Vandelinde, "On the steady-state error of the fading memory filter," *IEEE Transactions on Automatic Control*, vol. 21, no. 4, pp. 624–625, 1976.

[25] M. Braasch, *Multipath Effects*. Washington, DC, USA: American Institute of Aeronautics and Astronautics, 1996.

[26] C. H. Anderson, "GPS program update," in *62nd Meeting of the Civil GPS Service Interface Committee*, 2022.

[27] P. K. Enge, *The Global Positioning System: Signals, measurements, and performance*. Lincoln, MA, USA: Ganga-Jamuna Press, 1994.

[28] N. Kbayer, M. Sahmoudi, and E. Chaumette, "Robust GNSS navigation in urban environments by bounding NLOS bias of GNSS pseudoranges using a 3D city model," in *Proceeding of 28th International Technical Meeting of the Satellite Division of the Institute of Navigation, ION GNSS 2015*, 2015, pp. 2410–2420.

[29] T. Tominaga and N. Kubo, "Adaptive estimation of measurement noise to improve the performance of GNSS single point positioning in dense urban environment," *Journal of IPNT*, vol. 8, no. 1, pp. 1–8, 2017.

[30] ——, "Performance assessment of adaptive kalman filter-based gnss pvt and integrity in dense urban environment," *Transactions of Navigation*, vol. 4, no. 2, pp. 49–58, 2019.

[31] C. Kee, T. Walter, P. Enge, and B. Parkinson, "Quality control algorithms on waas wide-area reference stations," *Journal of The Institute of Navigation*, vol. 44, no. 1, pp. 53–62, 1997.

[32] P. Misra and P. Enge, *Global Positioning System: Signals, Measurements, and Performance (Revised Second Edition)*. Ganga-Jamura Press, 2010.

[33] E. D. Kaplan and C. J. Hegarty, *Understanding GPS/GNSS: Principles and Applications Third edition*. Artech House, 2017.

[34] G. Castaldo, A. Angrisano, S. Gaglione, and S. Troisi, "P-RANSAC: an Integrity monitoring approach for GNSS signal degraded scenario," *International Journal of Navigation and Observation*, vol. 2014, 09 2014.

[35] K. Shodai, K. Mitsunori, S. Taro, and A. Yoshiharu, "NLOS satellite detection using a fish-eye camera for improving GNSS positioning accuracy in urban area," *Journal of Robotics and Mechatronics*, vol. 28, no. 1, pp. 31–39, 2016.

[36] T. Suzuki and N. Kubo, "N-LOS GNSS signal detection using fish-eye camera for vehicle navigation in urban environments," in *Proceeding of 27th International Technical Meeting of the Satellite Division of the Institute of Navigation, ION GNSS 2014*, 2014, pp. 1897–1906.

[37] W. Wen, G. Zhang, and L.-T. Hsu, "Correcting NLOS by 3D LiDAR and building height to improve GNSS single point positioning," *Navigation*, vol. 66, pp. 705–718, 12 2019.

[38] P. Axelrad and P. Brown, *GPS Navigation Algorithm*. Washington, DC, USA: American Institute of Aeronautics and Astronautics, 1996.

[39] R. Fitzgerald, "Divergence of the Kalman filter," *IEEE Transactions on Automatic Control*, vol. 16, no. 6, pp. 736–747, 1971.

[40] A. Gelb, *Applied Optimal Solutions*. Cambridge, MA, USA: MIT Press, 1974.

[41] L. Shi, K. H. Johansson, and R. M. Murray, "Kalman filtering with uncertain process and measurement noise covariances with application to state estimation in sensor networks," in *2007 IEEE International Conference on Control Applications*, 2007, pp. 1031–1036.

[42] D. Simon, *Optimal State Estimation*. Hoboken, NJ, USA: Wiley-Interscience, 2006.

[43] W. Ding, J. Wang, C. Rizos, and D. Kinlyside, "Improving adaptive kalman estimation in GPS/INS integration," *The Journal of Navigation*, vol. 60, pp. 517–529, 09 2007.

[44] C. Hu, W. Chen, Y. Chen, and D. Liu, "Adaptive Kalman filtering for vehicle navigation," *Journal of Global Positioning Systems*, vol. 2, pp. 42–47, 06 2003.

[45] J. Zhang, M. Kaess, and S. Singh, "On degeneracy of optimization-based state estimation problems," in *2016 IEEE International Conference on Robotics and Automation (ICRA)*, 2016, pp. 809–816.

[46] D. Simon and T. L. Chia, "Kalman filtering with state equality constraints," *IEEE Transactions on Aerospace and Electronic Systems*, vol. 38, no. 1, pp. 128–136, 2002.

[47] G. Ammar, P. Benner, and V. Mehrmann, "A multishift algorithm for the numerical solution of algebraic riccati equations," *Electronic Transactions on Numerical Analysis*, vol. 1, 08 1998.

[48] M. Moorman and T. Bullock, "Mathematical analysis of bias in the extended Kalman filter," in *Proceedings of the 30th IEEE Conference on Decision and Control*, 1991, pp. 2733–2737 vol.3.

[49] Y. Takayama, T. Urakubo, and H. Tamaki, "Novel process noise model for GNSS Kalman filter based on sensitivity analysis of covariance with poor satellite geometry," *Sensors*, vol. 21, no. 18, 2021.

[50] ——, "Avoiding GNSS kalman filter in urban canyons with a novel process noise model," in *Proc. of ION GNSS+ 2022*, 2022, pp. 1831–1839.

[51] G. W. Gawrys and V. D. Vandelinde, "Divergence and the fading memory filter," in *1975 IEEE Conference on Decision and Control including the 14th Symposium on Adaptive Processes*, 1975, pp. 66–68.

[52] J. Sacks and H. Sorenson, "Nonlinear extensions of the fading memory filter," *IEEE Transactions on Automatic Control*, vol. 16, no. 5, pp. 506–507, 1971.

[53] W. Zhou, X. Qiao, F. Meng, and H. Zhang, "Study on SINS/GPS tightly integrated navigation based on adaptive extended Kalman filter," in *The 2010 IEEE International Conference on Information and Automation*, 2010, pp. 2344–2347.

[54] D. Wang, Y. Dong, Z. Li, Q. Li, and J. Wu, "Constrained MEMS-based GNSS/INS tightly coupled system with Robust kalman filter for accurate land vehicular navigation," *IEEE Transactions on Instrumentation and Measurement*, vol. 69, no. 7, pp. 5138–5148, 2020.

[55] G. Dissanayake, S. Sukkarieh, E. Nebot, and H. Durrant-Whyte, "The aiding of a low-cost strapdown inertial measurement unit using vehicle model constraints for land vehicle applications," *IEEE Transactions on Robotics and Automation*, vol. 17, no. 5, pp. 731–747, 2001.

[56] T. S., B. W., and D. Fox., *Probabilistic Robotics*. Cambridge, MA, USA: MIT Press, 2005.

[57] C. Harald, *Mathematical Methods of Statistics*. Princeton, NJ, USA: Princeton University Press, 1946.

[58] J. Zhang, M. Kaess, and S. Singh, "On degeneracy of optimization-based state estimation problems," in *2016 IEEE International Conference on Robotics and Automation (ICRA)*, 2016, pp. 809–816.

[59] S. Julier and J. Uhlmann, "Unscented filtering and nonlinear estimation," *Proceedings of the IEEE*, vol. 92, no. 3, pp. 401–422, 2004.

[60] S. Julier, J. Uhlmann, and H. Durrant-Whyte, "A new method for the nonlinear transformation of means and covariances in filters and estimators," *IEEE Transactions on Automatic Control*, vol. 45, no. 3, pp. 477–482, 2000.

[61] G. Evensen, "The ensemble Kalman filter for combined state and parameter estimation," *IEEE Control Systems Magazine*, vol. 29, no. 3, pp. 83–104, 2009.

[62] P. Djuric, J. Kotecha, J. Zhang, Y. Huang, T. Ghirmai, M. Bugallo, and J. Miguez, "Particle filtering," *IEEE Signal Processing Magazine*, vol. 20, no. 5, pp. 19–38, 2003.

[63] W. Wen, T. Pfeifer, X. Bai, and L.-T. Hsu, "Factor graph optimization for GNSS/INS integration: A comparison with the extended Kalman filter," *NAVIGATION*, vol. 68, 05 2021.

[64] R. Ueda, *Lecture Notes of Probabilistic Robotics(in Japanese)*. Bunkyoku, Tokyo, JP: Kodansha, 2019.

List of Publications

Journal Publications:

TAKAYAMA Yoji, URAKUBO Takateru, TOMINAGA takaki, TAMAKI Hisashi: Accuracy Enhancement of GNSS/INS Positioning in Dense Urban Environments with NLOS Signal Rejection based on Geometric Model. Transactions of the Institute of Systems, Control and Information Engineers, Vol. 34, Issue 2, pp. 37-46, 2021.

TAKAYAMA Yoji, URAKUBO Takateru, TAMAKI Hisashi: Novel Process Noise Model for GNSS Kalman Filter Based on Sensitivity Analysis of Covariance with Poor Satellite Geometry. Sensors, Vol. 21, Issue 18, 6056, 2021.

TAKAYAMA Yoji, URAKUBO Takateru, TAMAKI Hisashi: Adaptive Choice of Process Noise Covariance in Kalman Filter Using Measurement Matrices. IEEE Transactions on Control Systems Technology (submitted).

Publications in Proceedings of International Conference:

TAKAYAMA Yoji, URAKUBO Takateru, TAMAKI Hisashi: A Study on Efficient LiDAR-based Localization with Initial Pose Estimation. Proceedings of the 2020 IEEE/SICE International Symposium on System Integration (SII), pp. 985-990, 2020.

TAKAYAMA Yoji, URAKUBO Takateru, TAMAKI Hisashi: Avoiding GNSS Kalman Filter Degradation in Urban Canyons with a Novel Process Noise Model. Proceedings of the 35th International Technical Meeting of the Satellite Division of T he Institute of Navigation (ION GNSS+ 2022), pp. 1831-1839, 2022.

Appendix A

Reason for Minimizing Measurement Residuals

Under the Assumption 4.4.1, we can divide e_k^* into $e_{k,a}^*$ and $e_{k,b}^*$ as follows.

$$\begin{aligned} e_k^* &= e_{k,a}^* + e_{k,b}^*, \\ e_{k,a}^* &= P_{H_k} e_k^*, \;\; e_{k,b}^* = (I - P_{H_k}) e_k^*, \end{aligned} \tag{A.1}$$

where $*$ means $+$ or $-$, and P_{H_k} is a following projection matrix:

$$P_{H_k} = H_k^{\mathrm{T}} (H_k H_k^{\mathrm{T}})^{-1} H_k. \tag{A.2}$$

Then, using $\Psi_k(0) = I - K_k(0) H_k$, $e_k^+(\delta Q_k)$ can be approximated as follows.

$$\begin{aligned} e_k^+(\delta Q_k) &\approx [I - (K_k(0) + \Delta K_k) H_k] e_k^- - (K_k(0) + \Delta K_k) v_k \\ &= (\Psi_k(0) - \Delta P_k H_k^{\mathrm{T}} R_k^{-1} H_k) e_{k,a}^- + e_{k,b}^- \\ &\quad - (K_k(0) + \Delta P_k H_k^{\mathrm{T}} R_k^{-1}) v_k. \end{aligned} \tag{A.3}$$

Further, we obtain

$$\begin{aligned} e_{k,a}^+(\delta Q_k) = P_{H_k} &(\Psi_k(0) - \Delta P_k H_k^{\mathrm{T}} R_k^{-1} H_k) e_{k,a}^- \\ &- P_{H_k} (K_k(0) + \Delta P_k H_k^{\mathrm{T}} R_k^{-1}) v_k, \end{aligned} \tag{A.4}$$

$$e^+_{k,b}(\delta Q_k) = (I - P_{H_k})(\Psi_k(0) - \Delta P_k H_k^{\mathrm{T}} R_k^{-1} H_k) e^-_{k,a} + e^-_{k,b} - (I - P_{H_k})(K_k(0) + \Delta P_k H_k^{\mathrm{T}} R_k^{-1}) v_k. \tag{A.5}$$

When ΔP_k is chosen as $\Delta P_k = \alpha_k H_k^{\mathrm{T}} R_k^{-1} H_k + \beta_k \mathcal{H}_k^{\perp}$ in Section 4.4, (A.5) can be rewritten as

$$e^+_{k,b}(\delta Q_k) = (I - P_{H_k})\Psi_k(0) e^-_{k,a} + e^-_{k,b} - (I - P_{H_k}) K_k(0) v_k = e^+_{k,b}(0), \tag{A.6}$$

which means that $e^+_{k,b}(\delta Q_k)$ does not depend on δQ_k or ΔP_k. Therefore, the norm of $e^+_k(\delta Q_k)$ can be represented as

$$\begin{aligned} \|e^+_k(\delta Q_k)\|^2 &= \|e^+_{k,a}(\delta Q_k)\|^2 + \|e^+_{k,b}(\delta Q_k)\|^2 \\ &= \|e^+_{k,a}(\delta Q_k)\|^2 + \|e^+_{k,b}(0)\|^2. \end{aligned} \tag{A.7}$$

Since $\|e^+_{k,a}(\delta Q_k)\|^2 = \|H_k e^+_k(\delta Q_k)\|^2 = \|m_k(\delta Q_k) - v_k\|^2$, minimization of $\|e^+_k(\delta Q_k)\|^2$ corresponds to minimization of $\|m_k(\delta Q_k)\|^2$ except for the term of v_k.

In the sense of minimization of estimation error covariance, we can consider the problem of minimizing $E\{\|e^+_{k,a}(\delta Q_k)\|^2\}$. However, in Section 4.4, we employ the problem of minimizing $E\{\|m_k(\delta Q_k)\|^2_{R_k^{-1}}\}$ from the perspective of an adaptive filter based on the measurements. It should be noted that these problems are not equivalent because $e^+_{k,a}(\delta Q_k)$ and $m_k(\delta Q_k)$ contain v_k differently.

Appendix B

Accumulation of Fictitious Noise

In this appendix, we show by a simple example that fictitious noises with non-zero β_k accumulate in the estimation error covariance matrix P_k^+ and cause large estimation errors when the measurement matrix H_k varies significantly. We consider the system where $n = 2m$, $F_i = I_{n\times n}$, $Q_i = O_{n\times n}$ and $R_i = R$ for all i, and suppose that H_i varies with i, but it satisfies $H_i = (I_{m\times m}, O_{m\times m})$ for $i = k, k+1, \cdots, k+N$.

We also assume that, after the computation of EKF at time step $k-1$, the estimation error covariance P_{k-1}^+ is block diagonal as

$$P_{k-1}^+ = \begin{pmatrix} P_{1,k-1}^+ & O_{m\times m} \\ O_{m\times m} & P_{2,k-1}^+ \end{pmatrix}.$$

At time step k, fictitious noise δQ_k is added to Q_k such that

$$\begin{aligned} \Delta P_k &= \alpha_k H_k^{\mathrm{T}} R_k^{-1} H_k + \beta_k \mathcal{H}_k^{\perp}, \\ &= \begin{pmatrix} \alpha_k \Lambda_k & O_{m\times m} \\ O_{m\times m} & \beta_k \Lambda_k^{\perp} \end{pmatrix}. \end{aligned}$$

Then, $P_k^+(\delta Q_k)$ can be obtained from (4.21) by straightforward calculation as

$$P_k^+(\delta Q_k) = \begin{pmatrix} P_{1,k}^+ & O_{m\times m} \\ O_{m\times m} & P_{2,k}^+ \end{pmatrix},$$

$$P_{1,k}^+ = (I - P_{1,k-1}^+(P_{1,k-1}^+ + R)^{-1})P_{1,k-1}^+ + \alpha_k \Lambda_k, \tag{B.1}$$

$$P_{2,k}^+ = P_{2,k-1}^+ + \beta_k \Lambda_k^\perp. \tag{B.2}$$

Repeating (B.2) from time step k to time step $k+N$, we obtain

$$P_{2,k+N}^+ = P_{2,k-1}^+ + \sum_{i=k}^{k+N} \beta_i \Lambda_i^\perp. \tag{B.3}$$

From (B.3), we can see that $\beta_i \Lambda_i^\perp$ caused from the fictitious noise accumulates in $P_{2,k+N}^+$ without decreasing. It should be noted that, as N increases, the inflation of $P_{2,k+N}^+$ becomes large unboundedly. On the other hand, from (B.1), $P_{1,k}^+$ can be reduced from $P_{1,k-1}^+$ through multiplying it by the gain $(I - P_{1,k-1}^+(P_{1,k-1}^+ + R)^{-1})$. Although $\alpha_k \Lambda_k$ is added in the right-hand side of (B.1), it can also be reduced at time step $k+1$ in $P_{1,k+1}^+$ by the gain $(I - P_{1,k}^+(P_{1,k}^+ + R)^{-1})$.

Next, we assume that the measurement matrix changes at time step $k+N+1$ as $H_{k+N+1} = (I_{m\times m}, I_{m\times m})$. Then, the Kalman gain at time step $k+N+1$ can be calculated as

$$\begin{aligned} K_{k+N+1} &= \begin{pmatrix} P_{1,k+N}^+(P_{1,k+N}^+ + P_{2,k+N}^+ + R)^{-1} \\ P_{2,k+N}^+(P_{1,k+N}^+ + P_{2,k+N}^+ + R)^{-1} \end{pmatrix} \\ &\equiv \begin{pmatrix} K_1 \\ K_2 \end{pmatrix}. \end{aligned}$$

If $P_{2,k+N}^+$ is very large due to the accumulation of $\beta_i \Lambda_i^\perp$, $K_1 \approx O_{m\times m}$ and $K_2 \approx I_{m\times m}$. Denoting $\hat{x}_{k+N+1}^+$ as $[\hat{x}_1^{\mathrm{T}}, \hat{x}_2^{\mathrm{T}}]^{\mathrm{T}}$, $\hat{x}_1$ would not be updated sufficiently according to the measurement innovation, because the Kalman gain K_1 for $\hat{x}_1$ is much smaller than it should be. On the other hand, $\hat{x}_2$ would fluctuate greatly due to the measurement noise, because K_2 for $\hat{x}_2$ is too large. As a result, the accumulation of $\beta_i \Lambda_i^\perp$ would lead to the degradation of filter performance.

It should be noted that the observability is guaranteed by the variation of H_k. However, since the observability is temporarily degenerate for $i = k, k+1, \cdots, k+N$, the inflation of $P_{2,i}^+$ due to $\beta_i \Lambda_i^\perp$ cannot be suppressed. Too large inflation of $P_{2,i}^+$ degrades the filter performance as

mentioned above, at the time step when the measurement matrix changes. This measurement matrix change often happens for the systems working in unknown environments such as an automobile in Sec. 4.5.2 and a mobile robot in Section 4.5.3.

Doctor Thesis, Kobe University

Accurate GNSS Positioning in Urban Canyons with Extended Kalman Filter

Submitted on January, 18, 2023